Detection of Scalar Singlet Dark Matter

A Thesis Submitted to the
College of Graduate Studies and Research
in Partial Fulfillment of the Requirements
for the degree of Master of Science
in the Department of Physics and Engineering Physics
University of Saskatchewan
Saskatoon

By
Frederick Sage

Permission to Use

In presenting this thesis in partial fulfilment of the requirements for a Postgraduate degree from the University of Saskatchewan, I agree that the Libraries of this University may make it freely available for inspection. I further agree that permission for copying of this thesis in any manner, in whole or in part, for scholarly purposes may be granted by the professor or professors who supervised my thesis work or, in their absence, by the Head of the Department or the Dean of the College in which my thesis work was done. It is understood that any copying or publication or use of this thesis or parts thereof for financial gain shall not be allowed without my written permission. It is also understood that due recognition shall be given to me and to the University of Saskatchewan in any scholarly use which may be made of any material in my thesis.

Requests for permission to copy or to make other use of material in this thesis in whole or part should be addressed to:

Head of the Department of Physics and Engineering Physics
162 Physics Building
116 Science Place
University of Saskatchewan
Saskatoon, Saskatchewan
Canada
S7N 5E2

Abstract

The purpose of this thesis is to consider the phenomenology of the scalar singlet model of dark matter in light of current experimental and observational results. Signals of the model from direct detection methods, indirect detection methods and from collider searches are all computed. Direct nuclear recoil signals are calculated and compared with current experimental bounds. Indirect cosmic ray annihilation signals in the form of gamma rays, positrons, antiprotons and antideuterons are examined and the possibility of detecting a measurable signal is considered. A neutrino signal from the annihilation of singlet dark matter gravitationally captured in massive bodies is also computed. Finally, the production and detection of scalar singlet dark matter in particle colliders like the LHC is considered. It is found that the scalar singlet model is favored by current nuclear recoil experiments and consistent with current indirect detection bounds.

Acknowledgements

I would like to thank my supervisor, for putting up with me. Also, my cohort of fellow students deserves thanks for many things, among them: providing amusing anecdotes and jokes to keep me sane, providing advice and help when asked, and above all providing many refreshing beverages. And finally a certain professor, for not booting me out when he had the chance.

This thesis is dedicated to I.P.F. Even though no one else wants to acknowledge you, I will.

Contents

List of Tables

List of Figures

List of Abbreviations

$\mathcal{SM}$	Standard Model
SUSY	Supersymmetry
QCD	Quantum Chromodynamics
WIMP	Weakly Interacting Massive Particle
MACHO	Massive Compact Halo Object
MOND	Modified Newtonian Dynamics
LHC	Large Hadron Collider
NFW	Navarro-Frenk-White
LAT	Large Area Telescope
CMB	Cosmic Microwave Background
LO	Leading Order
NLO	Next to Leading Order
NNLO	Next to Next to Leading Order

Chapter 1

Background

For the last few decades, the astrophysical community has been grappling with a problem. We shall call it the 'dark matter problem,' and we shall formulate it in the following manner. Our understanding of Newtonian mechanics is quite sound, in that it makes predictions that are accurate within the relevant regime. This is not the case in certain astrophysical gravitational systems. In these systems Newtonian gravitation predicts behavior that is markedly different from what is observed to occur. These phenomena have been examined and confirmed beyond any reasonable doubt. There is certainly something occurring.

It was noticed that the predictions become accurate if one postulates the existence of a significant quantity of invisible mass. This hypothetical invisible mass has been given the name 'dark matter.' The alternative to the existence of this dark matter is that our understanding of gravitation at large scales is fundamentally flawed. So the dark matter problem is formulated here as the problem of gravitational anomalies being observed in the universe. The resolution of the problem is either the physical existence of dark matter or the modification of gravity. As will be shown in Section 1.3, both approaches have been, and continue to be, attempted.

Those who support the physical existence of dark matter, or particle dark matter, appear to have the majority over those who support the alternative, and many theories have been put forward as to the nature of dark matter. Normal matter was originally considered, but the consensus is now that dark matter is some kind of exotic particle, not something that is part of the Standard Model ($\mathcal{SM}$) of particle physics. This shift in attitude occurred over decades, as more and more people began to treat the problem seriously. Now there are dozens of different models being worked on by thousands of scientists. There is no doubt that dark matter is out there, in one form or another. Dark matter exists beyond the $\mathcal{SM}$ of particle physics, and that it does exist indicates that our understanding of particle physics is incomplete.

Whether the solution to the dark matter problem is found in particle physics, in gravitational physics or in both, there is no doubt that it will change our understanding of the universe.

1.1 Evidence

We provide a brief summary of the evidence for the existence of dark matter, evidence which can be taken to comprise the dark matter problem itself. The existence of dark matter is accepted by the scientific com-

munity because of the amount of evidence it has accumulated, and any competing model must explain these phenomena to be considered a serious rival to dark matter. At this point, the evidence is all gravitational. We move from the small to the large, advancing from the scale of galaxies to the scale of clusters to the cosmological scale.

What is usually cited as the primary piece of evidence for the existence of dark matter is found in studies of the rotation curves of spiral galaxies. This is in fact what convinced much of the physics community that the dark matter problem was real. The discrepancy was first noticed in the 1930s, but it was paid no attention until the 1970s when Rubin and her collaborators [104] surveyed the rotation curves of some sixty spiral galaxies through Doppler analysis and found the same issue in all of them.

A spiral galaxy is a stable system bound by gravity in which luminous components orbit a center with nearly circular trajectories. It is expected that such a system will follow Newtonian dynamics, which would have a stability condition of the centrifugal force being balanced by the gravitational pull. If $v(r)$ is the tangential velocity at radius r from the center of the galaxy, $M(r)$ is the total mass inside r, and G is Newton's gravitational constant, the stability condition reads:

$$a_f = \frac{v^2}{r} = \frac{GM(r)}{r^2} = a_g$$

$$\Rightarrow v = \sqrt{\frac{GM(r)}{r}}$$

This agrees with Keplerian orbital motion. Once the mass $M(r)$ stops increasing with radius, as we expect should happen when considering the velocities of stars and gas at the very edge of the galactic disc, it becomes constant and v should fall off like $\frac{1}{\sqrt{r}}$. This falling off of velocity is not what is observed, as can be seen in Figure 1.1.

What is observed is that $v(r)$ is roughly constant, even far past the luminous regions of the galaxy. The only way to retain the stability condition at this point is to say that $M(r)$ is not constant in these regions. So there must be some form of nonluminous mass extending far beyond the luminous regions of the galaxy. This mass is dark matter. The canonical reference on the subject of rotation curves of spiral galaxies is by Rubin and Sofue [112].

There is a significant amount of support for dark matter from gravitational lensing. We know from general relativity that mass curves spacetime and that the motion of objects in curved spacetime is what we call 'gravity.' The curvature of spacetime can affect the motion of massless particles like photons, and substantial mass can deflect them by a considerable amount. Such deflection is called gravitational lensing, and the region in which the light is deflected is called the gravitational lens. Gravitational lenses, once observed and analyzed, can be used to examine mass distributions. A recent review of the evidence for the existence of dark matter from gravitational lensing surveys exists [91], and it cites much of the observational literature.

Lensing studies have given us not only evidence for the presence of dark matter, but also demonstrations that it interacts roughly normally through gravity, and details of its large scale distribution.

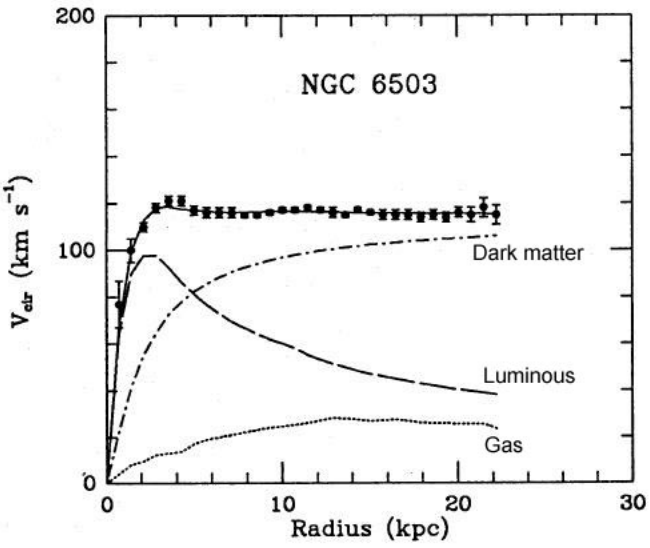

Figure 1.1: Galactic Rotation Curve of Galaxy NGC6503 [15]

There are three basic types of lensing to be considered. First, there is strong lensing, which is when a dense concentration of mass warps space to such a degree that light from an object behind it can take multiple paths around the concentration. This is the most mentioned type of lensing, giving rise to the well known 'Einstein ring' effect, where a ring of multiple images can appear surrounding the lens. We can determine how much mass a dense object, such as a distant galaxy or even more distant galaxy cluster, has by considering its action as a lens. In doing so, we see that the luminous mass cannot account for all of the gravitationally interacting matter present. Strong lensing is limited in its use, however, since it requires a line of sight that ends in a strong lens to get any observations, and such lines of sight are finite in number. It can provide evidence of localized dark matter, but it can say little about large scale distributions.

Secondly, we have what is called microlensing. This happens on the scale of a single star. When a dark massive object, like a planet, passes in front of a star, the star is visibly brightened, as its light is focused by the gravitational lens of the dark object. Microlensing has been used to search for Massive Compact Halo Objects (MACHOs), which were thought to make up a significant part of dark matter at one time. MACHOs are dark macroscopic objects like planets or brown dwarfs that drift about in the galaxy. Microlensing studies of millions of stars in different galaxies over many years have observed only a handful of events, indicating that MACHOs, while certainly present, are not capable of accounting for all of the dark matter. A high estimate is that 20% of dark matter is MACHOs [91].

The final type of lensing study is weak lensing, which has turned out through the power of statistics to be the most useful. While the other two types consider lensing by single objects, on the stellar scale or larger, weak lensing considers lensing by an entire mass distribution. Weak deflections of light through an extended lens can be approximated as a linear transformation of the sky. This technique has only become available in

the past twenty years. A shearing effect generated by the weak lens can alter the shapes of distant galaxies, adjusting their major-minor axis by $\sim$2%.

On the level of an individual galaxy, this cannot be observed, but all galaxies along a line of sight are changed in the same way, while their unaltered shapes should be uncorrelated. From this we can extract a shear signal, considering the intrinsic shape of the galaxies as noise. This shear signal can be related to the gravitational potential along the line of sight, which can be converted to a mass distribution map. This allows study of the large scale structure of mass distributions in the universe. Through this method, we obtain data on mass distributions in galaxy clusters, and larger scale structures. Additionally, since we are looking into the past when we look at distant galaxies, weak lensing gives us information about structure formation.

An example of weak lensing in action is the analysis of the Bullet Cluster, actually a pair of colliding clusters that have been called a 'smoking gun' for dark matter [33]. The collision has three separate components: the galaxies, the hot x-ray emitting gas, and the dark matter, which cannot be seen. Since the individual galaxies do not collide, they follow their original trajectories without any substantial change of motion. The intracluster gas clouds, seen by x-ray astronomy, interact with each other and so remain entangled in the impact region. This is what we see. Lensing tells us that some 30-40 times the visible mass is present with the galaxies, some 8σ of significance different from the gaseous regions, apparently having passed through the collision without a change in motion. Such mass would have to be electromagnetically neutral and nearly collisionless. Essentially, it would need to be dark matter. The Bullet Cluster is somewhat of a rarity, as we are seeing it in the midst of the collision, before gravitation has had a chance to pull the disparate components back together into one large cluster. The search for other mid-collision pairs of this type is ongoing, to turn a single event into a recognized phenomenon.

Some of the first evidence for dark matter was due to the application of the virial theorem to the motion of galaxies in a cluster. In 1933, Fritz Zwicky took data on the motion of galaxies in the Coma Cluster and then applied the virial theorem to his observations [123]. The general virial theorem relates the time averaged kinetic energies of bodies in a bound system to the total potential energy of the system. The application to systems that are gravitationally bound is obvious, and what Zwicky noted was that since the total gravitational potential energy of the system is related to its mass, one can use the observed motion of constituent bodies to estimate the mass of the whole system. In a simple illustration, if we take a cluster of N gravitating objects with average mass m and average velocity v, we can write the total kinetic energy of the system as

$$K = \frac{1}{2} N m v^2$$

If the average separation is r, the gravitational potential energy of the system, taking into account all pairings, is

$$V = -\frac{1}{2} N(N-1) \frac{G m^2}{r}$$

The virial theorem states

$$K = -\frac{V}{2}$$

So then the total system mass $M = Nm$ can be estimated, with $m \ll M$ as

$$M \approx \frac{2rv^2}{G}$$

Zwicky estimated this mass and found it to be much greater than the total mass of the luminous bodies that were observed. Though he was somewhat off with his actual numerical values compared to current estimates, his proposal of the existence of dark matter in the Coma Cluster was the first indication of cluster level missing mass.

Modern estimates of cluster mass using kinematics are far more complex than the simple application of the virial theorem above. They continue to indicate the presence of dark matter, however [89].

On the largest scales as well, there is evidence for dark matter. Cosmological evidence takes the form of observations that indicate the presence of dark matter in the early universe, when matter and energy first decoupled as a result of expansion.

Before decoupling occurred, matter and energy were in thermal equilibrium, with particles and photons constantly interacting. Regions of this mixture would contract due to gravity before being forced apart due to radiation pressure, which reduced the pressure enough that gravity could take over again, leading to oscillations in density. When the photons decoupled from baryonic matter, the oscillations ceased, and their state at the time of 'last scattering,' as it is called, is visible in large scale cosmological structures.

We can see the time of last scattering, when photons and baryonic matter dropped out of equilibrium, if we look hard enough. Looking into the distance is equivalent to looking back in time, and if we look far enough, we will see a 'wall' of light which we call the Cosmic Microwave Background (CMB). The CMB is composed of the photons whose last interaction was with a baryon in thermal equilibrium at the instant of decoupling. We can examine the distribution of these photons to explore the state of matter at decoupling.

The surveys from COBE [25] and more recently WMAP [82] study the CMB, and have found that it is not uniform. Some regions of the sky are colder than others, and they can be seen as darker patches in Figure 1.2. These anisotropies are taken to be evidence of the oscillations in the primordial mixture mentioned above. We can expand the CMB in terms of spherical harmonics to study these anisotropies in detail.

At the largest scales, the distribution of matter appears to have structure. Galaxies are organized into clusters, which are organized into superclusters, which make up what are called filaments. When these filaments were first observed, we had no idea how they came about. Now, we think they are the result of the primordial density fluctuations. When decoupling occurred, certain regions were more densly populated by baryons than others, giving them a greater gravitational potential. Matter was attracted to these dense regions, making them denser and so more attractive. Continuing, we can see how modern structure could form as the result of these initial oscillations. Wide angle galaxy surveys have provided us with a great deal

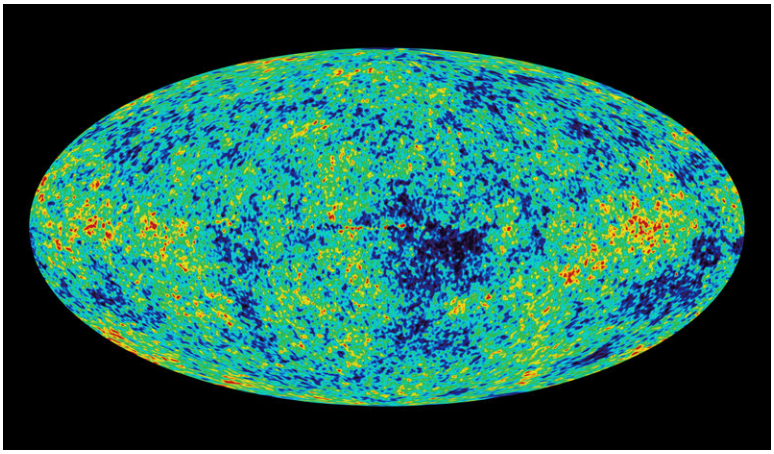

Figure 1.2: Cosmic Microwave Background (Image from NASA's public archive)

of information about large scale structure. From these observations we can work backwards using simulations to try to reproduce the initial conditions that led to these observed phenomena. However, a problem arises.

Examining the CMB anisotropies gives us an idea of the structure of the initial baryonic density perturbations after decoupling. From what we can compute and simulate, these perturbations are insufficient to give us the structure we currently observe. Their gravitational potential would need a much longer time frame to create the present structure.

One explanation for this is that there was another kind of matter, one that did not interact with photons and so decoupled from the primordial mixture much sooner than the baryonic matter did. If this pressureless matter decoupled before the CMB was created, and if it existed in much greater abundance than baryonic matter, the density perturbations left by its decoupling would overwhelm the baryonic fluctuations and provide a scaffolding for present structure. If the nonbaryonic matter decoupled early enough, it would be capable of providing enough gravitational attraction to produce the structure we see. This pressureless matter is identified with dark matter in standard cosmological models.

This is a remarkably strong consistency argument. Observations of Type Ia supernovae, from exploding white dwarf binary star systems that are called 'standard candles' of cosmology [83], give us a quantitive factor for the expansion of the universe. CMB anisotropies constrain the baryonic component and large scale structure constrains the total matter component. These three independant cosmological data sets are combined to give us the standard Cold Dark Matter cosmological model. We take the total energy density as $\Omega_0 = \Omega_\Lambda + \Omega_{DM} + \Omega_b$, with Ω_Λ the expansion component (dark energy), Ω_{DM} the dark matter component, and Ω_b the baryonic component. Best fit analysis of the data of these three kinds of observations gives us the values we use. The actual analysis is quite complicated. General reviews of dark matter contain the basics of these ideas, and a book discusses much of this material in great depth [11].

There could be another explanation for these observations, but the best one we have is the existence of

some kind of dark matter. While compelling models may explain the evidence on smaller scales with differing amounts of success, they all fail at reproducing these cosmological phenomena. To remove dark matter would require us to rework cosmology from the earliest time scales.

1.2 Alternative Models

Before proceeding to discuss the model of dark matter we work with in this thesis, it is beneficial to provide a brief overview of several alternative solutions to the dark matter problem that have enjoyed attention in the literature. This section is by no means exhaustive, either in inclusion of all alternative models, or in explanatory depth of the models that are included. We simply seek to paint a picture of what else is out there. References are provided for each of the models mentioned, so further details are easily obtained. General reviews of particle dark matter candidates are also available [23].

When one reads papers on dark matter detection, one often finds the discussion framed in terms of the Weakly Interacting Massive Particle, or WIMP. The WIMP is a generic form of particle dark matter, having a mass anywhere from keV scale to TeV scale and interacting with $\mathcal{SM}$ matter with strength on the same scale or weaker than the weak interaction. Most kinds of particle dark matter can be called WIMPs, and so experimental or theoretical results are often formulated for the WIMP. In this thesis, when we speak of things that can apply to any kind of dark matter, we use the term WIMP. When we specify to the scalar singlet model which is the focus of this thesis, we use the term singlet.

Of all the models for particle dark matter, the ones with the most support are the class of models which propose supersymmetric dark matter. The theory is pleasing in many ways, for it solves a number of issues in high energy physics with a potential explanation for dark matter being something of a bonus. While the full details of supersymmetry are far too complex to even begin to present here, we provide a brief outline of the theory in the context of dark matter.

Supersymmetry (SUSY) is a new symmetry of spacetime, one that relates fermionic (half integer spin) and bosonic (integer spin) particles. One of the reasons it was proposed was to solve the hierarchy problem. The hierarchy problem is that the scale differences in the $\mathcal{SM}$ are so far apart. For example, the Higgs mass including radiative corrections and the Planck mass are many orders of magnitude apart. SUSY fixes this issue to all orders in perturbation theory by proposing that each $\mathcal{SM}$ particle has a supersymmetric partner, an s-particle or sparticle, that differs from it in spin by 1/2. So fermions have bosonic superpartners and bosons have fermionic superpartners. In the minimal case, we double the number of fermions and vector bosons, as well as requiring two Higgs doublets, each with their own superpartner field.

Included in SUSY is a quantum number known as $\mathcal{R}$-parity, which is assumed to be conserved. It can be assigned by simply stating that for particles $\mathcal{R} = 1$ and for sparticles $\mathcal{R} = -1$. This number was originally proposed to prevent proton decay into superpartner states, but has the additional property of making the lightest supersymmetric particle absolutely stable. Since this particle is constrained to be electromagnetically

and color neutral, it is a natural candidate for dark matter.

Which sparticle is the lightest depends on which version of SUSY is being used. There are a large number of them, varying in which phenomena they try to explain and which assumptions are made. Some lightest sparticles which have been proposed are the sneutrino, which is the superpartner of the neutrino and has long been excluded by direct detection bounds, the axino, which is the superpartner of the axion (discussed later in this section), and the gravitino, the superpartner of the hypothetical graviton, a spin 2 boson that acts as the carrier of the gravitational force in quantum gravity. Theories that include axinos and gravitinos as the lightest sparticle tend to have certain unattractive properties, making them disfavored.

By far the most favored candidate for the lightest sparticle, and hence for particle dark matter, is the neutralino. Superpartners of the electroweak gauge boson fields, called winos and zinos, and a pair of Higgsinos, which are Higgs superpartners, combine to form four Majorana fermionic mass eigenstates called neutralinos. The lightest of these is 'the' neutralino of SUSY dark matter literature. Neutralinos are expected to be nonrelativistic at the present time, and to have interesting annihilation spectra. For many, the neutralino represents the ideal WIMP dark matter candidate.

The actual predictions SUSY dark matter makes depend completely on the kind of SUSY chosen. The usually used Minimal Supersymmetric $\mathcal{SM}$ has a large number of free parameters, mostly representing various masses and mixing angles. A number of assumptions must be made to reduce this number from over a hundred to a phenomologically managable handful. These assumptions give the framework that allows meaningful predictions to be made. The parameter space for SUSY dark matter still remains large, but it can be reduced by comparison with experimental data.

There are any number of papers dealing with SUSY dark matter, but the essential reference [78] has been the standard for the past fifteen years, though it is becoming dated. More up to date, though less comprehensive, reviews have been published [23].

One of the more popular ideas that has been considered in fundamental theoretical physics is the possibility that reality has more than the 3+1 dimensional structure it appears to. Theories that postulate these extra dimensions have used them to present solutions to many problems in particle physics, and they can present a solution to the dark matter problem as well.

Fields propagating in extra dimensions can be Fourier expanded into what are called Kaluza-Klein states. These states would appear to us as a series of particle states with increasing mass and the same quantum numbers. As with SUSY, there are many different variations on this theme, a large number of models with differing properties. Conservation of momentum in the extra dimensions and the formalism of fermion generation result in an effective symmetry, similar to $\mathcal{R}$-parity in SUSY, that stabilizes the lightest of these Kaluza-Klein states. It is this lightest state that is put forward as a candidate for particle dark matter.

The lightest Kaluza-Klein particle is usually associated with the first Kaluza-Klein excitation of the photon. Thermal equilibrium calculations from the early universe and constraints from present abundance requirements have placed its mass in the 400-1200 GeV range [107]. This is at the edge of the range we are

currently able to probe, and the next generation of detectors should be able to reach well into that zone. Further details on Kaluza-Klein dark matter are available in the review paper by Servant [108].

Another example of a dark matter candidate that was originally proposed to deal with a different problem in particle physics is the axion. In the nonperturbative regime of quantum chromodynamics, the theory predicts large CP violations in strong sector interactions. This is not observed experimentally. It was noted that the CP-violating phase could be made dynamical by introducing a global $U(1)$ symmetry, which would then be broken. This broken symmetry would then, by Goldstone's Theorem, generate a Goldstone boson. This boson was called the axion, and it gains a mass through anomalous mixing with the π and η mesons.

The exact phenomenology of the axion is determined by the scale factor of the broken symmetry. The mass of the axion has been restricted by experiments and observations of stellar processes to $m_a < 0.01\, eV$, which is exceptionally light for a dark matter particle. The axion couples so weakly to ordinary matter, primarily through photons, that it was never in thermal equilibrium in the early universe, making calculations of current abundances difficult. Axion production is also poorly understood, further complicating relic density estimates.

The axion was one of the earliest proposed candidates for non-baryonic dark matter, and so has had a wide variety of treatments in the literature. A recent review of axion dark matter by Sikivie is available [22]. Modern constraints are shrinking the axion parameter space. There remains a mass region (from 10^{-5} to 10^{-2} eV) in which the axion could act as dark matter, but current experiments are biting into that region already. There are also experiments looking for axions in this mass range outside the context of dark matter. While the axion model was strong in the past, recent results have made it less attractive than the alternatives.

A somewhat popular class of models are called 'little Higgs' models, which attempt to stabilize the weak scale in an alternative to SUSY. In such models, the $\mathcal{SM}$ Higgs boson has a mass fixed by symmetries guaranteeing stability up to ~ 10 TeV. Since this is a class of models, different models provide different dark matter candidates. Candidates are generally stable scalar particles with masses occasionally reaching into the TeV range. These models often need to have a symmetry inserted by hand to guarantee stability of the candidate particle. There are reviews of these theories available [24].

A particle that is all but ruled out for dark matter at this point is the sterile neutrino. It was a good prospect in the past, but has been shown to be far too light, if it even exists, to account for the majority of the cold dark matter in the universe. Sterile neutrinos are right handed massive neutrinos that do not interact with $\mathcal{SM}$ matter, except for mixing with the $\mathcal{SM}$ neutrino sector. A recent book on particle dark matter has provided a review of sterile neutrinos as dark matter [22].

There are many other candidates for dark matter which have been proposed that we will not provide any detail for. They include inert Higgs doublets [90], mirror dark matter [57], WIMPzillas [81], and dark matter as primordial black holes [58]. Work is done on these models, but not as much as on the models presented above, or as much as on model that is the focus of this thesis.

It was mentioned earlier that the alternative to particle dark matter is the modification of gravitational

theory. As one of the main pieces of evidence supporting dark matter, the discrepancy in galactic rotation curves, is the result of a prediction made by Newtonian mechanics, several astrophysicists have postulated that Newtonian mechanics itself does not apply at such large scales. Since Newtonian mechanics has not been experimentally tested in these regimes, this hypothesis is valid. The resulting altered theories of dynamics are called Modified Newtonian Dynamics (MOND).

The basic premise behind MOND is that Newton's second law, $F = ma$, is not correct. The equation is modified so that

$$F = ma\mu\left(\frac{a}{a_0}\right)$$

The parameter a_0 is some acceleration scale that determines when the new dynamics comes into effect. The function $\mu\left(\frac{a}{a_0}\right)$ is $\simeq 1$ for $a \gg a_0$ and is $\simeq \frac{a}{a_0}$ for $a \ll a_0$. The scale a_0 is believed to be $\simeq 10^{-10}\ m/s^2$, so Newtonian dynamics is modified at exceptionally low accelerations. Applying this to basic rotational motion:

$$\Rightarrow a = \frac{v^2}{r} \Rightarrow \frac{GM}{r^2} = \left(\frac{v^2}{r}\right)^2 \frac{1}{a_0} \Rightarrow v^4 = GMa_0$$

This gives the constant rotation curves observed outside the mass distribution that are observed. There is no doubt that with the proper fine tuning, MOND describes galactic rotation curves very well. However, it has no explanation for the other evidence that has been accumulated in favor of particle dark matter, such as the Bullet Cluster. Due to this, it lacks the support of much of the community. Work on MOND continues, and further modifications of the theory may yet produce results. Detailed reviews of MOND are avialable [97] [16].

There have also been attempts to resolve the dark matter problem using general relativity [40]. Such explanations have been generally unsuccessful, using unjustified assumptions or not standing up to the scrutiny of peer review.

1.3 Detection of Dark Matter

While there are a plethora of models proposing one kind of particle dark matter or another, none can be fully accepted until they pass the experimental gauntlet. These models must provide some kind of signature that can be searched for. Only in the past decade have experimental searches for dark matter really taken off, with the dark matter problem moving firmly into the experimental domain. The particle astrophysics community is now capable of testing its models against reality.

In this section, as well as in the sections of each chapter where the basics of the detection methods are discussed, we write about detection of a generic WIMP. These detection techniques apply to most forms of particle dark matter, and they function the same way regardless of the model. It is not necessary to restrict our discussion until we proceed to the actual calculations, which require model-specific parameters.

Searches for WIMP dark matter assume that there is some interaction between the WIMP and $\mathcal{SM}$

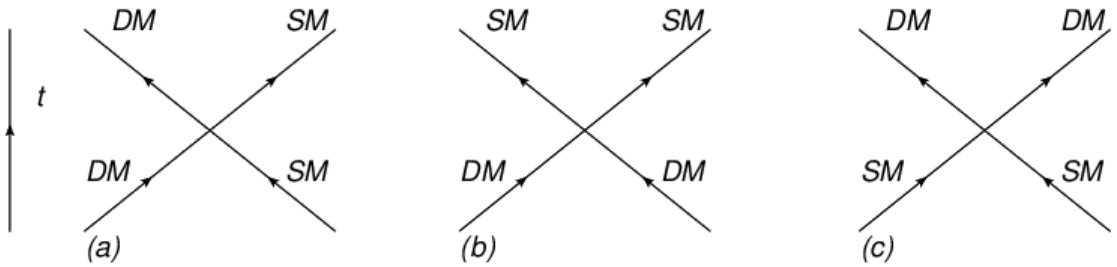

Figure 1.3: Dark Matter Detection

matter other than the gravitational. In terms of quantum field theory, these interactions can be of three different types.

The first kind of experiment is called a direct search for dark matter, utilizing the scattering interaction in Figure 1.3a. In this case, a WIMP scatters off of a $\mathcal{SM}$ particle through some unknown mechanism, and the $\mathcal{SM}$ particle recoils. With appropriate experimental design, this recoil can be observed and measured. Searches of this type are considered in Chapter 3.

In the second case, two WIMPs annihilate and produce a pair of $\mathcal{SM}$ particles, as in Figure 1.3b. This kind of interaction assumes that the WIMPs annihilate to $\mathcal{SM}$ matter, but that is the case for most of the WIMP models in the literature. Many of the annihilation products are too short lived to produce a detectable signal, or any signal they do produce has too high a background to be useful, but a few of them are promising. Searches for these kinds of annihilation signals are called indirect searches.

For an annihilation product to be suitable for an indirect search, it needs to be detectable, stable, and have a managable background. Stability rules out most hadrons and charged leptons in generations higher than the first, as well as the W, Z, and Higgs bosons. Confinement means that any quarks or gluons produced quickly hadronize. The background for protons, neutrons, and electrons is very high, making them less than ideal. What remains are photons, stable baryon and electron antimatter, and neutrinos. We examine each of these separately.

The photon is simple enough to detect, and its propagation is straightforward, but it has a highly intrusive background spectrum. Nearly all astrophysical objects emit photons, and this happens all across the energy spectrum. A careful background analysis is required before any claim of a signal can be verified. WIMP dark matter tends to produce a signal in the deep gamma energy range, at the GeV scale, where the background is potentially manageable. This kind of indirect signal is discussed in Chapter 4.

Antimatter detection requires the use of space-based detectors to get any clear signal, and such detectors have only recently started to take data. Usual signals sought include those from positrons, antiprotons, and antideuterons. Positrons and antiprotons tend to be more favorably produced, but the antideuteron background is much lower, making a signal easier to extract. Propagation is far more of an issue, since charged particles interact with the interstellar medium and the galactic magnetic field in a highly nontrivial way. Chapter 5 contains details on antimatter indirect signals.

Perhaps the most complicated of these indirect signals to compute is the neutrino signal. The neutrino is a particle that interacts only very weakly with regular matter, making detection quite difficult. Neutrino propagation is also fairly complex, since neutrinos oscillate between flavor states as they travel, a fact which has been ignored in most previous analyses of neutrino signals. In terms of background, the neutrino is better off. While processes in the universe do produce neutrinos, the majority of those are far below the WIMP annihilation product energy range. The most overwhelming background for terrestrial detectors is that of atmospheric neutrinos, which covers all of the energy range. Atmospheric neutrinos result when certain cosmic rays interact with the particles in the upper atmosphere. While direct annihilation to neutrinos is fairly rare in most WIMP models, most of the actual annihilation products are unstable and decay rapidly through leptonic channels, many producing neutrinos as they do. Neutrino signals have many difficulties, but they have a lot of potential as well, which will be seen when they are considered in Chapter 6.

The final means of interaction, shown in Figure 1.3c, is when two $\mathcal{SM}$ particles annihilate or fuse to create WIMPs. Given the generally high masses of WIMPs, these processes have a decently high energy threshold for lighter $\mathcal{SM}$ particles. While it is possible these interactions occur in astrophysical events and other natural high energy processes, those are not very useful for us in terms of dark matter searches. Having high energy collisions that can be repeated and observed as closely as we want is something that is very helpful to particle physics, and is the motivation behind the construction of particle collider experiments.

Work on the production of WIMPs in colliders now focuses mostly on the Large Hadron Collider (LHC) in CERN, due to negative results over the last two decades at lower energy colliders. A WIMP search in a collider experiment is a rather difficult prospect, as WIMPs are difficult enough to detect in ultra clean environments like direct detectors, let alone in the particle kaleidoscope that gets produced in the interaction region of a high energy collider. One can search for WIMP production by looking for missing energy, the energy that went into the collision but was used to produce WIMPs and so is not visible in the collision products. Alternatively one can look for model dependent bremsstrahlung type effects from freshly produced WIMPs.

Collider WIMP searches provide a valuable means of checking WIMP model parameters, and they are discussed in Chapter 7.

The three processes of scattering, annihilation and pair production provide complementary means of searching for a WIMP signal, and all are being pursued by many collaborations around the world, in both theoretical and experimental contexts.

Chapter 2

The Scalar Singlet Model

This thesis examines the possibility that the dark matter phenomenon can be described by a physical model, to be detailed in this chapter. The basic motivation is minimality; that is, to extend the $\mathcal{SM}$ of particle physics in a minimal fashion to explain the gravitational observations making up the dark matter problem. The most extreme of the minimal dark matter models is the scalar singlet model, which we explore here. This idea has been considered several times in the past, and even now provides a baseline model for WIMP dark matter.

2.1 Model Construction

Within the $\mathcal{SM}$ only the Higgs field, due to the symmetries of the electroweak gauge theory and renormalizability constraints, is capable of a renormalizable coupling to $SU(3)_c \times SU(2)_L \times U(1)_Y$ gauge singlet fields. No other $\mathcal{SM}$ particles have this property, and so such singlet fields would be capable of interacting with the $\mathcal{SM}$ only through gravity or a Higgs boson mediated Yukawa interaction. This interaction between hidden fields and $\mathcal{SM}$ particles has been called the 'Higgs portal.' The existence of such singlet fields contradicts no known physical principles and indeed, Occam's razor suggests we explore minimal models before more complex constructions. In the literature, these singlets have been referred to as phantoms, phions or darkon.

Though multiple singlet fields are possible, and have been proposed [46], we restrict ourselves for simplicity to a single field. Likewise for simplicity, we take it to be real and scalar, generating a spin-0 bosonic particle. Due to the weakness of its Higgs mediated interactions with $\mathcal{SM}$ matter, this singlet is a natural candidate for dark matter.

There are certain conditions any potential form of particle dark matter must satisfy. It must be electromagnetically neutral (dark), satisfy thermal constraints to produce the present observed abundance, be stable on cosmological time scales, and have a sufficiently weak nongravitational interaction with $\mathcal{SM}$ matter, as it has not yet been observed. The singlet is a $\mathcal{SM}$ gauge singlet, and so is neutral by definition. It has no fixed parameters, so it can be fit to the required thermal constraints with little effort. These calculations, detailed in Section 2.4, actually provide additional constraints on the model parameters. The Higgs field couples very weakly to the first generation of $\mathcal{SM}$ particles, so if the Higgs-singlet coupling constant is taken to be small enough, the interactions between the hidden and standard sectors can be made as weak as required. The

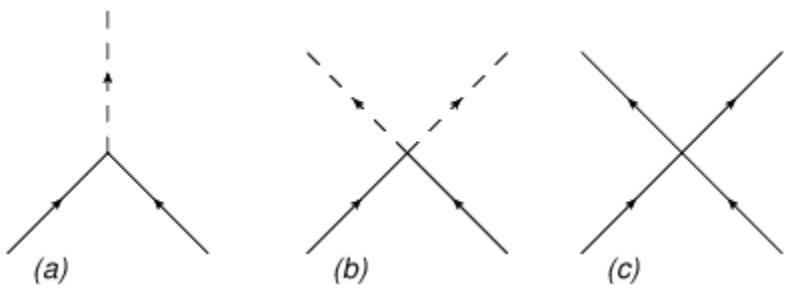

Figure 2.1: Phantom sector interaction verticies

stability requirement can be ensured by hand at very little cost. So the singlet satisfies the basic requirements of a dark matter candidate, but whether or not it satisfies the experimental bounds currently being set is the focus of this thesis.

The most general renormalizable Lagrangian that fits the theory while retaining gauge and Lorentz invariance as required is as follows:

$$\mathcal{L} = -\frac{1}{2}\partial_\mu S \partial^\mu S - \frac{m_0^2}{2}S^2 - \frac{\lambda}{4}S^4 - \eta S^2 H^\dagger H - \frac{\lambda_h}{4}\left(H^\dagger H\right)^2$$

This Lagrangian is an extenstion of the Higgs sector of the $\mathcal{SM}$ Lagrangian. S is the singlet field, m_0 is the bare mass of the singlet field, and H is the $\mathcal{SM}$ Higgs doublet. The constants η and λ are respectively the coupling constant between the Higgs field and the singlet field and the singlet field self-coupling constant. The constant λ_h is the Higgs field self-coupling constant. This Lagrangian has been proposed before [26] [46]. To ensure stability on a cosmic time scale, a discrete $\mathcal{Z}_2$ symmetry is imposed. Under this symmetry, which can be thought of as a parity, the singlet field transforms as $S \to -S$, allowing singlets to be produced and destroyed only in pairs, while everything else is even. Preservation of this symmetry is important, so we must include in the Lagrangian only terms that preserve it. This is the reason for the lack of an S^3 term.

After breaking the electroweak gauge symmetry and using the Higgs mechanism to generate $\mathcal{SM}$ particle masses, we can write the scalar part of the Lagrangian in the unitary gauge as

$$\mathcal{L} = \frac{1}{2}\partial_\mu S \partial^\mu S - \frac{m_0^2}{2}S^2 - \frac{\lambda}{4}S^4 - \frac{\eta}{2}S^2\left(h^2 - v_h^2\right)^2 \tag{2.1}$$

In this Lagrangian, the transition to unitary gauge has introduced h, the physical Higgs boson, with v_h the vacuum expectation value of the Higgs field, taken to be 246 GeV. We can read off from the interaction terms any Feynman rules we require for calculations. Vertex diagrams of the three interactions are in Figure 2.1, with (a) and (b) representing the Higgs-singlet interactions, which determine the $\mathcal{SM}$ interactions of the hidden sector. Of these, we neglect the S^4 term (Figure 2.1c), as it does not affect the detection phenomenology of the model in any significant fashion. The term governs singlet self-scattering events only, and these are not constrained by observation or experiment.

The scalar potential of this Lagrangian can be examined to gain constraints on the coupling parameters. For this, we follow the analysis of Burgess et al [26]. The Lagrangian generates a scalar potential of the form:

$$V = \frac{m_0^2}{2}S^2 + \frac{\lambda}{4}S^4 + \frac{\eta}{2}S^2\left(h^2 - v_h^2\right)^2 + \frac{\lambda_h}{4}\left(h^2 - v_h^2\right)^2$$

Simple analysis shows that the potential is bounded from below if λ and λ_h are both ≥ 0 and their product $\lambda_h\lambda \geq \eta^2$ for negative η. If no minimum exists, then there is no ground state and the model is of no use in describing dark matter. We assume the existence of a lower bound on the potential.

When considering the minima of V, we keep two things in mind. Particle masses in the $\mathcal{SM}$ are generated by the Higgs mechanism, which requires a nonzero Higgs vacuum expectation value. We wish to retain this mass generation feature in our modified Lagrangian, to ensure compliance with current phenomenology, and to avoid having to postulate some other mass generation mechanism. So to make sure the electroweak gauge symmetry is still broken, we require that $h \neq 0$ at the minimum. Similarly, the assumption of singlet longevity requires that the discrete $\mathcal{Z}_2$ symmetry remain unbroken. Since this symmetry takes $S \to -S$, this means $S = 0$ is required at the minimum. In the $\langle S\rangle \neq 0$ case, the singlet fields and the Higgs fields begin to mix, yielding some potentially interesting but far more complex variations. This case is not considered here, but is mentioned in the literature [106]. The vacuum expectation value requirements are then $\langle h\rangle \neq 0$ and $\langle S\rangle = 0$.

The derivative of the potential V is zero (a stationary point) for $h \neq 0$ and $S = 0$ if and only if $v_h^2 > 0$, in which case the point is an extremum with $\langle h\rangle^2 = v_h^2$, which is what we need to retain the Higgs mechanism. This extremum is furthermore a minimum if and only if $m_0 + \eta v_h^2 > 0$, indicating the physical singlet mass is positive. This is the minimum we seek.

A second minimum can exist if $\eta > 0$ and $\eta^2 < \lambda_h\lambda$, and if $m_0^2 < 0$ and $-\eta m_0^2 > \lambda\lambda_h v_h^2$. This minimum occurs at $\langle h\rangle = 0$ and $\langle S\rangle^2 = -m_0^2/\lambda$. As mentioned above, this minimum presents interesting possibilities, but makes things far more complex.

In the case that both minima exist, the first is the global minimum if $0 < -m_0^2 < v_h^2\sqrt{\lambda\lambda_h}$. We therefore assume that this is the case, and that this minimun is the true vacuum. These assumptions give us that an extremum with $\langle h\rangle \neq 0$ and $\langle S\rangle = 0$ both exists and is a minimum, and that that minimum is the global minimum of the potential. These assumptions ensure that as little as possible is changed from the $\mathcal{SM}$.

As a result of symmetry breaking, we shift $h \to h + v_h$ for h the physical Higgs boson with mass $m_h^2 = \lambda_h v_h^2$. This leads to the singlet dependent part of the potential being written in the form:

$$V = \frac{1}{2}\left(m_0^2 + \eta v_h^2\right)S^2 + \frac{\lambda}{4}S^4 + \frac{\eta}{2}S^2h^2 + \eta v_h S^2 h$$

The first term is the singlet mass term, providing a physical singlet mass of $m_S = m_0^2 + \eta v_h^2$. The second term is the singlet self-interaction term, and the last two terms represent the SSh and $SShh$ interaction vertices between the singlets and Higgs bosons.

The model is characterized by three parameters: the singlet mass m_S, which has been taken to be the mass of the physical particle and not the bare mass that appears in the mass term of the Lagrangian m_0,

the singlet self-coupling constant λ, and the Higgs-singlet coupling constant η. Neglecting the S^4 term in the Lagrangian means λ is also neglected, as it only affects singlet self interactions, which are irrelevant for detection. We require that $\lambda < 1$ to guarantee that perturbation theory is still valid. The addition of only three parameters to the $\mathcal{SM}$ is a demonstration of the minimality of the scalar singlet model.

The phenomenology of the model also depends on the as yet undetermined Higgs boson mass m_h, of course. The viable mass range for the Higgs was, until recently, quite large, spanning nearly 100 GeV. This would nessecitate studying the singlet model by taking an appropriate range of values for m_h and dealing with each individually. That no longer appears to be necessary. As of this writing, the bounds for a single Higgs boson in the SM have drawn to a mass range of a few tens of GeV, with a 95% confidence interval. Additionally, a signal has been observed at the CMS and ATLAS detectors attached to the LHC that could indicate the presence of the Higgs boson at approximately 124 GeV [29]. While it is certainly possible that the Higgs mass is outside of this range, we will choose for definitness the specific value of 124 GeV. We note here that throughout the thesis, we write most masses and momenta in natural units ($\hbar = c = 1$), leaving eV as the unit of mass. The exceptions are obvious.

The renormalizability of the theory was recently examined in great detail by Gonderinger et al. [61]. They demonstrate the renormalizability of the theory and construct an effective 1-loop potential for the theory, from that calculating the β functions, as well as the singlet self-energy and singlet corrections to the Higgs self-energy. They also discuss how varying the coupling constants can have an effect on thermal relic abundances. While their work is interesting, it does not affect our study of the phenomenology in a significant fashion.

The main attraction of the scalar singlet model is its fundamental simplicity. By extending the parameter space of the $\mathcal{SM}$ by two degrees of freedom, the dark matter problem can be solved. Such simplicity is rarely found in alternate models, which often require dozens or even hundreds of new degrees of freedom. This model was not created with any attention paid to aesthetics, or with an eye to solving other standing problems in particle physics. It is extremely narrow in focus, addressing only the phenomological concern that is the dark matter problem.

The model is in some ways a generic dark matter model, providing a nessecary contrast to more complicated models, which allows a more comprehensive interpretation of the data. The singlet model is very easy to pull predictions from, and is also rather easily falsified. As a consequence of its extremely simple structure, indirect detection signals in particular are expected to be different from those of more complex candidates like the neutralino.

It should be noted here that while the scalar singlet is considered solely in the context of dark matter in this thesis, the possibility of Higgs portal hidden sectors remains even if the singlet does not turn out to account for the dark matter. While in this case the phenomenology would be minimal, it is still an interesting theory. The extension of the singlet to an entire hidden sector is also occasionally considered in the literature.

2.2 Annihilation Cross Sections

To calculate the thermal relic densities in the next section, as well as to consider indirect signals in subsequent chapters, we require the annihilation cross sections of the singlet. We have taken the singlet to be its own antiparticle, and so it self-annihilates to $\mathcal{SM}$ particles with a frequency governed by η, the coupling to the Higgs field. This is because any interaction with $\mathcal{SM}$ particles must be through the Higgs portal, and so these annihilation events occur through an intermediate Higgs.

There are three basic cross sections to consider: annihilation to fermions, annihilation to massive vector bosons, and annihilation to Higgs bosons. Since the Higgs does not couple directly to photons or gluons, annihilation to the massless gauge bosons only begins to occur at the 1-loop level, and so is suppressed. We can obtain approximate annihilation cross sections for these supressed channels with little effort by using an effective field theory. An effective Lagrangian introduced by Shifman and some collaborators many years ago [119] allows tree level couplings between the Higgs boson and massless gauge bosons. The calculations using these effective interactions are present in the Appendix, and their results justify ignoring these annihilation terms.

Also note that there is no direct annihilation to neutrinos. While it is certain that neutrinos have nonzero mass, whether or not that mass is of Dirac or Majorana type is unknown, and so the $\mathcal{SM}$ as is does not include a Higgs-neutrino coupling. To avoid getting into the details of neutrino mass generation, we take that approximation. If neutrinos were given Dirac mass, their production as a result of singlet annhilation would be given by the same cross section as the other fermions (2.2), while the form for Majorana neutrinos would be somewhat different. Regardless of the mass type, experimental bounds on neutrino masses are so small that any Higgs-neutrino coupling is essentially nonexistent, allowing us to ignore such a term. Further details on neutrino production in singlet annihilation are in Chapter 6.

Since the parameters in our model vary over such a wide range, we restrict ourselves to the leading order cross sections. These cross sections are presented below, while the calculations are presented in the Appendix.

The fermion and vector boson product cross sections are s-channel processes only, while Higgs production involves the s-, t-, and u-channels, as well as the $SShh$ vertex.

$$v\sigma_{SS\to ff} = \eta^2 \frac{N_c m_f^2}{4\pi m_S^3} \frac{\left(m_S^2 - m_f^2\right)^{3/2}}{\left(4m_S^2 - m_h^2\right)^2 + m_h^2\Gamma_h^2} \tag{2.2}$$

$$v\sigma_{SS\to WW} = \eta^2 \frac{\sqrt{m_S^2 - m_W^2}}{4\pi m_S^3} \frac{3m_W^4 - 4m_W^2 m_S^2 + 4m_S^4}{\left(4m_S^2 - m_h^2\right)^2 + m_h^2\Gamma_h^2} \tag{2.3}$$

$$v\sigma_{SS\to ZZ} = \eta^2 \frac{\sqrt{m_S^2 - m_Z^2}}{8\pi m_S^3} \frac{3m_Z^4 - 4m_Z^2 m_S^2 + 4m_S^4}{\left(4m_S^2 - m_h^2\right)^2 + m_h^2\Gamma_h^2} \tag{2.4}$$

$$v\sigma_{SS\to hh} = \eta^2 \frac{\sqrt{m_S^2 - m_h^2}}{16\pi m_S^3} \left| \frac{2m_S^2 + m_h^2}{4m_S^2 - m_h^2 + im_h\Gamma_h} - \frac{2\eta v_h^2}{2m_S^2 - m_h^2} \right|^2 \tag{2.5}$$

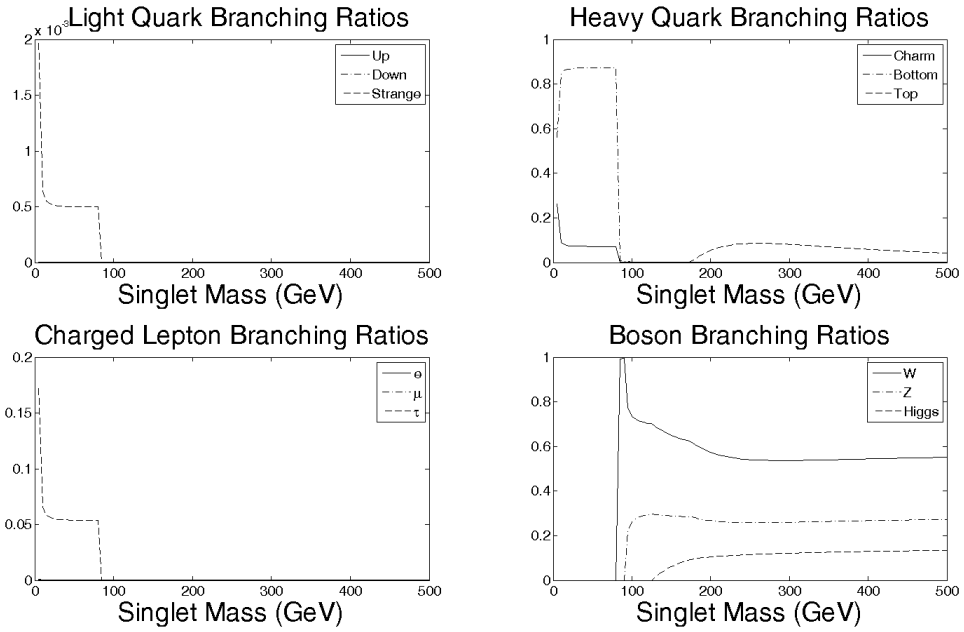

Figure 2.2: Singlet Annihilation Branching Ratios ($\eta = 0.1$)

The factor of two difference between the W and Z production cross sections is because the Z is its own antiparticle. The mass of particle species x is denoted by m_x, the decay width is denoted by Γ_x, and the factor N_c counts color and is 3 for quarks and 1 for leptons. In this model $\Gamma_S = 0$. Other variables are as labelled in the Lagrangian (2.1). In Figure 2.2 and 2.3 are plots of the singlet annihilation branching ratios as a function of singlet mass. We note the sharp difference in branching ratios before and after the W boson annihilation channel opens up at $m_S = m_W$. This allows us to divide the singlet mass range into basically two regions: light and heavy, where $m_S = m_W$ is the boundary. For light singlets, the annihilation products are nearly all bottom quarks (>90% most of the time), with the charm quark and τ lepton at less than 10% for most of the light mass range. There is also a per mille level contribution from the strange quark channel. As soon as the W channel opens, it dominates, lowering slightly as each new heavy particle channel opens before finally settling at about 60%. The Z boson channel accounts for about one quarter of all annihilations from its opening onward. The Higgs and top quark channels contribute at the 10% level or so. There is also an interesting feature in the branching ratio for $\eta = 0.3$ at the Higgs mass m_h =124 GeV, where the Higgs production cross section peaks due to the resonance between the Higgs and singlet masses.

The total velocity scaled annihilation cross section as a function of singlet mass is plotted for both values of η in Figure 2.4, with a zoomed version on the interesting region from 50 to 110 GeV in Figure 2.5. The difference in cross sections due to η is simply a matter of scaling. The scaling is not entirely quadratic in η as one might expect, but it is fairly close. As is usual with multichannel annihilation cross sections, there are peaks centered on the masses of produced particles. These resonances are a consequence of the increased probability of the process occuring when there is little excess energy. There is also a huge resonance at the

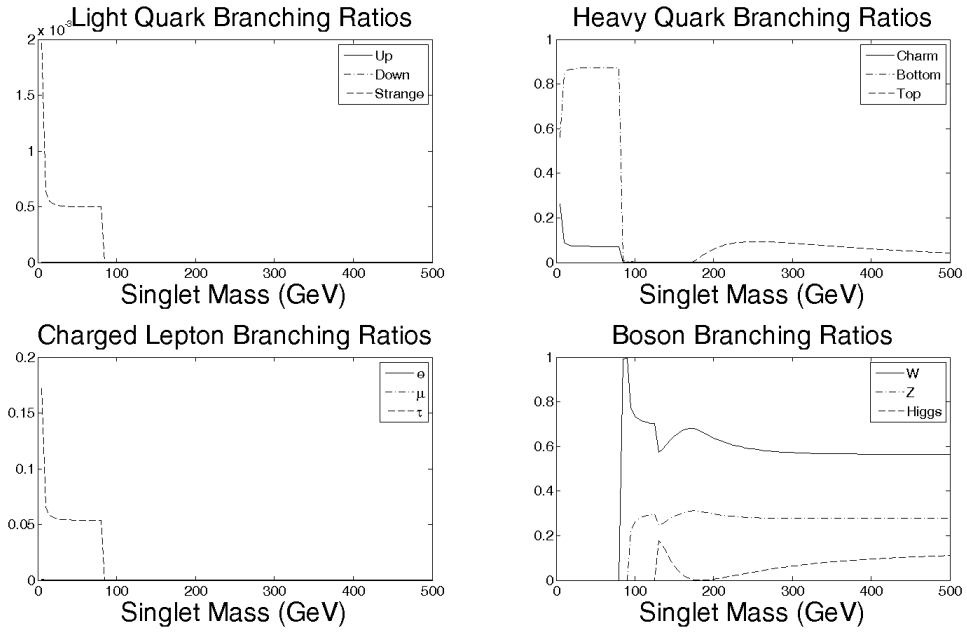

Figure 2.3: Singlet Annihilation Branching Ratios ($\eta = 0.3$)

value of $m_h/2$. This resonance is present because all annihilations proceed through an intermediate Higgs boson, and when that virtual Higgs is very nearly on mass shell the probability of the process occurring increases dramatically. The resolution of the plot does not quite capture the full magnitude of the peak, which increases to 10^{-18} cm^3/s, for either value of η.

2.3 Thermal Relic Density Calculations

One of the strongest constraints that can be placed on a dark matter model is that it must be able to account for the presently observed abundance. If one considers the dark matter to be a thermal relic, a species of roughly constant abundance since it emerged from thermal equilibrium in the early universe, then one can use Lee-Weinberg theory [86] to calculate the present abundance that the model would generate based on its annihilation cross section. We have obtained, primarily due to the data from the WMAP satellite [82], a reasonably accurate value for the dark matter mass density of the universe. We observe the present abundance to be $h^2\Omega_{dm} = 0.228$, which corresponds to an energy density of $\varrho_{DM} = 1.106\ keV/cm^3$, so this constrains the annihilation cross section and the parameters of the model on which it depends. In this section we perform the standard thermal relic density calculations for the scalar singlet and show how the present abundance restricts its parameter space. This is a review of material that has been published several times [110] [94] [26] [46].

After inflation, the singlets and $\mathcal{SM}$ matter were in thermal and chemical equilibrium, forming a primordial soup. This state continued as long as the thermal interactions of the singlets could maintain their

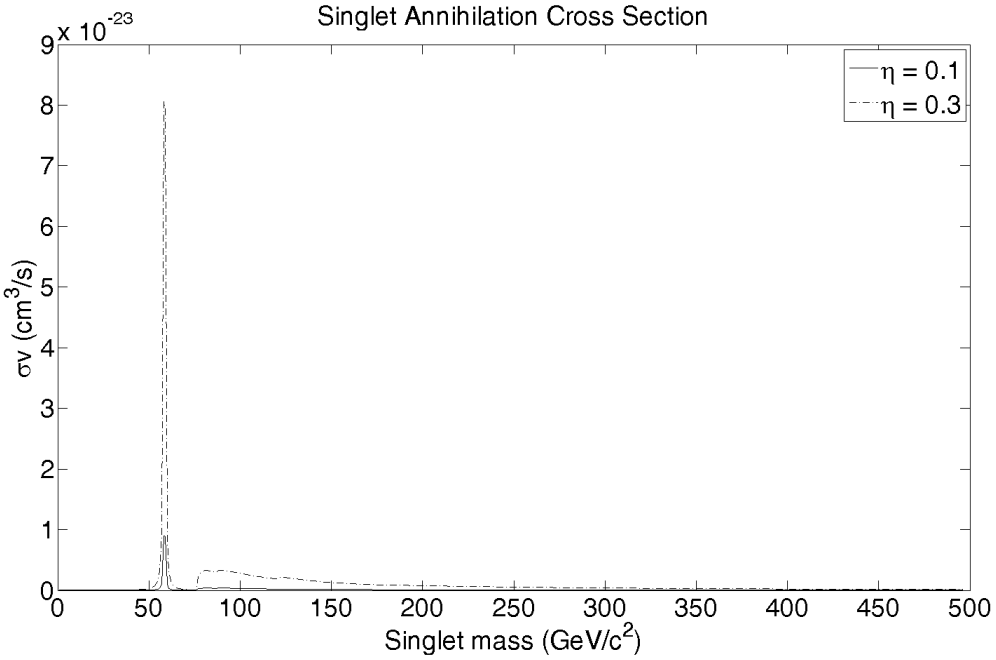

Figure 2.4: Singlet Annihilation Cross Section σv

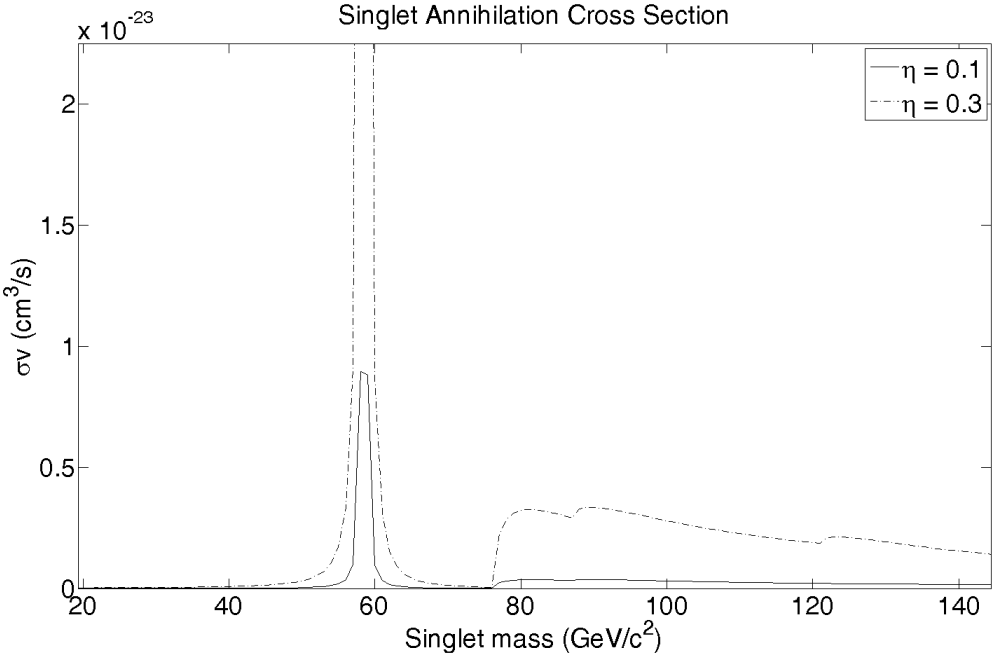

Figure 2.5: Singlet Annihilation Cross Section σv (zoomed in version)

frequency in the face of the expanding universe. Once the Hubble expansion of the universe reduced the frequency of singlet interactions with $\mathcal{SM}$ matter to a degree that they fell out of thermal equilibrium, the amount of singlets in the universe was to a large degree determined. The temperature at which the singlets dropped out of equilibrium is called their 'freeze-out' temperature. This temperature fixes the singlet abundance in terms of the model's parameters. Since the amount of singlets in the universe should not have been able to change appreciably since then, it should match what we observe.

To be able to make this comparison, we must first solve the rate equation for the singlets, which governs how the number of singlets changes over time. The equation is

$$\frac{dn}{dt} = -\frac{3n}{2t} - \langle \sigma v \rangle \left(n^2 - n_0^2\right).$$

We have n as the singlet number density, n_0 as the equilbrium density of singlets and $\langle \sigma v \rangle$ as the thermal average of the velocity scaled singlet annihilation cross section. The first term on the right hand side governs expansion, and the second governs annihilation events. This equation is in time t, but in the early universe, it is more convenient to work in terms of temperatures T than in terms of times, as the cooling of the universe as time went on is understood. We assume that radiation is dominant during singlet freeze-out, which allows us to use the relation $t = b/T^2$, with the parameter $b = \frac{3\hbar m_{Planck} c^2}{\pi k_B^2}\sqrt{\frac{5}{2g^*(T)}} = 3.41 \times 10^{19} sK^2$. The constants m_{Planck} and k_B are the Planck mass $m_{Planck} = \sqrt{\frac{\hbar c}{8\pi G}}$ and Boltzmann's constant $k_B = 8.6173$ eV/K. The function $g^*(T)$ describes the degrees of freedom of the primordial mixture at the temperature T. For $m_S < T < m_W$, $g^*(T) = 91.5$.

Transforming t to T, we can write the rate equation as

$$\frac{d}{dT}\frac{n}{T^3} = 2b \langle \sigma v \rangle \frac{n^2 - n_0^2}{T^6}.$$

Lee and Weinberg [86] proposed the following approximation for the equilibrium density

$$n_0(T) = \frac{1}{2\pi^2 (\hbar c)^3} \int_0^\infty dK \frac{\left(K + mc^2\right)\sqrt{K\left(K + 2mc^2\right)}}{\exp\left[\left(K + mc^2\right)/k_B T\right] - 1}$$

which holds until the freeze-out temperature T_f is reached, defined by the condition, called the Lee-Weinberg condition, that

$$\frac{d}{dT}\left.\frac{n}{T^3}\right|_{T=T_f} = 2b \langle \sigma v \rangle \frac{n_0^2(T_f)}{T^6} \tag{2.6}$$

If we assume that $T_f \ll m_S$, as is usually the case in the timeframe of interest, then

$$n_0(T) = \left(\frac{1}{\hbar}\sqrt{\frac{m_S k_B T}{2\pi}}\right)^3 \exp\left(-\frac{m_S c^2}{k_B T}\right).$$

We seek to transform the Lee-Weinberg condition into a more useful form. Radiation dominates after inflation until $t_{eq} \simeq 2.4 \times 10^{12}$s. The rate equation changes depending on whether the radiation dominance assumption is in effect, due to the relative strength of the expansion term:

$$\frac{dn}{dt} = \begin{cases} -\frac{3n}{2t} - \langle\sigma v\rangle n^2 & if \quad t_f < t < t_{eq} \\ -\frac{3n}{a}\frac{da}{dt} - \langle\sigma v\rangle n^2 & if \quad t > t_{eq} \end{cases}$$

where $a(t)$ is the scale factor in the Robertson-Walker metric. The initial condition is that $n(t_f) = n_0(T_f)$.

It can be shown [46] that the expansion term $\frac{3n}{a}\frac{da}{dt}$ dominates over the annihilation term $\langle\sigma v\rangle n^2$ for $t > t_{eq}$. This allows us to neglect the annihilation term and write

$$n(t) = n(t_{eq})\left(\frac{a(t_{eq})}{a(t)}\right)^3 \quad for \quad t > t_{eq}$$

If we define the variable $\xi = m_S c^2/k_B T_f$, we can rewrite the Lee-Weinberg condition (2.6) in the more useful form

$$\exp(\xi) = \frac{2bk_B m_S c^2}{\left(\sqrt{2\pi}\hbar c\right)^3}\langle\sigma v\rangle \frac{\sqrt{\xi}}{\xi - 1.5}$$

$$= 4.18 \times 10^{11}\frac{\langle\sigma v\rangle}{10^{-24}cm^3/s}\frac{m_S c^2}{100GeV}\frac{\sqrt{\xi}}{\xi - 1.5} \tag{2.7}$$

where the physical constants have been combined and scaling factors for $\langle\sigma v\rangle$ and m_S have been inserted.

For the region $t_f < t < t_{eq}$, the rate equation can be solved to give

$$n(t_{eq}) = \left\{\frac{1}{n(t_f)}\left(\frac{t_{eq}}{t_f}\right)^{\frac{3}{2}} + 2\langle\sigma v\rangle t_f\left[\left(\frac{t_{eq}}{t_f}\right)^{\frac{3}{2}} - \frac{t_{eq}}{t_f}\right]\right\}^{-1}$$

$$\simeq \frac{n(t_f)}{1 + 2\langle\sigma v\rangle t_f n(t_f)}\left(\frac{t_f}{t_{eq}}\right)^{\frac{3}{2}}.$$

The approximation follows from T_f being a few GeV, which follows from the Lee-Weinberg condition above, leading to $\sqrt{\frac{t_{eq}}{t_f}} > 10^9$. We can then use the radiation domination assumption and the definition of ξ to write

$$t_f = \frac{b}{T_f^2} = \frac{bk_B^2}{m_S^2 c^4}\xi^2 = 2.53 \times 10^{-11} \times \left(\frac{100GeV}{m_S c^2}\right)^2 \xi^2 s$$

$$\Rightarrow \langle\sigma v\rangle t_f = 2.53 \times 10^{-11} \times \left(\frac{100GeV}{m_S c^2}\right)^2 \xi^2 cm^3 \frac{\langle\sigma v\rangle}{10^{-24}cm^3/s}.$$

The Lee-Weinberg condition gives

$$n(t_f) = \left(\frac{m_S c}{\hbar\sqrt{2\pi\xi}}\right)^3 \exp(-\xi) = \frac{m_S^2 c^4}{2bk_B^2\langle\sigma v\rangle}\frac{\xi - 1.5}{\xi}$$

which implies that

$$2\langle\sigma v\rangle t_f n(t_f) = \xi - 1.5$$

$$\Rightarrow n(t_0) = n(t_{eq}) z_{eq}^{-3}$$

for the factor

$$z_{eq} = \frac{a(t_0)}{a(t_{eq})} - 1 \simeq \frac{a(t_0)}{a(t_{eq})} \approx 3000$$

We combine the above equations to arrive at the singlet energy density at the current time

$$\varrho_S = n(t_{eq}) m_S c^2 = \frac{2\xi - 3}{2\xi - 1} \xi \frac{k_B \sqrt{b}}{2 \langle \sigma v \rangle t_{eq}^{3/2} z_{eq}^3}$$

$$\simeq \frac{2\xi - 3}{2\xi - 1} \xi \times \frac{2.51 eV/cm^3}{\langle \sigma v \rangle / (10^{-24} cm^3/s)} \tag{2.8}$$

We want $\varrho_S = \varrho_{DM} = 1.106\ keV/cm^3$ for the singlets to satisfy the observed dark matter density. With this, the above equation (2.8) determines ξ in terms of $\langle \sigma v \rangle$ and the substitution into the Lee-Weinberg condition (2.7) relates $\langle \sigma v \rangle$ and m_S, which is also a relation between m_S and η. We do not present the numerics here; the results are available in the literature [110] [94] [26] [46].

Of course, to obtain numbers for this solution, we need to calculate the thermally averaged annihilation cross section $\langle \sigma v \rangle$. We can use the nonrelativistic annihilation cross sections computed in the previous section with the substitution $m_S^2 \to (m_S + K)^2$, where K is the kinetic energy of the singlet. Assuming a standard thermal distribution, we have

$$\langle \sigma v \rangle = \frac{\int_0^\infty dK \frac{(m_S+K)\sqrt{K(2m_S+K)}}{\exp[(m_S+K)/T]-1} \sigma v(K)}{\int_0^\infty dK \frac{(m_S+K)\sqrt{K(2m_S+K)}}{\exp[(m_S+K)/T]-1}}$$

The kinetic energy dependent cross section $\sigma v(K)$ is the sum over the spectrum of $\mathcal{SM}$ particles of the cross sections $\sigma v_{SS \to SMSM}$ under the above substitution. It has been shown in the literature [46] that for the singlet thermal annihilation cross section, $\langle \sigma v \rangle \simeq \sigma v$, as the temperature T affects the result only up to a constant factor of $\mathcal{O}(1)$. So we can use the basic annihilation cross section instead of the thermal average. We have included only contributions from the cross sections $\sigma_{SS \to WW}$, $\sigma_{SS \to ZZ}$, $\sigma_{SS \to tt}$, $\sigma_{SS \to hh}$, $\sigma_{SS \to bb}$, $\sigma_{SS \to \tau\tau}$, and $\sigma_{SS \to cc}$. The others are small enough in our mass ranges that they can be safely neglected, as can be seen from the branching ratios plotted in Figures 2.2 and 2.3.

2.4 Singlet Halo Distributions

To perform any calculations, we must first specify how the singlets are distributed in the region of interest. For the galactic fluxes we will study, this means the Milky Way galaxy. The study of dark matter distrubutions is a lively field, producing more detailed simulations every year. Of course, since dark matter itself is still hypothetical, our understanding of dark matter mass distributions is far from perfect. In this section we outline the assumptions that have been made about the singlet distribution.

Structure formation arguments and many body simulations indicate that galactic dark matter forms a spherical halo that surrounds the disk of the galaxy. The halo is approximately spherically symmetric, so we can describe the mass density as a function of radius only. Such a radially dependant mass distribution is called a halo mass profile, usually denoted $\rho(r)$. For a generic dark matter particle of mass m_{DM}, the profile can be related to the number density $n(r)$ by the simple relation $\rho(r) = n(r)m_{DM}$. The mass profile is poorly constrained by observations, so its form mostly relies on simulations of gravitational collapse. In the past few decades, simulations of the scale nessecary to achieve any kind of accuracy ($10^6 - 10^9$ particles) have become possible, allowing parameterizations of mass profiles to be created and used as tools in dark matter calculations.

In the 90s, Navarro, Frenk and White ran a series of simulations for various structure types and found that they could parameterize profiles in the form [99]

$$\rho_{NFW}(r) = \frac{\rho_0}{(r/r_s)\left(1 + r/r_s\right)^2}$$

with ρ_0 and r_s parameters of the halo and r the radial variable. This form is not scale independent, but holds for any size of halo. This form has become the defacto standard profile for dark matter research, called the NFW profile.

There are other profiles that have been proposed as well. Some examples include the Moore profile [98]

$$\rho_{Moore}(r) = \frac{\rho_0}{(r/r_s)^{1.5}\left[1 + (r/r_s)^{1.5}\right]}$$

which was obtained by similar methods to the NFW profile, or the isothermal profile

$$\rho_{iso}(r) = \frac{\rho_0 r_s^2}{r^2}.$$

The isothermal profile is a simplistic model that was used before N-body simulations of this magnitude were available. This profile is a poor approximation, not meeting the expected r^3 behavior at large radii. A modern profile that may be taking the place of the NFW as the standard is the Einasto profile [96] [51].

$$\rho_{Einasto}(r) = \rho_0 \exp\left[-\frac{2}{\alpha}\left(\frac{r^\alpha - r_s^\alpha}{(25kpc)^\alpha}\right)\right]$$

where the parameter $\alpha = 0.17$ for the Milky Way. The Einasto profile is defined by a logarithmic relation and was originally applied to modelling other astrophysical systems, like galactic kinematical systems.

All profiles presented here are roughly similar in form, as can be seen in Figure 2.6. They all also break down in the galactic core region, diverging as $r \to 0$, which is why we have omitted that region from the plot. This is in direct contradiction to evidence that indicates the halo should have a roughly constant mass distribution in the core region, as well as the assumption that there is no dark matter singularity at the center of the galaxy. This inconsistency is believed to be caused by the limiting resolutions of earlier simulations (only a few million particles), and the situation in the core is becoming clearer with more recent simulations (a few billion particles) [114].

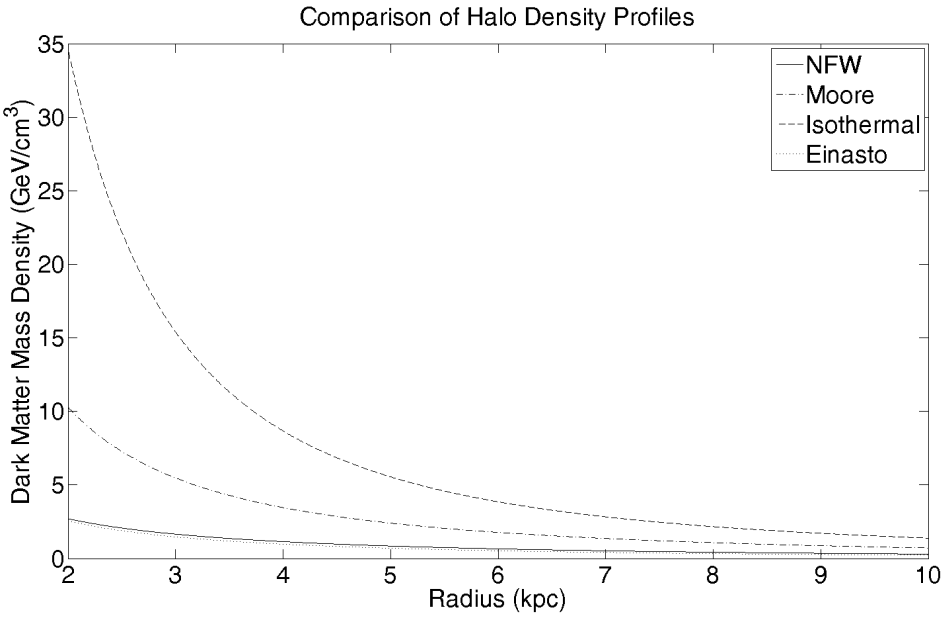

Figure 2.6: Dark Matter Halo Profile Comparison (Milky Way parameters used)

At this point, the only two profiles being used consistently in the literature are the NFW and Einasto profiles. The NFW is being slowly phased out as recent simulations suggest the Einasto provides a better fit to the collapse data. As can be seen from the comparison figure, those two profiles are very close for the Milky Way. We have chosen to work with the NFW profile. The core region of the halo is less of a concern than the outer regions, and the halo profiles are close in value in the outer regions. This also allows a better comparison with previous work in the area, most of which used the NFW profile. Choosing a different profile would affect the results to a minor degree, but not the overall structure of the computed quantities.

It should be noted here that the above mentioned simulations indicate there is potential for a substantial amount of substructure to be present in the galactic halo. By this we mean regions of more or less mass density than the profile indicates for that radius. While the general trends appear to fit the above profiles, local structure may vary considerably. Substructure effects can significantly alter annihilation rates and hence annihilation signals. Substructures are quite complicated, and a detailed analysis would be quite beyond the scope of this thesis. As such, we ignore substructures. At this level of treatment, until halo substructure is better understood, this is the natural solution.

2.5 Singlets in the Literature

The scalar singlet model is frequently present in the literature, perhaps because of its simplicity and ease of use, and is often used as a basic model with which one can examine new observational results or consider new detection techniques. We present here a brief outline of appearances the model has made in the literature. While an attempt at exhaustiveness has been made, it is unlikely to have succeeded. There are no doubt

many other papers that treat the model that are not included here. Nonetheless, the most important that have appeared in preprint form before the end of 2011 are present.

The model was first proposed by Silviera and Zee [110] in 1985 as a solution to the cold dark matter problem. They briefly considered the construction of the singlet fields, then proceeded to perform some relic density calculations. The model was extended to a complex singlet field in 1994 by MacDonald [94], where the thermal relic properties were recomputed and consideration was given to indirect neutrino signals from the annihilation of singlets captured by massive bodies. The treatment was perfunctory, as there was no way of detecting such neutrinos at that time.

Around the turn of the millenium, the first generation of dark matter detection experiments were on the verge of producing results, and a number of papers were published considering the scalar singlet model in this context. MacDonald [95] and Zee [76] extended their previous work, while Burgess [26] and Bento [17] considered nuclear recoils and neutrino signals.

Over the next few years, several papers were published that used singlets in a different context than dark matter, or that treated them only tangentially. Some groups gave a basic description [43] [100], while one considered singlets in the context of perturbative unitarity [42] and others in the context of mixing with the $\mathcal{SM}$ Higgs [106] or with sterile neutrinos [84]. The paper that came up with the term 'Higgs portal' was a brief survey letter that was written in 2006 [101].

Around the middle of the decade, as the LHC began nearing completion, the particle physics community began publishing literature making predictions about a variety of theories that the LHC data could shed light on. Of course, the dark matter problem was no exception. As an additional boost, several direct detection experiments reported negaive results over these years, placing firm bounds on recoil cross sections. This led to much speculation, as many models and regions of parameter space were excluded. There was discussion of singlet signals from gamma rays [122] [46], from antimatter [63], at the LHC [12] [73], and from nuclear recoils [72]. There were also extensions of the model [52] [21].

In 2009, the CDMS collaboration announced that they had seen two candidate events during their latest run [5]. While this is a small number, and they have since been deemed background events, this was the first reported direct detection of dark matter outside of the modulation signals observed long ago. This led to further publications, exploring the implications of the findings. Several papers concerning singlets were published in reponse to this report [54] [6] [71]. As of this writing the CDMS collaboration has not yet reported any further results.

Finally, the most recent round of results from direct detection experiments have led to more literature on scalar singlets. There was an update of direct detection analysis [67] and a discussion of the first XENON100 results [53], as well as an extension to explain inflation [87]. Preliminary results from the LHC also led to the publishing of at least one paper [74].

At this time, the literature on indirect detection of singlets is somewhat lacking. This is somewhat made up for by the fact that many of the papers that are published in the context of indirect detection are

model-independent, and so present results that can be applied to nearly any model with little effort, but a treatment of scalar singlet annihilation signals from antideuterons or extragalactic gamma rays does not yet exist. Further, no treatment of neutrino signals which takes recent results and oscillations into account exists for scalar singlet dark matter.

Chapter 3

Nuclear Recoil Signals of Singlets

The cornerstone of the particle dark matter search is the direct detection experiment. Any candidate that is excluded by bounds placed due to direct searches is finished, and any positive signal from a different kind of experiment needs to be confirmed by direct searches before it can be accepted. There are a large number of direct detection experiments, even though this kind of experiment has little use other than its stated purpose. That so many resources have been put into these searches is a testament to how important they are considered to be.

The basic physics behind WIMP direct detection relies on the idea that WIMPs interact with $\mathcal{SM}$ matter in some fashion beyond the gravitational. This interaction is expected to be very small, smaller even than the weak force interactions, and any experimental design seeking signals of this interaction needs to be considered with this in mind. The method employed by current direct search experiments is to look for the nuclear recoil that occurs after a WIMP has scattered elastically from a nucleus.

As we have no reliable way of producing WIMPs, we must rely on the local WIMP flux passing through the solar system. WIMPs are part of the Cold Dark Matter paradigm of cosmology and so are believed to have nonrelativistic velocities, with recent estimates suggesting a distribution of some kind, often taken to be Gaussian, with a mean at ~ 220 km/s. Such slow moving WIMPs carry very little momentum, and so any nuclear recoil resulting from a collision with one of these ambient WIMPs would be miniscule. Recoils on this scale tend to be overwhelmed by the thermal motion of the detector material, leading to a background that is subdued by keeping the detector very cold.

The literature on the subject of direct detection is vast. Each experiment of course puts out its own series of design papers, and each model of dark matter usually has a discussion of direct detection as applied to itself. A thorough review of direct detection and reviews of many of the experimental setups that will be discussed in the next section is available in the recent book compiled by Bertone [22].

3.1 Experiments

In this section, we provide a brief overview of the physics behind the direct detection of WIMP dark matter.

There are a few ways to detect the actual nuclear recoil. The main method of recoil detection involves scintillation photons. The energy deposited by the WIMP can go into the creation of an excited state, which

decays while emitting a photon. These photons will have characteristic energies dependent on the properties of the material the detector is made of. Similarly, the energy may instead liberate an electron from the atom, ionizing it. In this case, the electron drifts through the material with an energy related to that deposited by the WIMP. These two channels are often used together to provide more information about the recoil.

In crystal structures thermal vibrations can be treated as quantized pseudoparticles known as phonons. Energy can be transmitted through the crystal lattice by these phonons, and detected at the edge of the crystal. The nuclear recoil energy from a WIMP collison event can also be transmitted in this way, and this presents another detection channel that is available only in very low temperature crystal structures.

One of the properties of a WIMP model that can severely affect its direct detection properties is how it couples to nuclear matter. Certain kinds of WIMP interact with the spin of nucleons as well as their mass. This makes the effective coupling to the whole nucleus different from the spin independent case. In the spin independent case, the coupling to all of the nucleons in the nucleus is the same, leading to A (the mass number of the nucleus) scattering amplitudes which add coherently to give a total cross section proportional to A^2. In the spin dependent case, the coupling changes sign based on nucleon spin, so contributions from paired nucleons in the nucleus tend to cancel each other out, leaving only contributions from unpaired nucleons. Because of this, only nuclei with odd numbers of protons or neutrons can detect spin dependent interactions. So the detector material must be chosen to optimize detection of spin dependent or spin independent interactions. There are some models of dark matter that have different spin independent couplings to protons and neutrons, which complicates the nuclear recoil cross section considerably. A review is available [55], but we do not mention isospin violating dark matter any further.

There are three basic types of WIMP direct detection experiment in operation, with a fourth in development. Each is described in the following.

First we have what are called cryogenic detectors. The cryogenic detectors of today are the successors to the cold superconductor experiments of the 1980s that were used to look for neutrinoless $\beta\beta$ decay. Those same experiments served as a 'generation zero' for direct dark matter detection. These old experiments had no way of discriminating between electron and nuclear recoil, which have quite similar signals, making them quite unreliable. Modern cryogenic experiments, such as CRESST or CDMS, consist of Germanium or Silicon crystals cooled to mK scale temperatures. The main advantages of cryogenic detectors is their ability to measure the nuclear recoils in terms of temperature changes, through phonons propagating through the crystal lattice. The phonon pulse structure can be used to determine a rough location for the recoil, allowing positional discrimination. To correct the inability to distinguish electron and nuclear recoil that the old single channel detectors had, many cryogenic detectors use electrons that are ionized by the recoil as a second channel.

Next there are noble liquid detectors. As their name implies, they are made with a large amount of cooled liquid noble elements, like Xenon or Argon, with exceptional purity. Examples of this kind of detector include ArDM, LUX, and the XENON series of experiments. When a recoil occurs within the detector

material, both ionization and excitation can occur. The excited state decays, emitting a scintillation photon with a characteristic wavelength that is not absorbed by the liquid. The ionized electron propagates through the fluid, causing photons to be emitted when it interacts. Some detectors detect only the scintillation photons, while others look for the ionization signal as well. The dual phase detectors allow for electron recoil discrimination and much better location resolution. An in-depth review of Xenon based detectors, with much of the physics applicable to other liquids, has been written [10].

The third kind of direct detector in operation is the superheated gas detector, and is also the least common kind. PICASSO [44] is an example of a detector of this type. The idea behind these detectors is similar to bubble chamber experiments as seen in particle physics. The detector material is a superheated gas which undergoes a phase transition when energy is deposited in it, producing bubbles. The bubbles can then be tracked through the material. Temperature and pressure variation can be used to discriminate against electron recoils. Additionally, they do not need to be so cold, so they can use materials that are more sensitive to spin dependant interactions, allowing better probes of the parameter space.

The final type of detector is called a directional detector. In addition to detecting the presence of WIMPs, these experiments will be able to determine the direction in which those WIMPs are travelling. None of these experiments are even in construction as of this writing, however. The proposed projects, such as DARWIN, are still in the prototype testing phase. DARWIN itself will be a scintillation-based dual channel noble liquid detector, which will take directional data through detailed analysis of events. Its high spatial resolution will make such analysis possible, as well as allowing for detailed background event discrimination. A review of the DARWIN project is available [14], and it includes details of both design and function.

A somewhat different approach is taken by the DAMA and CoGeNT collaborations. Rather than looking for a clear signal, they look for an annual modulation in the overall data they do pick up. The Sun and its accompanying planets are orbiting the center of the galaxy and are believed to be moving through the dark matter halo with a relative velocity of a few hundred km/s. This implies that as the Earth orbits the Sun it travels faster through the halo during one half of its orbit than during the other half. Since the detection rates are related to the motion of the WIMPs through the detector material, the relative motion of the Earth through the halo should change the signal that is picked up throughout the year. This method is still a direct detection experiment, and both DAMA and CoGeNT in all their incarnations are cryogenic experiments, but it allows for a much greater background tolerance, because most of the background is filtered out. Of course, picking out an actual signal is still difficult.

Many years ago DAMA reported observing such an annual modulation signal [20], and despite much criticism, they have never gone back on their claim. Recently CoGeNT reported a confirmation of the signal observed by DAMA [1], indicating the detection of a low mass WIMP. Both of these results are in conflict with many of the currently running experiments, leading to contradictory bounds.

3.2 Backgrounds and Uncertanties

Direct detection of WIMPs is a difficult task, since the background is several orders of magnitude greater than the actual signal. The main backgrounds are caused by natural radioactivity of material nearby and by cosmic rays.

To avoid the first, detectors are built from the least radioactive material possible, and knowledge of the exact radioactive proportions of the components is required to take into account the decays that occur during data analysis. Often the experiment goes so far as to purge radon from the air. Cosmic rays are usually blocked by placing the experiment far underground to use the crust of the Earth as a shield. These measures are not perfect, however, so most experiments use an active veto to reject events that occur too close to the edges of the experiment, reducing the actual mass available for data collection. The active veto also rejects multiscattering events, which are highly unlikely to be caused by WIMPs.

Despite the above precautions, there will be many background recoil events. This means it is necessary to have some way to discriminate between different kinds of recoils. In particular, neutrons are bad. There is no way to tell the difference between a WIMP induced nuclear recoil and a neutron induced one. Low energy neutrons can be blocked by water shielding, and high energy neutrons are usually produced by cosmic rays, so being underground and the use of active vetos attempts to account for them. It is impossible to remove the entirety of the neutron background though.

Electron recoils often generate similar signals to nuclear recoils. However, most backgrounds interact with electrons as much as with nuclei, which is not true for WIMPs. This can be used to discriminate between background and WIMP signals. The electron and nuclear recoils are distinguished in dual channel detectors as they produce different signal distributions. The details of these kinds of active discrimination and signal analysis can be found in the experiment details published by each individual collaboration, and a more general review of backgrounds in WIMP direct detection can be found as well [59].

Of course, though progress is made every year in reducing and accounting for the background signals, this cannot go on forever. In the depths of the low interaction region lies the neutrino background, which is absolute. There is no blocking neutrinos, and neutrino-nucleon deep inelastic scattering is a weak process, around the same scale as WIMP interactions. Solar neutrinos will totally blind us in certain energy regions, and atmospheric neutrinos can present a background over the entire energy spectrum.

There are several basic uncertainties that must be considered before interpreting the results of these experiments. Among them are astrophysical uncertainties about the dark matter profile, which is often taken to be the isothermal profile when doing calculations, and about the local dark matter density. There are also uncertainties in the backgrounds, but those are considered accounted for by the background supression methods listed above. Uncertainties in the properties detector material are also present, as are instrumental uncertainties, but those are specific to each experiment so we will not go into any further detail. A full discussion of the uncertainties that are present in direct detection experiments has been published as well

[93].

3.3 Singlet Nuclear Recoils

We now seek to find whether the singlet model is excluded by current direct detection results. To do this we must compute the nuclear recoil cross section for the singlet scattering and then compare it to these results, for various singlet masses to the bounds provided.

First we must find the singlet nucleon elastic scattering cross section. In the singlet model, describing nuclear recoil with field theory is in fact quite complicated. This is because the Higgs boson that mediates the scattering couples directly only to the quarks that make up the nucleons rather than the nucleons themselves. The majority of the mass of the nucleon is not found in its three valence quarks, but in the 'sea' of strongly interacting particles that surround those quarks. A naive attempt at dealing with the Higgs-nucleon coupling, taking only the valence quarks into account, is sure to describe only a fraction of the actual interaction. The behavior of the sea particles is still poorly understood, making exact calculations impossible.

To compute the way in which the Higgs boson couples to the nucleon, we are forced to compromise and work in an effective field theory. This allows us to include a term in the effective Lagrangian that acts as a Higgs-nucleon interaction, scaled by an effective coupling constant g_{hNN}, where the N fields are the nucleon fields

$$\mathcal{L}_{gNN} = -g_{hNN}\bar{N}Nh. \tag{3.1}$$

The initial calculation was done many years ago [109]. The reference can be examined for greater detail, but the basic idea behind the calculation is to take into account the Higgs boson coupling to the heavy quarks and gluons present in the sea, and use that to construct the effective Lagrangian. This basic treatment gives a dimensionless value of $g_{hNN} = 0.84 \times 10^{-3}$.

Unfortunately, this treatment is a bit too simple. In taking into account the strange quark content of the nucleon, the effective coupling can be greatly altered [30]. Again, more details are present in the reference, but including certain extrapolated experimental values for nucleon strange content can alter the value of g_{hNN} by a factor of up to 2.5. Modern experimental values of nucleon strangeness and lattice calculations indicate the nucleon strange content is far less than was estimated twenty years ago in the reference [117]. While there is certainly some strangeness in the nucleon, it appears to be very little, and so for simplicity we take the effective coupling constant to be $g_{hNN} = 0.84 \times 10^{-3}$, calculated assuming nucleon strange quarks do not contribute to the interaction. This effective coupling method is certainly not perfect, but as of this writing it remains the most complete treatment of a Higgs-nucleon coupling.

In this effective field theory, we can describe singlet-nucleon elastic scattering through a single s-channel tree level interaction. Due to the unknowns in the singlet model and uncertainties in the $\mathcal{SM}$, we do not advance the perturbation theory any further than first order. The Feynman diagram for the process is in

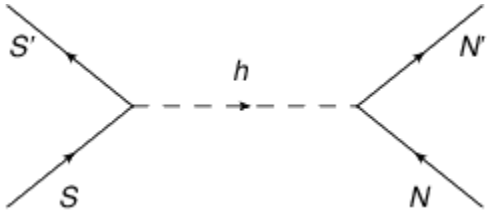

Figure 3.1: Singlet-nucleon Scattering Process

Figure 3.1. Since all nongravitational interaction between singlets and $\mathcal{SM}$ matter is through this Higgs portal, this is the only type of process that can be expected. The singlet is a scalar particle, and so the spin independant part of the cross section constitutes its entirety.

The relevant Feynman rules can be read off from the effective Lagrangian (3.1) and the model Lagrangian (2.1) from Chapter 2 as required. Evaluation of the matrix element and resulting scattering cross section in the nonrelativistic regime is quite simple, and is deferred to the Appendix. The result is

$$\sigma_{SN\to SN} = \frac{g_{hNN}^2 \eta^2 v_h^2}{8\pi m_h^4} \frac{m_N}{m_S} \ln\left(\frac{m_N + 2m_S}{m_N}\right)$$

The m_N, m_S, and m_h are the nucleon, singlet and Higgs masses, and v_h is the Higgs vacuum expectation value as before. The coupling constants η and g_{hNN} have also been explained.

This cross section is plotted in Figure 3.2 as a function of singlet mass for the mass range of 1 GeV to 1 TeV, assuming a Higgs mass value of 124 GeV. We plot it for $\eta = 0.05$, 0.1, 0.2, 0.3 to show the basic dependance on η, even though the Lee-Weinberg condition from Chapter 2 has made most of these values unlikely, and to show how the cross section changes over large ranges of singlet mass. The nucleon mass has been taken to be $m_N = 931.24$ MeV, the average nucleon mass in stable tungsten isotopes, and the Higgs vacuum expectation value is $v_h = 246$ GeV.

3.4 Experimental Bounds

Though there are several direct search experiments reporting bounds on nuclear recoil cross sections, we shall consider only a few. Our reasoning follows. First, only spin independent cross sections are relevant for singlet nuclear recoils, since the singlets are scalar particles. Experiments that are optimized for spin dependent recoils have no advantage over those that are not, for the purposes of singlet detection. Secondly, we consider the mass range that each experiment focuses on. Many collaborations are now working in the low WIMP mass range of a few tens of GeV, which does not allow for comparisons with higher mass singlet calculations. Finally, we look at those results that, when combined, provide the most complete picture of the current state of dark matter direct detection. Following these criteria, we have chosen to compare our calculations with results reported by the following groups: XENON100, CoGeNT, and CRESST. XENON100 was chosen because it currently reports the strongest contraints on nuclear recoil cross sections for a very

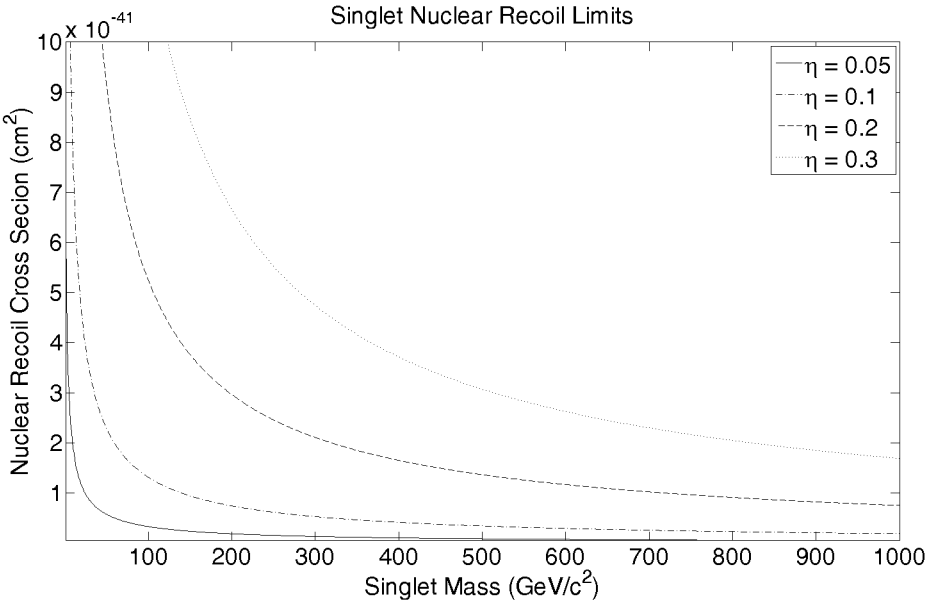

Figure 3.2: Singlet Nuclear Recoil Cross Section

wide range of masses. Similarly, CRESST was chosen because it has reported observing a positive recoil signal [8], though this observation appears to take place in a region already excluded by XENON100. We will discuss the tension between these two results later. For the final comparison, we sought to compare against a modulation signal, which meant a comparison against DAMA or CoGENT data. Both have observed positive modulation signals, but the data provided by CoGENT is more recent, as well as easier to obtain, so we proceed with using it. It so happens that these choices cover all three possible detection channels as well.

The XENON100 [9] experiment, as its name suggests, uses liquid xenon to look for WIMP induced nuclear recoils. The XENON series of experiments is a multi-decade endeavor, with the 100kg version extending the 10kg prototype that was completed in 2006. The XENON100 will, in turn, be replaced by the incoming XENON1T, which will contain a metric tonne of liquid Xenon. The XENON series are all dual channel detectors, detecting both scintillation photons and ionized electrons and comparing their time differences to differentiate between background events and WIMP recoils. Xenon scintillation photons appear at characteristic frequencies that are easy to observe, and an electric field is applied across the liquid to provide a drift of ionized electrons to the edge of the volume, where they can be detected. We show a plot of the most recently reported upper bounds on WIMP nuclear recoil cross sections from XENON100. We present it alone, as the calculated singlet cross sections are simply too different in magnitude for any meaningful visual comparison.

The CRESST-II [7] experiment is a liquid helium cooled cryogenic detector involving the use of scintillating $CaWO_4$ crystals. The detector modules are dual channel, involving scintillation photon and phonon detection. The energy of the recoil is primarily read from the phonon, with the photon being used mainly to discriminate

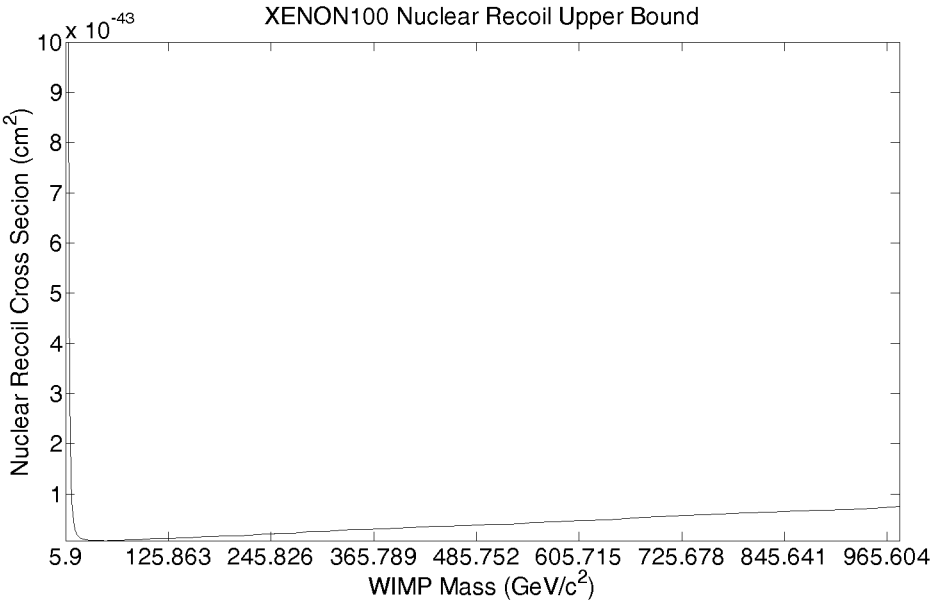

Figure 3.3: XENON100 Nuclear Recoil Cross Section Bounds

background events. The material provides attractive photon emission properties at low temperatures, allowing for better identification of background events, and combining this with the deep underground location, detector shielding, and active muon vetos gives the CRESST collaboration a certain amount of justified confidence in their claim that not all of the observed events could be caused by the background. Depending on the maximum likelihood formalism used, they calculate either a 4.7σ or 4.2σ statistical significance for rejecting that the 67 events observed were background events.

The collaboration has analyzed the events and produced a likelihood region on a WIMP mass-nuclear recoil cross section plot. We present in Figure 3.4 the 1σ and 2σ regions around their maximum likelihood points. Also in these figures is the calculated singlet nuclear recoil cross section. While the lower mass region of significance appears to be different from the computed singlet recoil cross section, the higher mass region contains the theoretical line to a significant degree. From this, we have consistency between the CRESST-II events and a low mass singlet of 20-50 GeV.

CoGeNT [2] is based around semiconducting germanium crystals, which provide better recoil signals for lower mass WIMPs. The experiments seeks an annual modulation signal, in an attempt to verify the DAMA claims. This kind of detector was originally proposed in the context of neutrino instigated nuclear recoils, but was adapted to WIMP detection. In Figure 3.5, we plot the most recent upper bounds on WIMP-nucleon recoil cross sections [1], in comparison with the calculated singlet recoil cross section. The CoGeNT bounds, being based on a modulation signal, are less strong than the bounds provided by the other experiments. We see that the scalar singlet recoil cross section is consistent with the CoGeNT bounds over a large mass range.

Any discussion of these results requires mention of the obvious tension between the XENON and CRESST

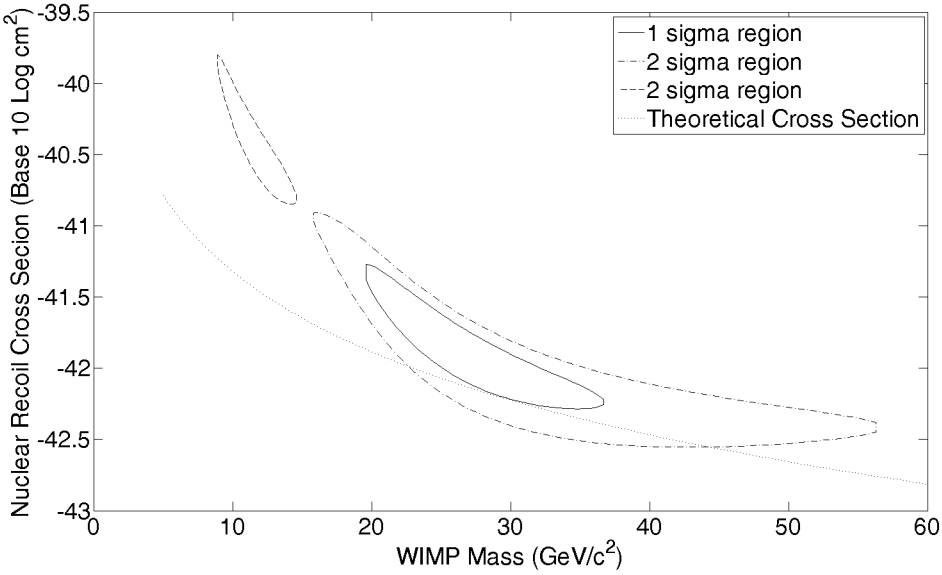

Figure 3.4: CRESST II Nuclear Recoil Region of Significance

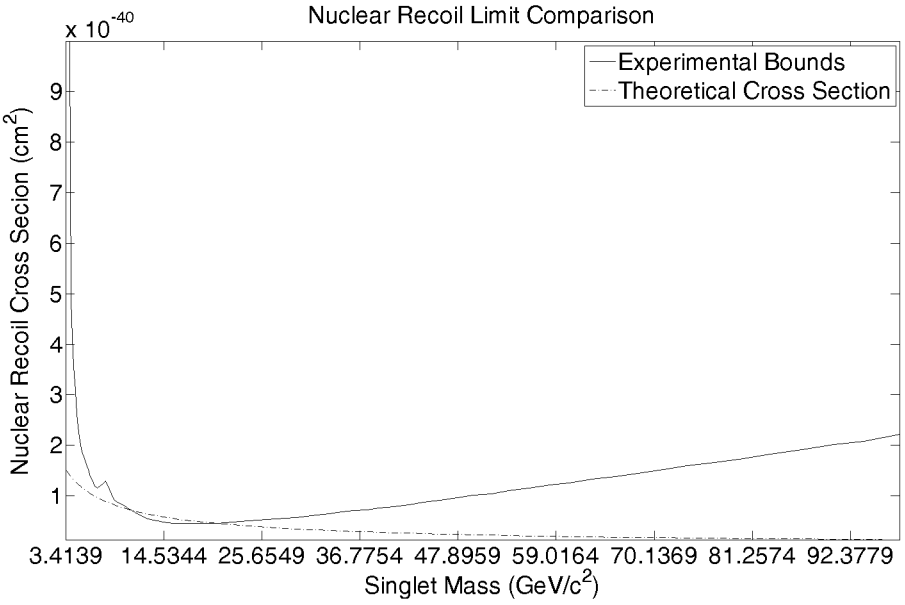

Figure 3.5: CoGeNT Nuclear Recoil Bounds

data sets. As can be seen by comparing the scales of the plots in Figures 3.3 and 3.4, the observed CRESST events are several orders of magnitude above the reported XENON100 upper bound. From this we must conclude that there are errors in the reported results of at least one of the two collaborations. The methodology of XENON has been called into question before [38], resulting in a heated debate [37] [39]. A full analysis of potential resolutions to this conflict is beyond the scope of this thesis. All that can be said is that the scalar singlet model remains viable for some of its parameter space according to the CRESST results, but it is no longer viable at all according to the XENON results. Our singlet interpretation of the CRESST signal has been submitted as a short letter and was accepted for publication [47].

Chapter 4

Gamma Ray Signals of Singlets

The most easily detected products of particle dark matter annihilation are without a doubt photons. For almost all of its existence, the science of astronomy has consisted of collecting photons from the sky, so this is hardly something new. The annihilation products of intermediate mass WIMP dark matter generally have energies on the 1-100 GeV scale, which means that produced photons are very high energy gamma rays.

Gamma ray signals are of great importance in determining which models of dark matter remain viable. Their ease of detection and the fact that photons propagate nearly freely through the galaxy mean that individual regions of the sky can be examined more closely if necessary to focus on areas with a higher expected annihilation signal, whether from increased dark matter density, or from decreased background. The propagation of photons is modified by scattering with charged matter, which is minimal at this energy scale due to the low density of the interstellar medium [103], by scattering with other photons, which is a second order loop effect and so negligible, and by gravitational lensing. The relevant galactic lensing effects only effect photons along a specific line of sight. The number of galactic lines of sight ending in a lens is finite, and not even very large, which means there is little effect on the propagation of gamma rays within the galaxy.

In this chapter we proceed to calculate the overall diffuse gamma ray flux at Earth from halo annihilations of scalar singlet dark matter. This is only one approach. Other possibilities include focus on certain regions like the galactic core or analysis of extragalactic objects like dwarf galaxies, or searching for diffuse exotic extragalactic signals. A more complete treatment would certainly use all of these means. This flux is dependent on the halo profile, though not to a large degree. For the sake of being definite, we use the NFW profile as described in Chapter 2.

4.1 Local Photon Flux

We now consider the annihilation of scalar singlets to photons. At tree level, there is no direct annihilation to photons. Decay of annihilation products to photons at secondary stages and beyond occurs, and makes for the majority of the total photon spectrum. Singlet to photon annihilation occurs at the 1-loop level, suppressed by tree level interactions, through the coupling of charged particles to the Higgs field. Analysis with effective Lagrangians, as detailed in the Appendix, as well as full loop order calculations, indicates that

this contribution can be neglected with little effect.

Many of the direct annihilation products are not color singlets, and so hadronize immediately, as dictated by confinement. This hadronization produces many unstable mesons and baryons which proceed to decay, producing many more photons. Hadronization is not yet fully understood, and the functions that describe how it occurs cannot be derived theoretically; they must be pulled from fits to phenomological data sets. Additionally, any charged particle that is produced can emit a bremsstrahlung photon and lose some of its energy. The hadronization and bremsstrahlung contributions to the photon primary spectrum are significant. The bremsstrahlung contributions are calculable, to a degree, but the hadronization effects are not.

To get around this, we follow Dick et al. [46] and Bergström et al. [19] and use a phenomological photon fragmentation function. This function describes the photon production by $\mathcal{SM}$ particles, and since it is a fit to experimental data, it includes hadronization and bremsstralung effects as well as decays. To be more accurate, it is a fit to a photon spectrum from dark matter annihilations computed with the software package `DarkSUSY` [62], which includes phenomological hadronization and bremsstrahlung effects as part of its routines. The average photon spectrum produced by energy E_{in} of $\mathcal{SM}$ particles can be parametrized as a function of the scaled variable $x = 2E/E_{in}$ by

$$\frac{dN}{dE}(E, E_{in}) = \frac{0.42 \exp(-8x)}{x^{1.5} + 0.00014}.$$

Since singlets annihilate exclusively to $\mathcal{SM}$ particles, we can obtain the average photon spectrum from singlet annihilations by setting $E_{in} = 2m_S$. This follows from conservation of energy in the nonrelativistic case. The photon spectrum is plotted in Figure 4.1. It exhibits no surprising features, but we note that the vast majority of photons are produced with energies less than 20% of the singlet mass. This treatment allows a vast simplification of calculation that would not be possible if we tried to take each individual effect into account, though possibly some software package could handle the job. Actual testing of the validity of the treatment must wait until an exotic photon signal has been identified.

The photon flux at Earth from galactic halo annihilations can be described by the integral

$$j = \int d^3\bar{r} \frac{1}{2} \frac{n^2(\bar{r})}{4\pi \left|\bar{r}_\odot - \bar{r}\right|} \frac{d\mathcal{N}_\gamma}{dE}(E, 2m_S) \frac{\sigma v}{4\pi sr} \tag{4.1}$$

The function $n(\bar{r})$ is the number density of singlets in the halo, related to the mass profile by $\rho(\bar{r}) = n(\bar{r})m_S$. It is squared to count collisions, and the factor of 1/2 is to avoid overcounting. The integration is over all points $\bar{r}$ in the galactic halo, with $\bar{r}_\odot$ as the distance of the solar system from the center of the galaxy. The annihilation cross section of the singlets is σv, as reported in Chapter 2, and then the photon production function $\frac{d\mathcal{N}_\gamma}{dE}(E, 2m_S)$ is identified with the $\mathcal{SM}$ photonic fragmentation function as described above. Technically the production spectrum should include a second term that describes direct annihilation to photons:

$$\frac{d\mathcal{N}_\gamma}{dE}(E, 2m_S) = \frac{dN}{dE}(E) + BR_{\gamma\gamma}\delta(E - m_S)$$

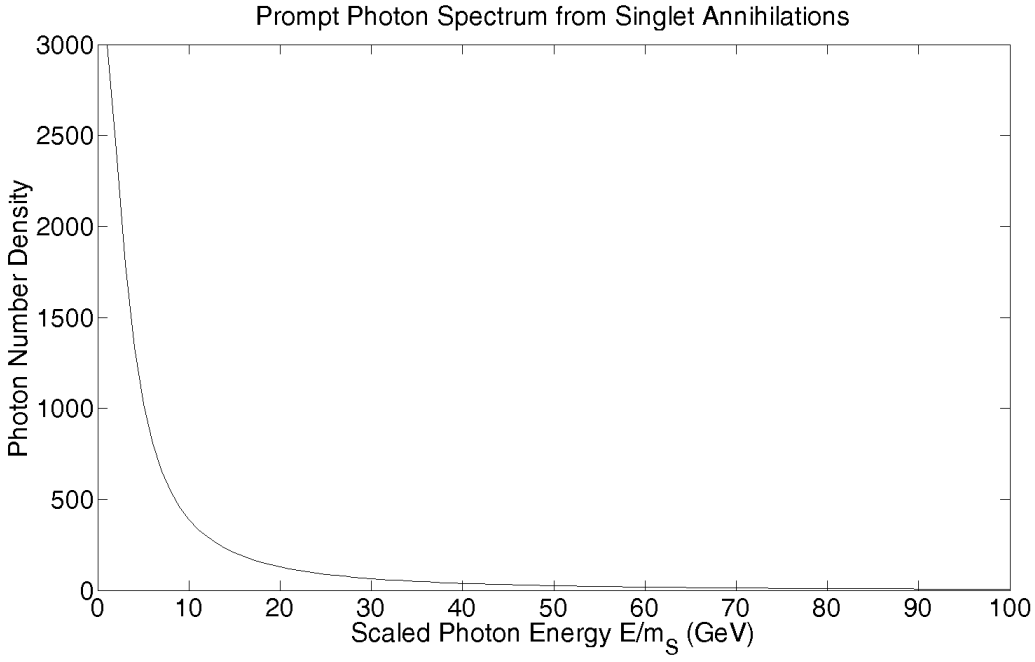

Figure 4.1: Photon Production Spectrum

with $BR_{\gamma\gamma}$ the branching ratio for annihilation to a pair of photons. We take this as insignificant, as the branching ratio is of the order 10^{-3} or less, depending on singlet mass. It produces a flux that is a few orders of magnitude less than the continuous spectrum. The irrelevance of such a term is somewhat unfortunate, as the direct annihilation peak in the gamma ray spectrum at the singlet mass would be a very clear signal of exotic annihilations, one that would be difficult to mimic. This could give something to search for, as well as providing strong bounds in its absence. Another term could be added to production function as well, representing secondary photons produced when antimatter annihilation products create gamma rays through inverse Compton scattering or annihilation with interstellar particles. The inclusion of these secondary photons is not implemented.

Using the NFW profile in a form which emphasizes the total halo mass $M = 5.41 \times 10^{64}\ TeV/c^2$,

$$\rho\left(r\right) = \frac{M}{\left(r/r_s\right)\left(1 + r/r_s\right)^2}$$

we can rewrite the flux (4.1) as an integral over the radial variable and solve it analytically.

$$j = \int_0^\infty dr \frac{r}{r_\odot} \ln\left(\frac{r + r_\odot}{|r - r_\odot|}\right) \frac{\rho^2(r)}{4m_S^2} \frac{d\mathcal{N}_\gamma}{dE}(E, 2m_S) \frac{\sigma v}{4\pi s r}$$

$$= \frac{M^2}{4m_S^2} \frac{d\mathcal{N}_\gamma}{dE} \frac{\sigma v}{4\pi s r} \frac{1}{r_\odot r_s^4} \times \left\{ \frac{\pi^2}{6} + dilog\left(\frac{r_s}{r_s + r_\odot}\right) + dilog\left(\frac{r_s - r_\odot}{r_s}\right) \right.$$

$$\left. + \frac{1}{2}\ln^2\left(\frac{r_s + r_\odot}{r_s}\right) + \frac{4 r_s r_\odot \left(2r_s^2 - r_\odot^2\right)}{3\left(r_s^2 - r_\odot^2\right)^2} - 2 r_s r_\odot \frac{9r_s^4 - 8r_s^2 r_\odot^2 + 3r_\odot^4}{3\left(r_s^2 - r_\odot^2\right)^3} \ln\left(\frac{r_s}{r_\odot}\right) \right\}.$$

We have defined the dilogarithm function as

$$dilog\,(x) = \sum_{n=1}^{\infty} \frac{(1-x)^n}{n^2} = \int_1^x dt \frac{\ln(t)}{1-t}.$$

We can insert the radial and mass parameters and evaluate the functions to obtain the expression

$$j = 1.95 \times 10^{14} \times \left(\frac{TeV}{m_S}\right)^3 \frac{d\mathcal{N}_\gamma}{dE}(E, 2m_S) \frac{\sigma v}{TeV\ cm^5 sr}.$$

Now we have an expression for the local photon flux at Earth from singlet annihilation. This flux is plotted for representative values of m_S in Figures 4.2 and 4.3.

In this theoretical flux, there are two main uncertainties, from the particle physics and astrophysics parts of the calculation. The particle physics uncertainties lie primarily in the term σv, which depends on the dark matter model, though it is constrained by the Lee-Weinberg condition (2.7). The astrophysical uncertainties lie in the dark matter halo profile, which was discussed in Chapter 2. These two factors together make calculations like this nessecarily exploratory in nature.

As mentioned in Chapter 2, we will not consider halo substructures. If we were to consider them, the gamma ray signal analysis is the analysis that would benefit the most from their inclusion. The other detection methods, aside from the direct detection signal, tend to be insensitive to halo structure to a large degree. The basic idea for the gamma signal is that if a region in the halo has a higher dark matter density than the profile suggests, it will also present a higher annihilation signal (recall from (4.1) that the photon flux from annihilation scales quadratically with number density). If the density is high enough, the region may present a gamma signal that is strong enough to distinguish it from the diffuse background. Such a positive signal would be a great step toward understanding dark matter, but no such signal has been identified yet. Further work with the scalar singlet model may take substructures into account.

4.2 Observed Flux

We compare our computed diffuse galactic flux to the gamma ray data gathered by the Large Area Telescope (LAT) aboard the Fermi satellite. The collaboration has published several reports on the observed gamma ray flux, allowing observation of the sky through the medium of gamma rays of energies in the range 20 MeV to 300 GeV. In addition to examining unknown gamma sources, one of the primary missions of the instrument is to measure the diffuse gamma spectrum. It is this aspect that is useful for comparing to calculations for diffuse gamma fluxes from dark matter annihilation.

We have chosen to work with the Fermi data because it currently provides the best picture of the diffuse gamma spectrum. It has far superior resolution to the EGRET telescope [115], and that it is space-based means that it has fewer problems observing gamma rays than ground-based telescopes do. While ground-based telescopes may be much larger in size than the LAT, that they are looking through the atmosphere requires them to be entirely different from the simpler space-based telescopes. Gamma rays certainly do not

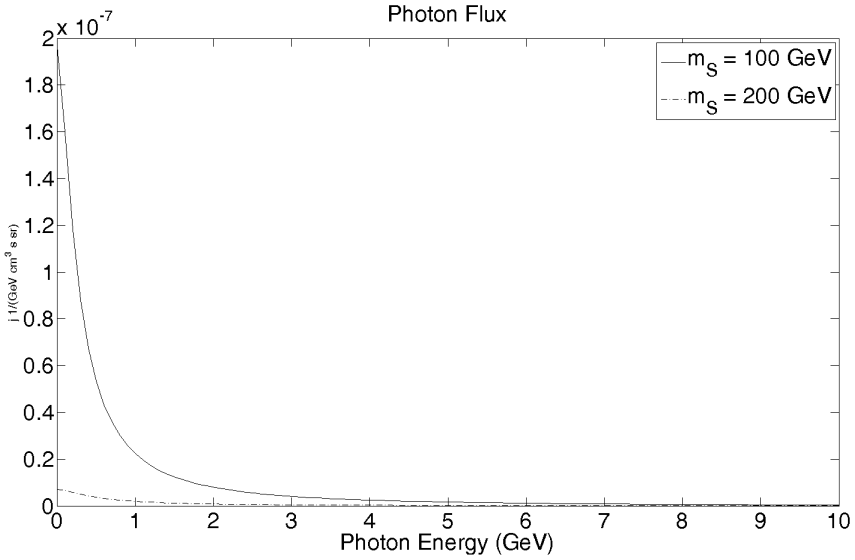

Figure 4.2: Photon Flux from Singlet Annihilation (m_S =100 GeV, 200 GeV)

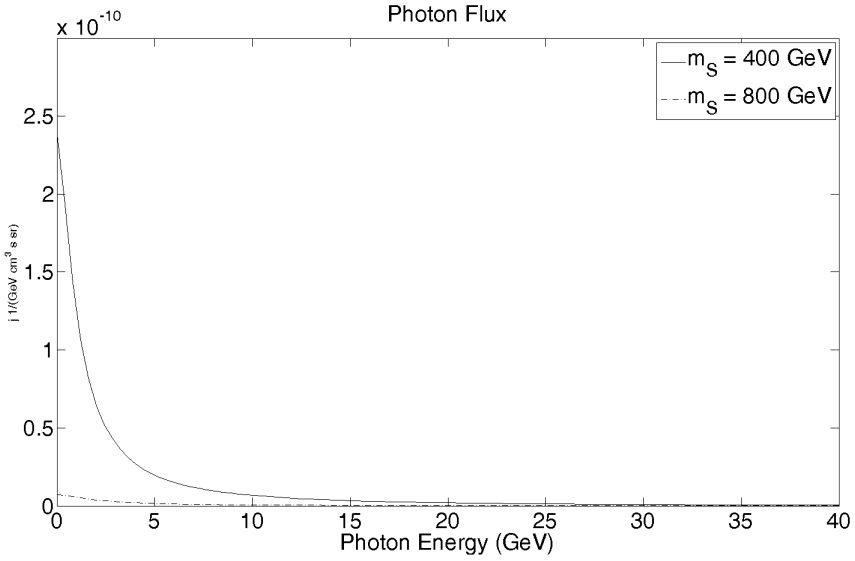

Figure 4.3: Photon Flux from Singlet Annihilation (m_S =400 GeV, 800 GeV)

penetrate the atmosphere to the surface of the Earth, so the ground-based telescopes look at the atmospheric showers that result from the initial contact. HESS [75], for example, is basically a Cherenkov detector. This necessity leads to larger backgrounds and loss of directional and energy data. The resolution is poorer, and more time is required to get the same picture. Additionally, ground-based telescopes have a fixed field of view, and cannot really perform wide-sky surveys, making measurements of the diffuse background difficult. The ground-based telescopes have their own advantages, but for our purposes the Fermi LAT data is obviously superior.

The basic mechanism behind the detection of the gamma rays in the LAT is simple. An incoming photon will hit a thin sheet of tungsten, and produce an electron-positron pair. The pair will traverse a series of silicon sheets, ionizing them and giving directional information. The pair is then absorbed by a cesium iodide crystal scintillation calorimeter, allowing a reading of the energy to be taken. There are several mechanisms in place to reject cosmic ray and Earth albedo backgrounds, but we will not go into further detail.

A brief discussion of the astrophysical gamma ray background may be in order. The main background for the examination of point gamma sources is the isotropic diffuse background, which is what is of interest to us as we look for a dark matter annihilation signal. This diffuse background could be made up of photons from unresolved point sources, from unnaccounted for galactic diffuse emission, or from the extragalactic background. The extragalactic background is poorly understood, but the consensus seems to be that much of it comes from energetic events in active galactic nuclei. There are also sources of device background, mostly due to charged cosmic ray interactions with the satellite or from mislabelling of charged particles as photons. These problems are taken into account by strict event selection criteria, which remove most of the offending data points.

The data set we use [56], reported in 2010, is presented as the extragalactic diffuse background. What the collaboration has done is to compute the gamma ray flux from the propagation of charged cosmic rays through the galaxy, which is the primary source of diffuse high energy photons, and compare this and several other secondary sources against the observed gamma flux. The galactic flux from the propagation of cosmic rays does not account for all of the observed diffuse gamma radiation, so the remainder is presumed to be from an extragalactic source. Since we know of no other galactic sources of diffuse gamma rays, this is not necessarily incorrect. Any gamma signal from the annihilation of dark matter must be present in this extragalactic diffuse background. The collaboration reports a smooth power law spectrum with an index of 2.41, and a total intensity of $I(>100\,MeV) = (1.03 \pm 0.17) \times 10^{-5}\ cm^{-2}s^{-1}sr^{-1}$ which implies their observed diffuse gamma ray spectrum can be fit to the function

$$j_{Fermi} = (1.03 \pm 0.17) \times 10^{-5} \times 1.41 \times \left(\frac{E}{0.1GeV}\right)^{-2.41} cm^{-2}s^{-1}sr^{-1}GeV^{-1}$$

We compare this reported flux against the flux computed from the annihilation of singlets in Section 4.1. This is done by plotting the flux ratios of j_{Theory}/j_{Fermi} for representative values of m_S and two values of η^2 for comparison, displayed in Figures 4.4 to 4.10. The gamma ray flux from singlet annihilation is seen to account for at most a few per cent of the extragalactic diffuse background, and for larger masses, this

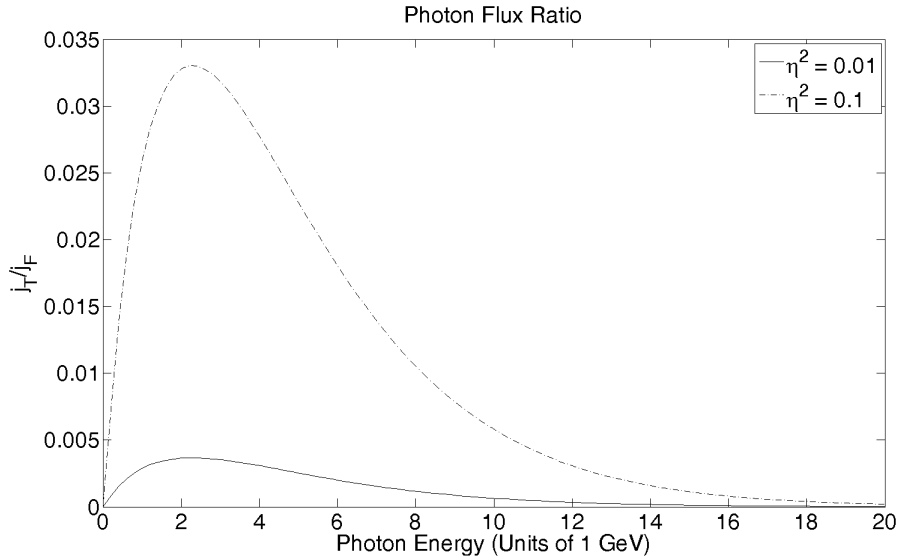

Figure 4.4: Gamma Ray Flux Ratio $j_{T/F}$ ($m_S = 20$ GeV)

reduces to the per mille level or less. Only one of these scenarios ($m_S = 50$ GeV, $\eta^2 = 0.1$) is ruled out by the observational data. While the remainder remain viable, they are also not especially useful in providing support for the scalar singlet model, sitting at the per cent scale that they do. The gradual peak that occurs between 10% and 20% of the singlet mass may be discernable once more of the actual background is accounted for, but it would simply provide evidence of some kind of exotic annihilation occuring with center of mass energies in that range. The theoretical photon flux may be compared to subsequent data sets, allowing continual evaluation of the model.

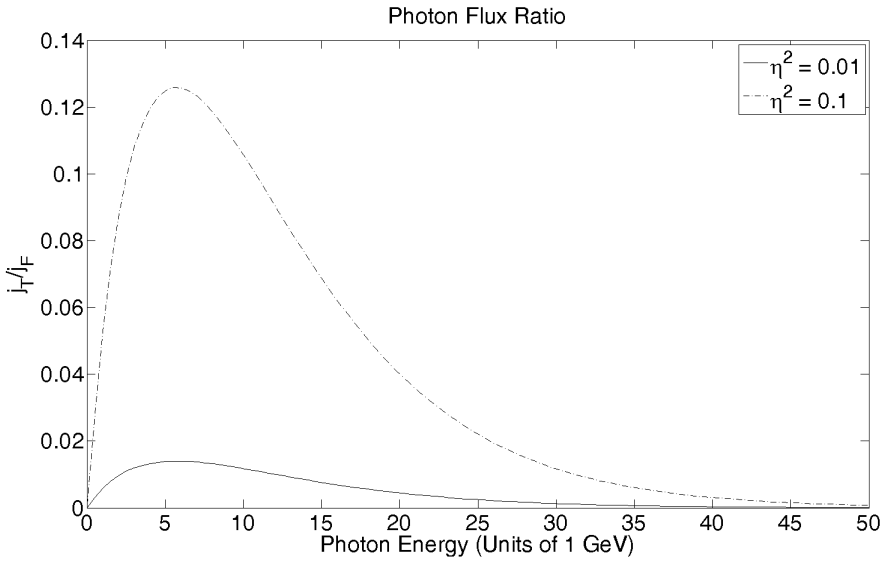

Figure 4.5: Gamma Ray Flux Ratio $j_{T/F}$ ($m_S = 50$ GeV)

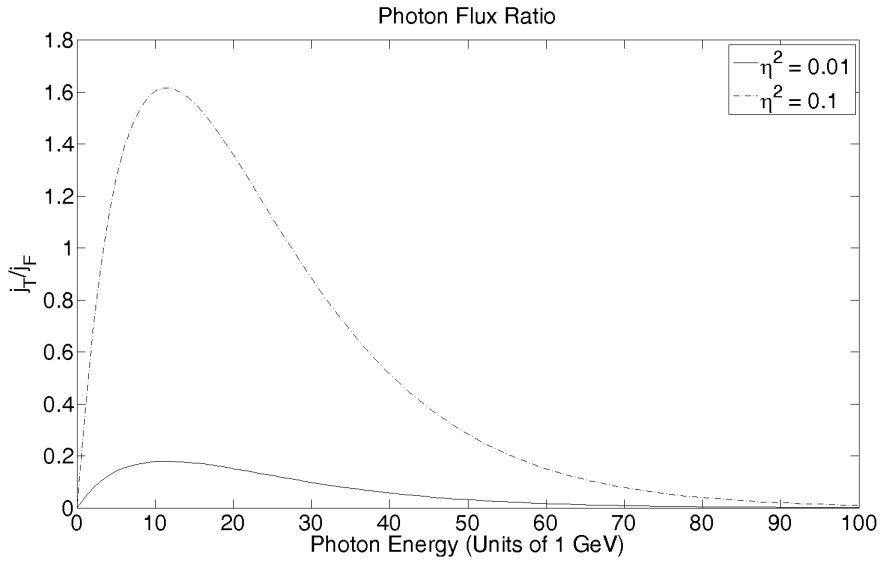

Figure 4.6: Gamma Ray Flux Ratio $j_{T/F}$ ($m_S = 100$ GeV)

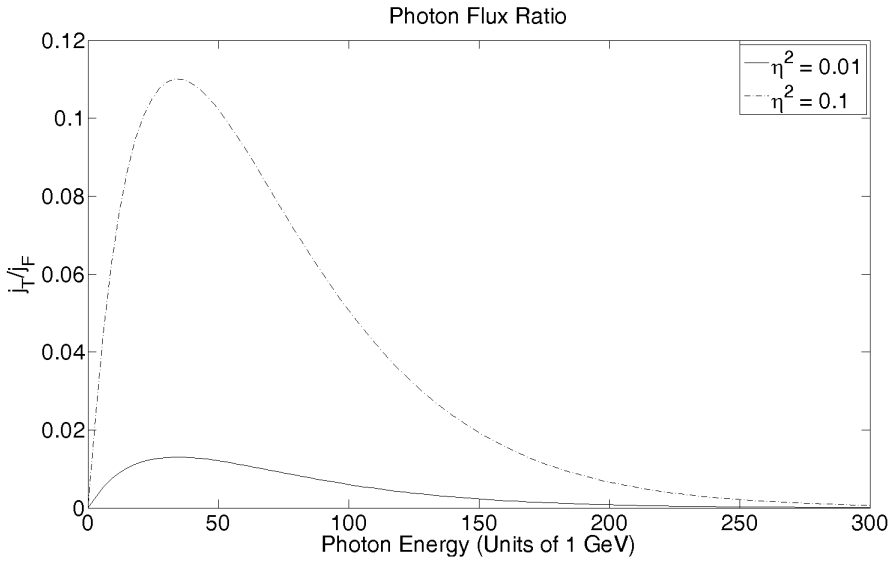

Figure 4.7: Gamma Ray Flux Ratio $j_{T/F}$ ($m_S = 300$ GeV)

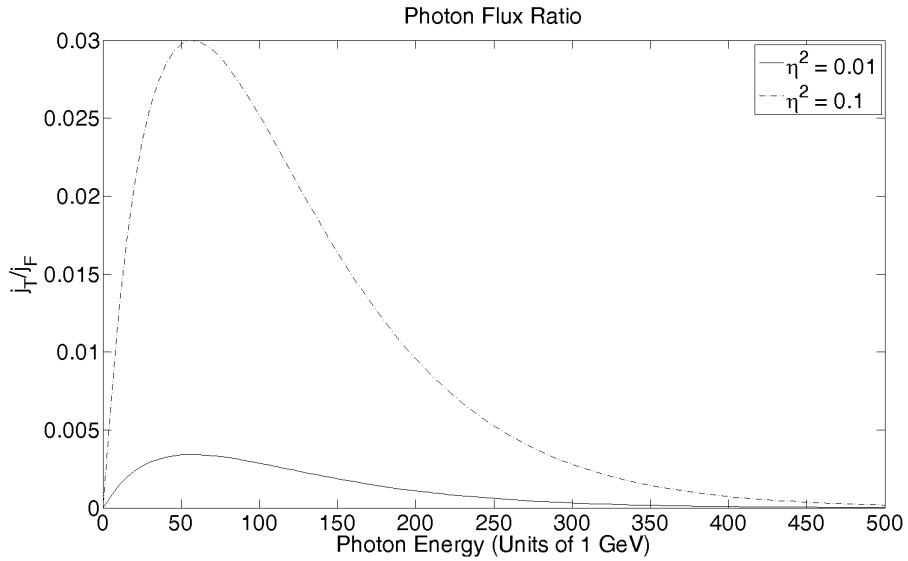

Figure 4.8: Gamma Ray Flux Ratio $j_{T/F}$ ($m_S = 500$ GeV)

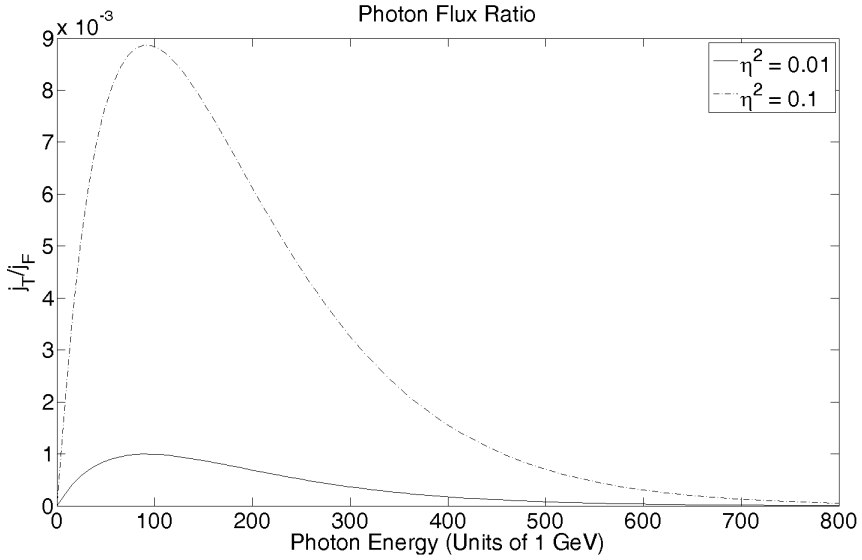

Figure 4.9: Gamma Ray Flux Ratio $j_{T/F}$ ($m_S = 800$ GeV)

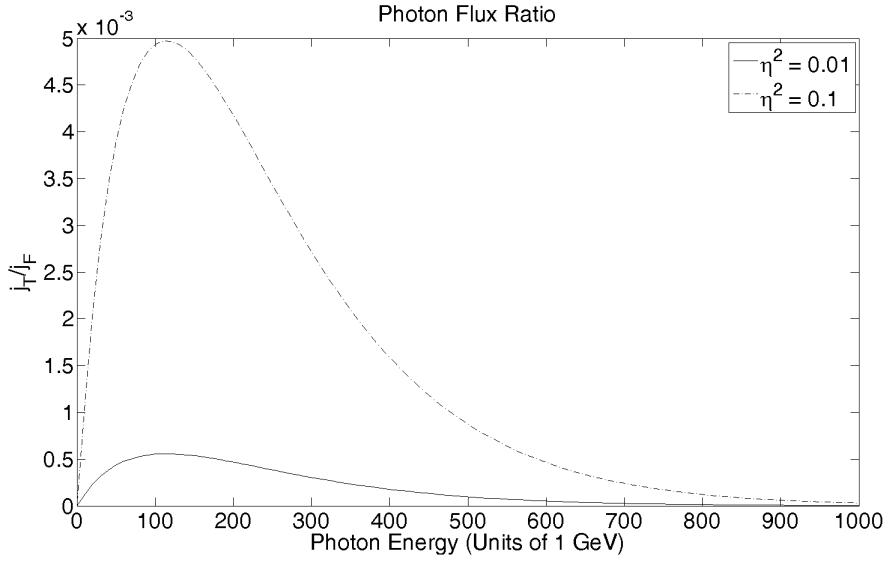

Figure 4.10: Gamma Ray Flux Ratio $j_{T/F}$ ($m_S = 1000$ GeV)

Chapter 5

Antimatter Signals of Singlets

Many of the advances in particle physics over the last several decades have been motivated by the study of cosmic rays. Cosmic rays are particles produced somewhere in space that happen to hit the Earth, often at energies we are incapable of reproducing. It has long been considered that some component of the cosmic ray spectrum might be due to an exotic source, but serious studies of cosmic rays as indirect signatures of dark matter annihilation are fairly recent. In this chapter, we discuss the production and propagation of charged scalar singlet annihilation products and how they might provide a signal.

While theoretically all charged particles produced in these annihilation events could be used as the basis for a search, the realities of the situation require that certain criteria are met. First, dark matter is so sparsely dispersed that there is never enough of it concentrated close to Earth for unstable particles to provide any kind of signal. This rules out any baryon heavier than a proton, and any meson at all, as well as all leptons but the electron flavor. Stable nuclei remain viable. Secondly, any dark matter annihilation signal is expected to be very small, so it would be best to choose those particles that have small backgrounds. This means, in general, that we need to look for antimatter instead of matter. Singlets are rather special, in that they should not favor either matter or antimatter when they annihilate to $\mathcal{SM}$ particles.

The species we consider are positrons (e^+), antiprotons ($\bar{p}$), and antideuterons ($\bar{d}$). Of these, the $\bar{d}$ are produced with far less frequency, but this is made up for by a comparatively low expected background.

5.1 Production

In this section we construct the production spectra that can be inserted into the source term of the propagation equation in the next section. We do this for each species in turn.

In the halo, two singlets annihilate, and their annihilation products are described by equations (2.2 - 2.5). We seek to construct production energy spectra $\frac{d\mathcal{N}_s}{dE}$ for the differential number density of species s with respect to particle energy. This function will of course depend not only on particle energy E, but also on injection energy E_{in}, which is the amount of energy initially available. In our case, we are dealing with nonrelativistic singlets annihilating, so $E_{in} = 2m_S$. The production spectra are not simply the annihilation cross sections. Not only are there no direct annihilations to $\bar{p}$ and $\bar{d}$ as they are composite particles, but even with positrons, the vast majority of positrons produced by singlet annihilation do not come from direct

annihilation. Rather, they are produced by the decay of more abundantly produced particles.

Our analysis is somewhat limited. Many collaborations now use software packages like `PYTHIA` [111] or `DarkSUSY` to make these production spectra calculations, as they take into account most known processes. However, for clarity we provide analytic expressions when possible. We ignore all annihilation products except those which contribute in a significant fashion. For the light singlet mass range of 5-81 GeV, this means the relevant annihilation channels are the b quark channel, the c quark channel, and the τ lepton channel. For the heavy mass range of 81+ GeV, the relevant annihilation channels are the W boson channel, the Z boson channel, the Higgs boson channel, and the t quark channel. The others do not contribute in significant enough quantities.

The number densities can be constructed analytically by using the relation

$$\frac{d\mathcal{N}_s}{dE}(E, E_{in}) = \frac{1}{\sigma_{tot}} \frac{d\sigma_s}{dE} \tag{5.1}$$

for the number density of a particle of species s produced in an annihilation event with cross section σ_s, or the relation

$$\frac{d\mathcal{N}_s}{dE}(E, E_{in}) = \frac{1}{\Gamma_{tot}} \frac{d\Gamma_s}{dE} \tag{5.2}$$

for the number density of a particle of species s produced in a decay with specific decay width Γ_s.

The positron energy spectrum from the annihilation of singlets of mass m_S may be approximated by a step function [79] [105]

$$\frac{d\mathcal{N}_{e^+}}{dE}(E, 2m_S) \simeq \frac{1}{0.7m_S} \Theta(m_S - E).$$

This is an approximation to a polynomial that fails to take into account much of the richer structure resulting from hadronization. Nonetheless, it provides an easily implemented analytic form for the positron spectrum that would otherwise need to be computed using `PYTHIA`. The error introduced by this approximate spectrum is smaller than the error that comes from uncertainties in the propagation model.

Next we consider antihadron spectra, as they are nessecary for both antiprotons and antideuterons, which are made up of an antiproton and an antineutron. While it might be possible to apply some kind of effective theory as was used in Chapter 3 to couple the Higgs boson to nucleons, the approach we have chosen is based on phenomenology and so should model reality better.

There are no direct annihilations to hadrons, but there are direct annihilations to quarks and antiquarks, and to gluons supressed at the loop level. These particles are not color singlets and so confinement dictates that they will hadronize immediately. This hadronization is not a process that can be calculated exactly, as it is not well understood and is nonperturbative, and to make predictions we need to rely on experimentally fitted functions, called fragmentation functions. These fragmentation functions $D_q^h(Q)$ describe the probability of a quark or antiquark q to hadronize into a hadron h that carries a proportion Q of the quark's momentum. Such functions exist for gluons as well.

We use a fitted total fragmentation function for the production of antiprotons from dark matter annihilation [18], which is derived from computations done with PYTHIA using the quark to proton fragmentation functions as measured from collider experiments. The parameterization takes the form for annihilation channel f

$$\frac{d\mathcal{N}_{\bar{p}}^{f}}{dx} = \left(p_1 x^{p_3} + p_2 \left|\log_{10}(x)\right|^{p_4}\right)^{-1} \tag{5.3}$$

where $x = E_{\bar{p}}/m_S$ is the scaled kinetic energy of the antiproton and the p_i are given by

$$p_i(m_S) = \left(a_{i1} m_S^{a_{i2}} + a_{i3} m_S^{a_{i4}}\right)^{-1}$$

and the parameters a_{ij} are found in the reference. The a_{ij} depend on the direct annihilation products that fragment to antiprotons, and included are the c, b, and t quark channels, and the W and Z boson channels. The fragmentation functions for each annihilation channel must be summed with appropriate weightings to give the total antiproton production spectrum from singlet annihilations:

$$\frac{d\mathcal{N}_{\bar{p}}}{dx} = \sum_f BR_f \frac{d\mathcal{N}_{\bar{p}}^{f}}{dx}.$$

This parameterization is valid for the singlet mass range of 50-5000 GeV. We use it for one computation outside of this range, at $m_S = 10$ GeV. While the parameterization may not be fully valid at this mass, we feel that the general structure should hold enough to provide an estimate. The branching ratios are computed with $\eta = 0.1$ for definitness. We do not expect changing η to alter the results in any unexpected fashion.

Now that we have both the $\bar{p}$ and the $\bar{n}$ spectra from singlet annihilation, we are prepared to compute the $\bar{d}$ spectrum. The model for deuteron nucleation that we have chosen to use is the coalesence model [27]. It is fairly basic, but it is useful for our purposes, and has been used in the context of dark matter annihilations before [41]. The probability that a $\bar{p}$-$\bar{n}$ pair will produce a $\bar{d}$ is dependent on the relative momentum of the two particles, and is greatest when the relative momentum is zero. In momentum space, the probability of finding a $\bar{d}$ is the probability of finding an $\bar{n}$ within a sphere of radius p_0 around a $\bar{p}$, where p_0 is the coalesence parameter, taken to be $p_0 = 79$ MeV. This number is taken from hadronic production data [35]. The energy spectrum of antideuterons is then

$$\frac{dN_{\bar{d}}}{dE_{\bar{d}}} = \frac{4}{3} p_0^3 \frac{m_{\bar{d}}}{m_{\bar{p}} m_{\bar{n}}} \frac{1}{\sqrt{E_{\bar{d}}^2 + 2 m_{\bar{d}} E_{\bar{d}}}} \left(\frac{dN_{\bar{n}}}{dE_{\bar{n}}}\right)_{E_{\bar{n}} = E_{\bar{d}}/2} \left(\frac{dN_{\bar{p}}}{dE_{\bar{p}}}\right)_{E_{\bar{p}} = E_{\bar{d}}/2}.$$

We take the antiproton spectrum (5.3) as applying for both antiprotons and antineutrons. This follows from examination of the fragmentation functions for the neutron and the proton. The heavy quark fragmentation functions are equal for both nucleons, and the u and d quark functions are simply switched when one changes the proton to a neutron. Since the processes we consider produce u and d quarks with essentially equal frequency, it makes sense to retain the isospin symmetry.

With the production spectra for all three species in hand, we can consider the propagation of these particles through the galaxy.

5.2 Propagation

Finding the paths of charged particles as they propagate through the galaxy is a difficult problem. One needs to take into account interactions with the galactic magnetic field, with the interstellar medium and effects like fermi reacceleration and galactic convection. In general, one ends up with a complicated partial differential equation. What we discuss in this section is mostly borrowed from standard cosmic ray propagation theory.

The simplest model that provides somewhat accurate results is the Leaky Box model. This model is what was used until the 1990s, when more data and better computational power made diffusive alternatives more attractive. The Leaky Box model is a basic model of charged particle propagation that averages all quantities over the spatial propagation volume. There is a term in the resulting equation that describes loss of particles due escape from the region, hence the name of the model. While the Leaky Box model has been supersceded by the diffusion model and is now rarely used, it has reproduced the observations of stable nuclei, and can be shown to be equivalent to the diffusion model for stable species in many cases.

We instead choose to use the 2-zone diffusion model [92]. The diffusion model describes the galaxy as a thin disk of gas and stars embedded within a much thicker disk that represents the dark galactic halo. Both disks have the same radius, usually taken to be 20 kpc, and the thin disk has a height of 100 pc. The halo disk is far more of an approximation since the halo is supposed to be spherical, and the choice of the half-height L of this disk greatly affects how the propagation proceeds. Common choices range from $L = 1$ kpc to $L = 15$ kpc. The thin disk density is taken to be 1 cm^{-3} and the halo $\mathcal{SM}$ density is assumed to be low enough that no interactions with propagating charged particles occur. Annihilation and scattering effects on propagating particles only occur within the thin disk, which is usually taken as infinitely thin. The geometry of the problem naturally suggests use of the cylindrical coordinate system (r, θ, z). In this coordinate system, we place the solar system in the galactic disk at $(r_\odot, \theta, 0)$, where $r_\odot = 8.5$ kpc and θ is made irrelevant by the symmetry of the problem.

The 2-zone model is not without its weaknesses. We mention the three main issues that certainly make the model no more than a crude approximation. The first is that the 2-zone model assumes the diffusion region is cylindrical, in the hopes of obtaining an exact analytical solution to the transport equation. We have no reason to believe the actual shape of the diffusion region is anything but spherical or perhaps deformed spherical. The model also assumes a sharp boundary condition which is blatantly unphysical. Observations suggest the fall-off of the galactic magnetic field is more like an exponential decay than a sudden absence. Finally, the model only takes into account particle sources inside the diffusion region. Since the main source of antimatter we are considering is from the annihilation of halo dark matter, the fact that the diffusion region only covers a small part of the halo means that much of the relevant source region is not included. This in particular makes the 2-zone model less attractive for use in indirect dark matter searches. Though some of these issues are fixed in the modified 3-zone diffusion model [102], we choose to work in the 2-zone model for simplicity.

The 2-zone model gives a basic diffusion-convection transport equation for charged particles in a cylindrically symmetric galaxy. The solution of the equation $\psi(\mathbf{x}, E, t)$ is the differential number density of a species of charged cosmic ray. One would solve this equation and then multiply by $\beta/4\pi$ to obtain the local flux. The equation is

$$\nabla \cdot \left[K(\mathbf{x}, E)\nabla\psi(\mathbf{x}, E, t) - \bar{V}_c(\mathbf{x}, E)\psi(\mathbf{x}, E, t)\right] - \Gamma_{ann}(E)\psi(\mathbf{x}, E, t) + \mathcal{Q}(\mathbf{x}, E, t)$$

$$+\frac{\nabla \cdot \bar{V}_c(\mathbf{x}, E)}{3}\frac{\partial}{\partial E}\left[\frac{p^2}{E}\psi(\mathbf{x}, E, t)\right] - \frac{\partial}{\partial E}\left[b_{ion}(E) + b_{Col}(E)\psi(\mathbf{x}, E, t)\right]$$

$$-\frac{\partial}{\partial E}\left[\frac{1+\beta^2}{E}K_{pp}(E)\psi(\mathbf{x}, E, t)\right] + \frac{\partial}{\partial E}\left[\beta^2 K_{pp}(E)\psi(\mathbf{x}, E, t)\right] = \frac{\partial}{\partial t}\psi(\mathbf{x}, E, t).$$

This equation is complicated, but fourtunately the species and energy ranges we are dealing with often allow simplifications to be made. One simplification we can make, that applies to all three species, is that we seek steady-state solutions. This means that the time derivative on the right hand side is set to zero, and the solution has no time dependance. This assumption is based on the idea that the amount of dark matter in the galaxy is not changing and has not been changing for some time. This is a property of cold dark matter models. We are also, as mentioned above, working in a cylindrically symmetric galaxy, so $\mathbf{x} = (r, z)$.

The first term in the equation is the diffusion-convection term. The part of this term containing the galactic wind $\bar{V}_c(\mathbf{x}, E)$ is the convection term, while the part containing the diffusion coefficent $K(\mathbf{x}, E)$ is the spatial diffusion term. The second term with $\Gamma_{ann}(E)$ describes losses due to annihilation in the interstellar medium, and $\mathcal{Q}(\mathbf{x}, E, t)$ is the source term, which can be obtained from the production spectrum. The first term on the second line involves adiabatic energy losses due to the galactic wind, and the second term on the second line covers losses due to ionization and Coulomb interactions. The final two terms in the equation describe first and second order Fermi reacceleration in the magnetic fields of the galaxy.

Some additional assumptions include neglecting the reacceleration terms for all species, and neglecting the convection terms for positrons, simply because the effect these terms have is minimal. The diffusion term represents the interaction of charged particles with inhomogeneities in the galactic magnetic field. The diffusion coefficent must be related to these inhomogeneities, but their structure is poorly understood. The usual assumption for $K(\mathbf{x}, E)$ is that of spatial independence,

$$K(\mathbf{x}, E) = K_0\left(\frac{E}{GeV}\right)^{\delta}$$

for positrons or

$$K(\mathbf{x}, E) = K_0\beta\left(\frac{p}{GeV}\right)^{\delta}$$

for the antinuclei, where E, p, and β are the energy, momentum and velocity of the particle, respectively. The constants K_0 and δ are parameters of the model, constrained by observation as discussed below. Additionally, the convective wind is assumed to be of constant magnitude everywhere, directed outward from the galactic disk.

We neglect annihilations for positrons and take annihilations as occuring only in the galactic disk for antiprotons with an annihilation rate in terms of the number densities of hydrogen and helium in the interstellar medium

$$\Gamma_{ann} = \left(n_H + 4^{2/3} n_{He}\right) \sigma_{p\bar{p}}^{ann} v_{\bar{p}}.$$

This expression becomes somewhat more complicated for antideuterons, since they are a composite particle. More details can be found in the reference [92].

We also take our source to be only the primary source. There are also secondary particle fluxes from particles produced during propagation, but we neglect those.

We also neglect potential effects from what is called solar modulation. The solar wind changes the behavior of local charged particles to a degree, making the particle flux outside the solar system somewhat different from the particle flux detected at the Earth. These effects are mainly relevant for nonrelativistic particles, so not including them has only a minor effect.

There are several free parameters in this model that must be constrained somehow. The usual method of constraining these parameters is by examining the Boron to Carbon ratio in the cosmic ray flux we observe [50]. Both of these nuclei are stable and common enough to obtain a decent sample size. From these nuclear ratios, several sets for the free parameters have been created.

The sets that have become the standard in the dark matter indirect search community are the parameter sets that maximize or minimize the local antiproton flux, as well as one that is midway between the two. They are known as MAX, MED and MIN, and they are used for many particle species, not just antiprotons. We have presented in Figures 5.1 - 5.21 our results using all of these models.

This transport equation can be solved for the number density of a charged particle species in a number of ways. The most complete solution is purely numerical, either through the public software package `GALPROP` [120] or through some other package. These solutions are capable of taking into account factors that would be highly impractical to include in an analytic solution, and hence present a higher degree of accuracy. Of course, our understanding of cosmic ray propagation is incomplete, and these numerical solutions remain constrained by our models.

The second method that exists is solving the equation, with appropriate simplifying assumptions, through a series expansion. The cylindrical symmetry of the problem naturally suggests a Fourier-Bessel decomposition of the solution. The basic form of the solution is taken to be

$$\psi(r, z, E) = \sum_{n=1}^{\infty} \sum_{i=1}^{\infty} P_{i,n}(E) \sin\left[\frac{n\pi}{2L}(z + L)\right] J_0\left(\frac{\alpha_i r}{R_{gal}}\right)$$

where the $P_{i,n}(E)$ are the expansion coefficents and J_0 is the Bessel function of 0th order, with α_i its zeros. We then apply the boundary conditions to find the full form of the solution. This method has been successfully applied in the past [50] [92]. A major uncertainty with these solutions lies in the boundary conditions. Retaining the validity of the expansions requires making certain assumptions about the nature

of the propagation region in the galaxy. The validity of these assumptions remains in question, as was noted before. The numerical evaluation of these series solutions also presents difficulties. The convergence of the series is, in general, rather slow, so to obtain any degree of accuracy requires significant computational expense. The coefficient functions of the series solution also contain potentially singular integrals over the halo density profile. If these integrations are not treated carefully, the series can easily fail to converge, but the balance between accuracy and numerical solvability is not easy to find. All in all, series solutions to the transport equation are not suited to computations. They are best used as a demonstration of the existence of an analytic solution to the equation, or as a tool to explore its behavior, rather than as a means of comparing theory to experiment.

The final way of solving the transport equation relies on Green's functions. It is certainly the simplest method for the case of positron propagation, but the more complex propagation of nuclei makes it nearly as difficult to use as the series method. Obtaining the Green's functions usually requires use of series methods in any case.

Since there is a great deal of literature on the subject of dark matter indirect detection by antimatter signals, it should not be surprising that numerical and analytic propagation functions are available for all three of the species dealt with here. We use the functions provided by Cirelli and collaborators [31], since they present simple analytic expressions.

For the case of positrons, the local flux can be written as

$$\frac{d\phi_{e^+}}{dE} = \frac{1}{4\pi}\frac{v\tau_\odot}{\epsilon^2}\frac{1}{2}\left(\frac{\rho_\odot}{m_S}\right)^2 \sum_f \langle\sigma v\rangle_f \int_\epsilon^{m_S} d\epsilon_s \frac{d\mathcal{N}^f_{e^+}}{dE}(\epsilon_s) I(\epsilon,\epsilon_s)$$

where $\tau_\odot$ is the propagation timescale $\rho_\odot$ is the local dark matter density, and the function $I(\epsilon,\epsilon_s)$ can be parameterized as

$$I(\epsilon,\epsilon_s) = a_0 + a_1 \tanh\left(\frac{b_1 - l}{c_1}\right)\left[a_2 \exp\left(-\frac{(l-b_2)^2}{c_2}\right) + a_3\right].$$

The variable $l = \log_{10}(\lambda/kpc)$, where

$$\lambda = \frac{\sqrt{4K_0\tau_\odot\left(\epsilon^{\delta-1} - \epsilon_s^{\delta-1}\right)}}{1-\delta}.$$

The antinuclei fluxes can be written as

$$\frac{d\phi_{\bar{N}}}{dE} = \frac{v_{\bar{N}}}{4\pi}\frac{1}{2}\left(\frac{\rho_\odot}{m_S}\right)^2 \sum_f \langle\sigma v\rangle_f \frac{d\mathcal{N}^f_{\bar{N}}}{dE} R(E)$$

where the function $R(E)$ can be expressed in the form

$$\log_{10}(R(E)/Myr) = a_0 + a_1 k + a_2 k^2 + a_3 k^3 + a_4 k^4 + a_5 k^5$$

and $k = \log_{10}(E/GeV)$.

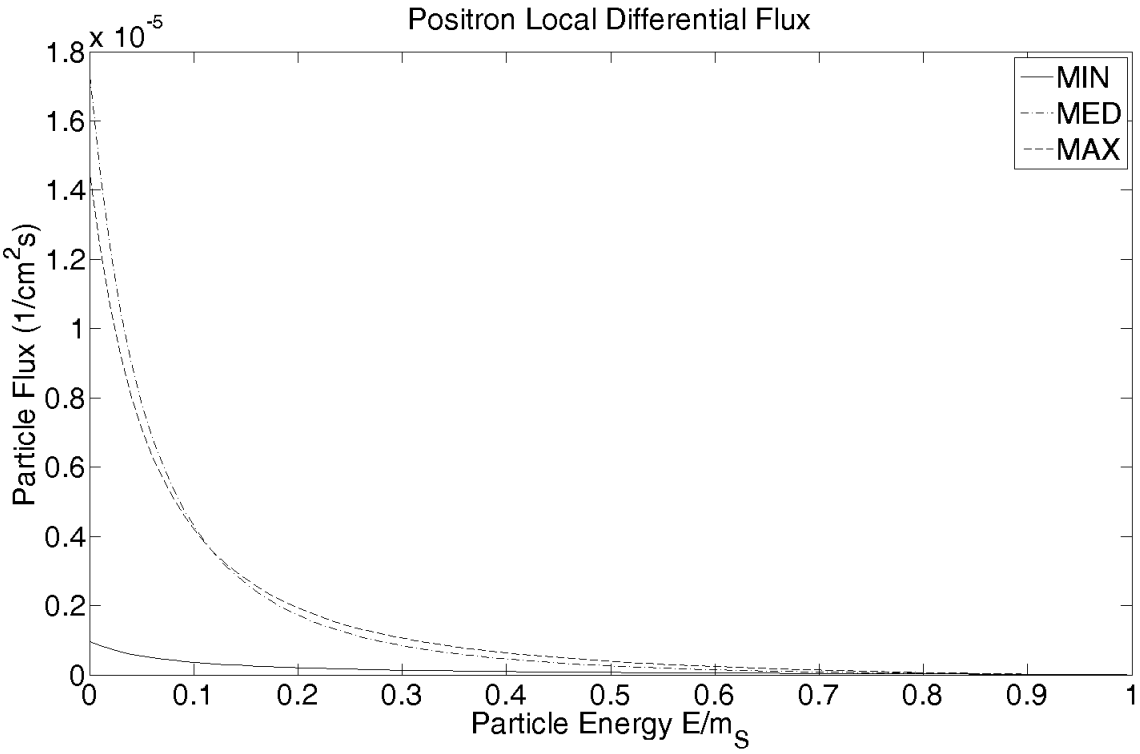

Figure 5.1: Local Positron Flux ($m_S = 10$ GeV)

The parameters for all of these functions are available in the reference and online. With these functions, we can use the production spectra and the annihilation cross sections from Chapter 2 to compute the local flux for all three particle species.

In Figures 5.1 - 5.7 are the local positron flux for a selection of singlet masses (m_S = 10, 50, 100, 300, 500, 700, 1000 GeV). We note first that the energy scales are different in each figure. To better highlight the structure of the flux at low energies, we have truncated the higher energy values. The next set of Figures (5.8 - 5.14) contains the local antiproton fluxes, again plotted for the same set of singlet masses as the positron fluxes. Finally, we present the local antideuteron fluxes in Figures 5.15 - 5.21. The set of singlet masses is again the same.

The antinuclei fluxes are of a similar shape to the positron fluxes. We note that the antideuteron flux is at the per cent level when compared to the antiproton flux at the same singlet mass, which is to be expected.

Given the behavior of the fluxes, we would expect an observable signal to appear for low mass singlets in the low energy range first. In fact, it is unlikely that the computed fluxes for the higher mass singlets will ever rise above the background. Given the prevalence of positrons in the background over antinuclei, perhaps the best chance of detecting a positive signal lies in the low energy antinucleus peak that occurs at around 5 per cent of the singlet mass.

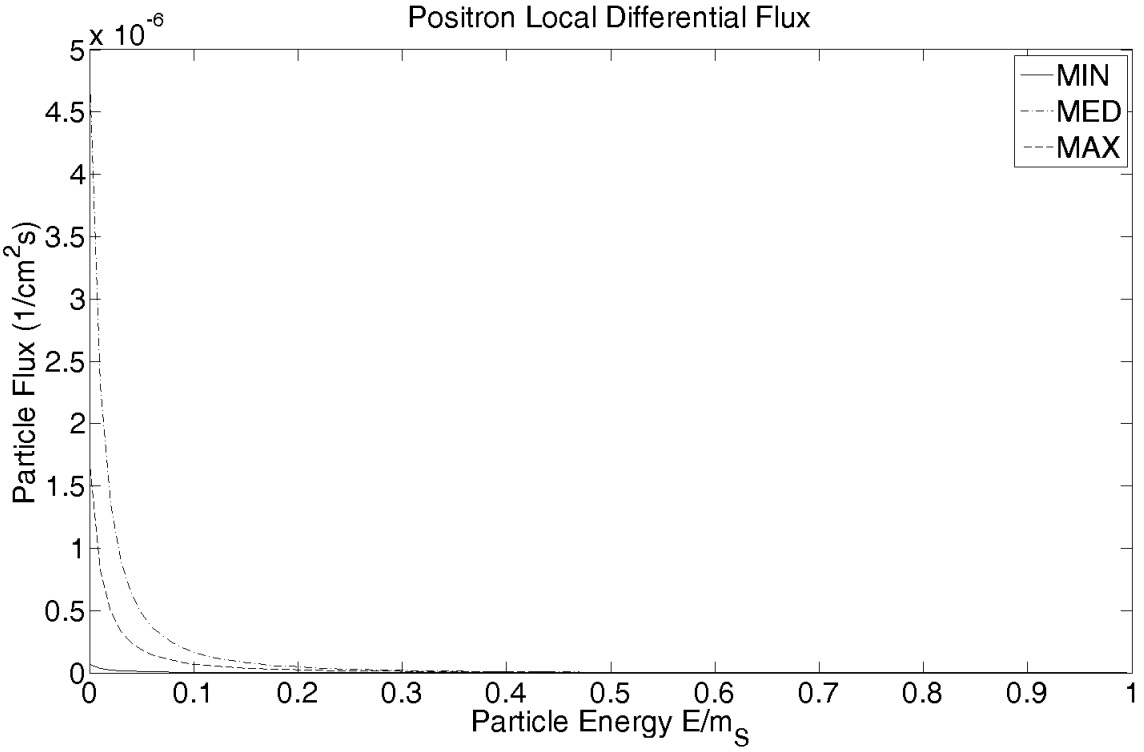

Figure 5.2: Local Positron Flux ($m_S = 50$ GeV)

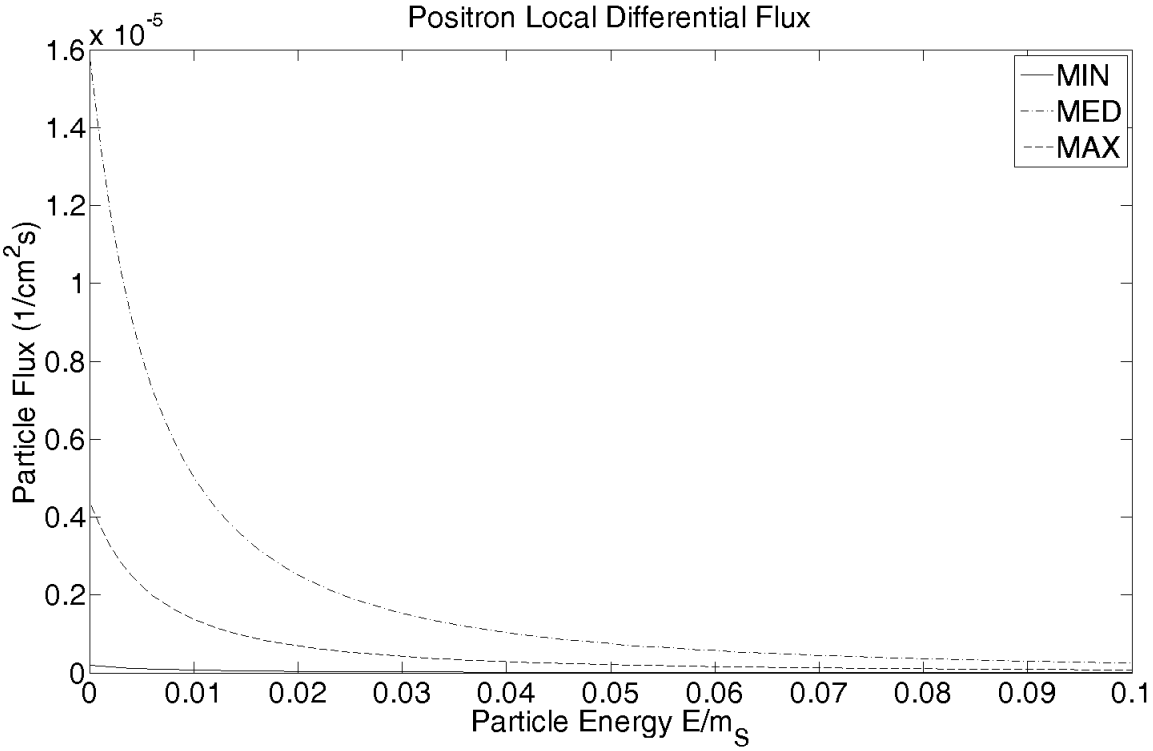

Figure 5.3: Local Positron Flux ($m_S = 100$ GeV)

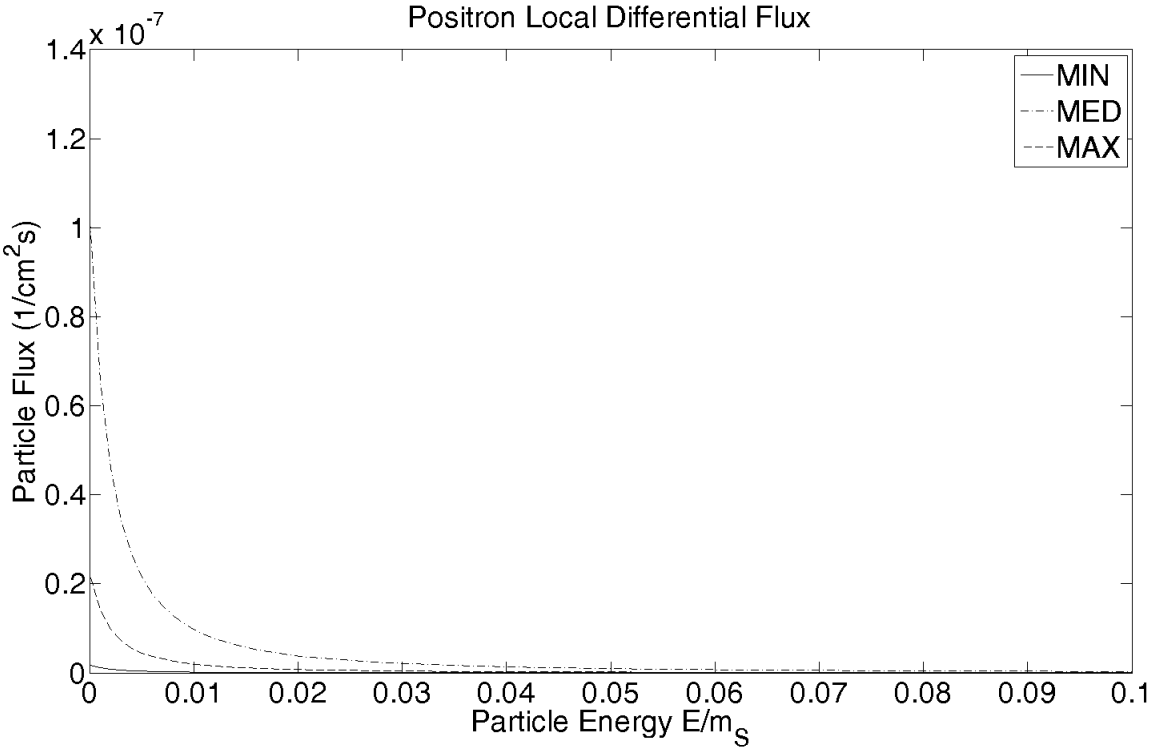

Figure 5.4: Local Positron Flux ($m_S = 300$ GeV)

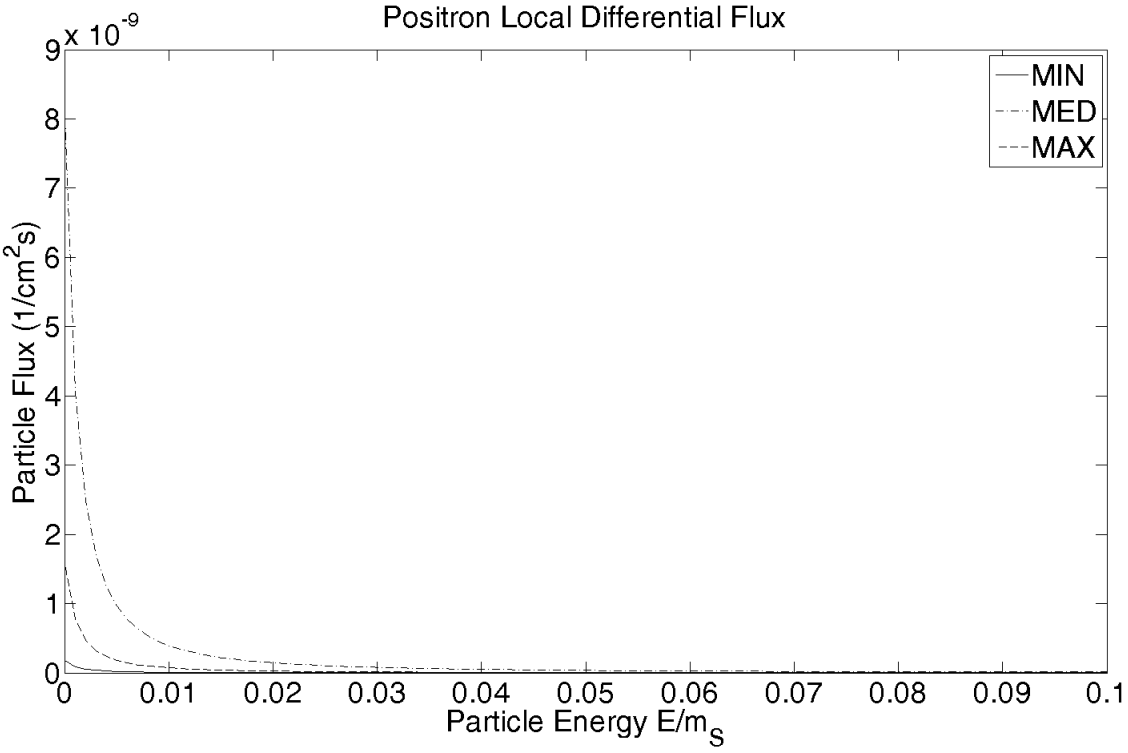

Figure 5.5: Local Positron Flux ($m_S = 500$ GeV)

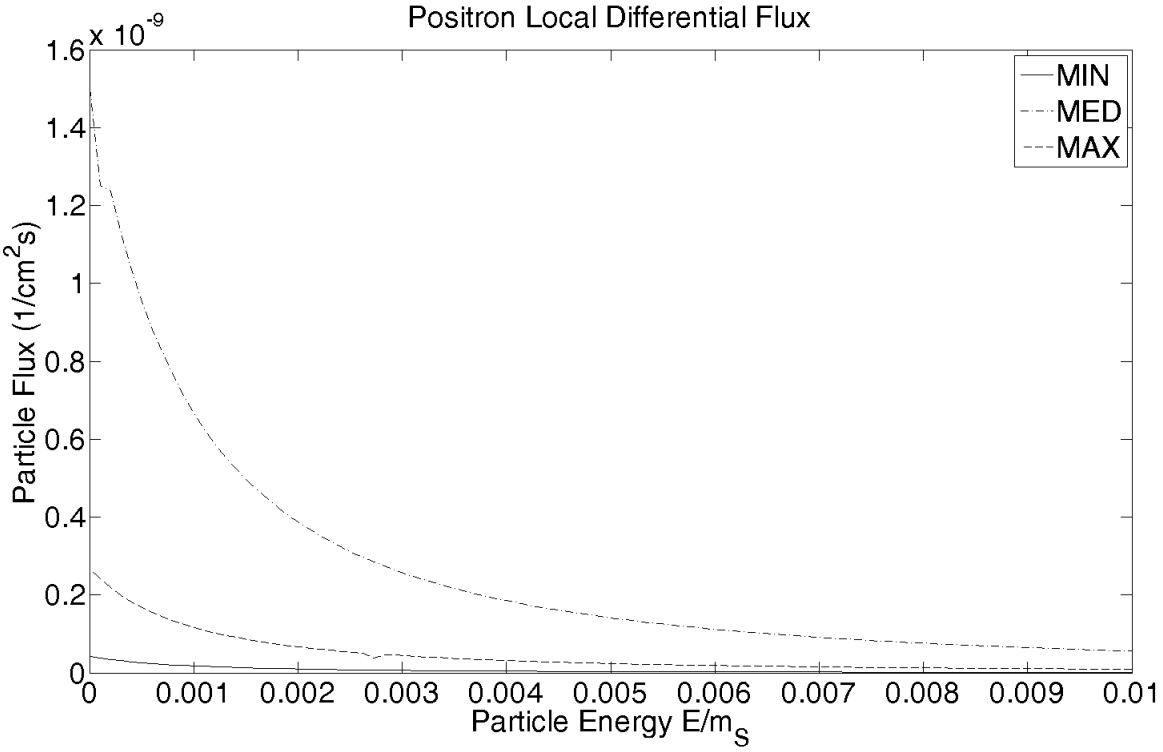

Figure 5.6: Local Positron Flux ($m_S = 700$ GeV)

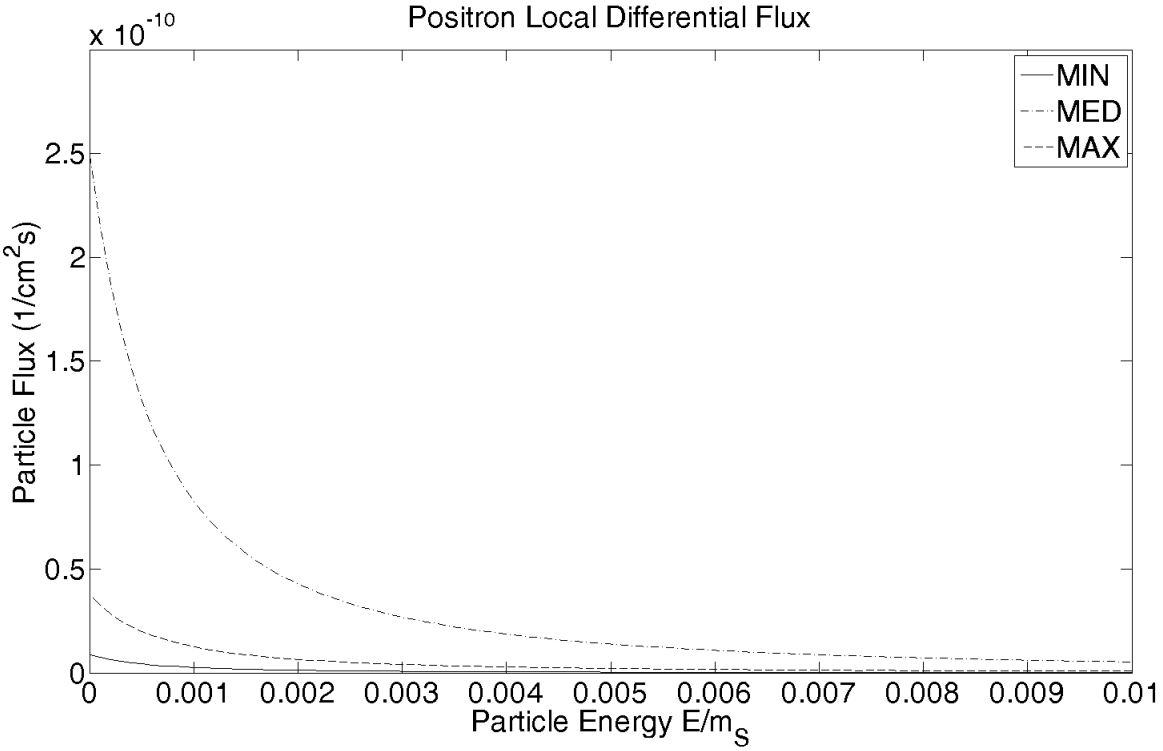

Figure 5.7: Local Positron Flux ($m_S = 1000$ GeV)

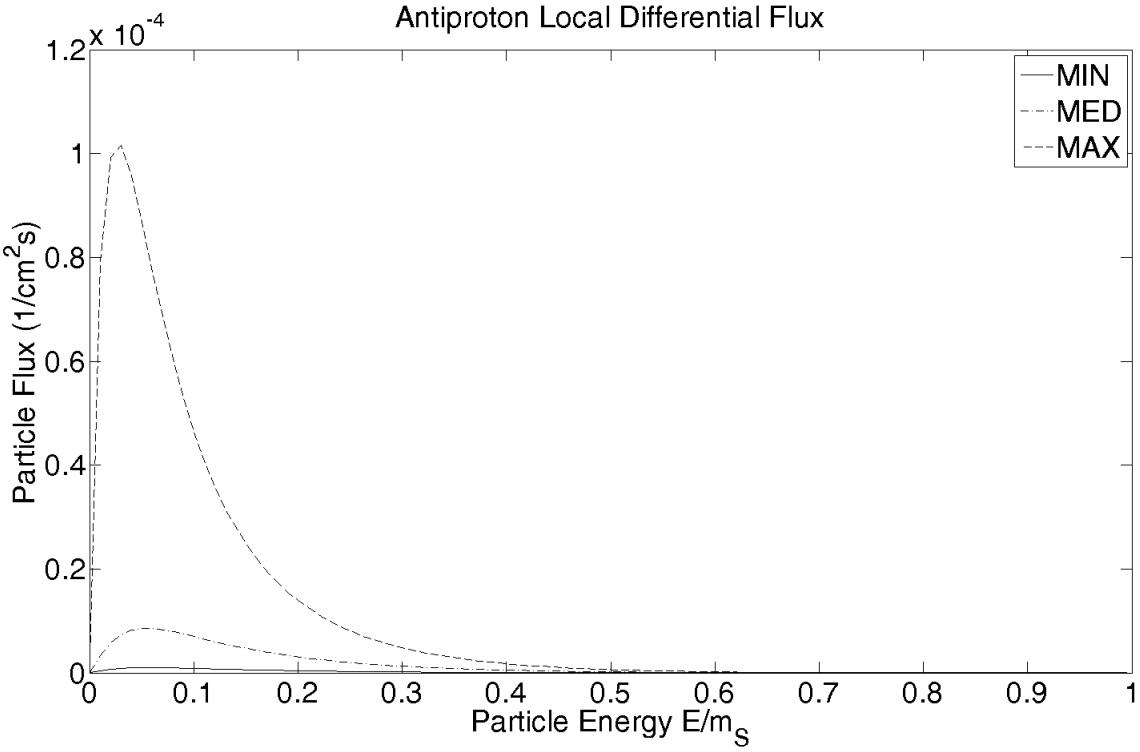

Figure 5.8: Local Antiproton Flux ($m_S = 10$ GeV)

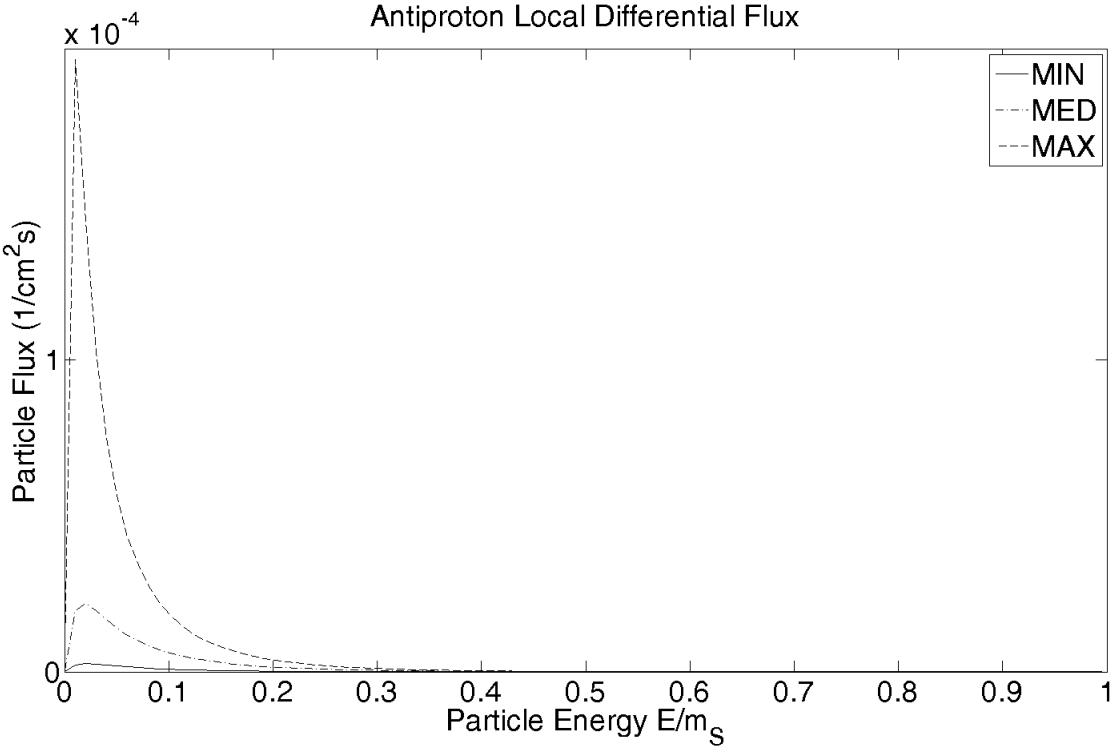

Figure 5.9: Local Antiproton Flux ($m_S = 50$ GeV)

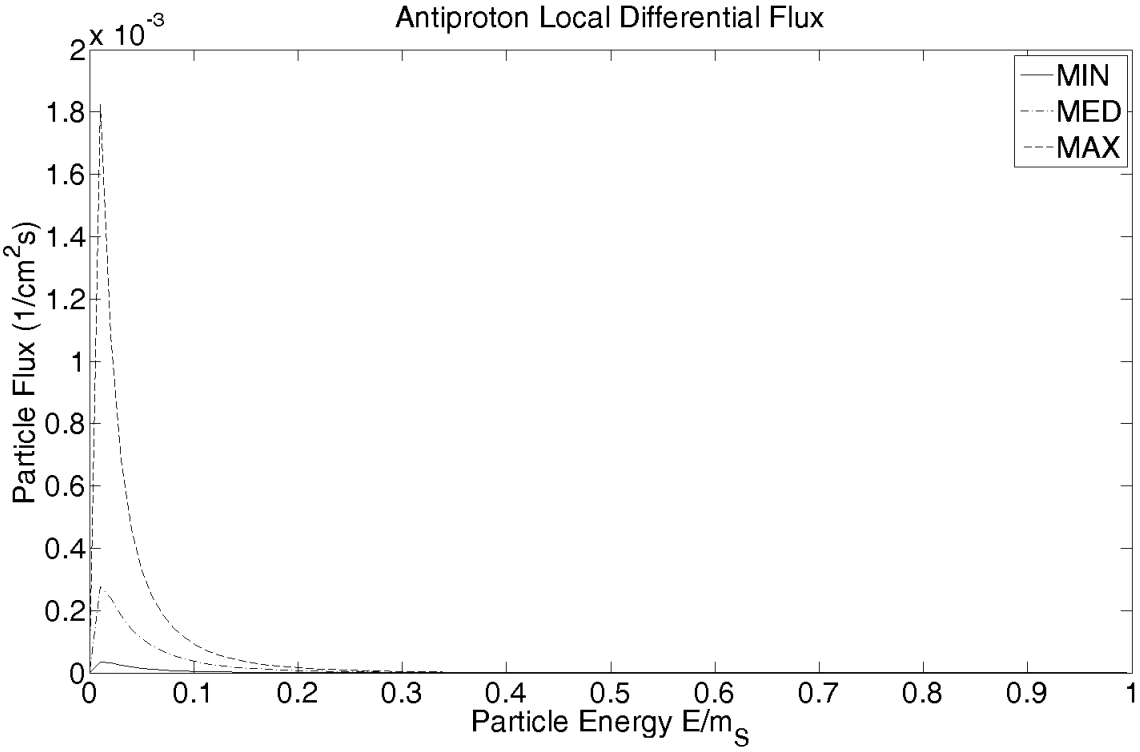

Figure 5.10: Local Antiproton Flux ($m_S = 100$ GeV)

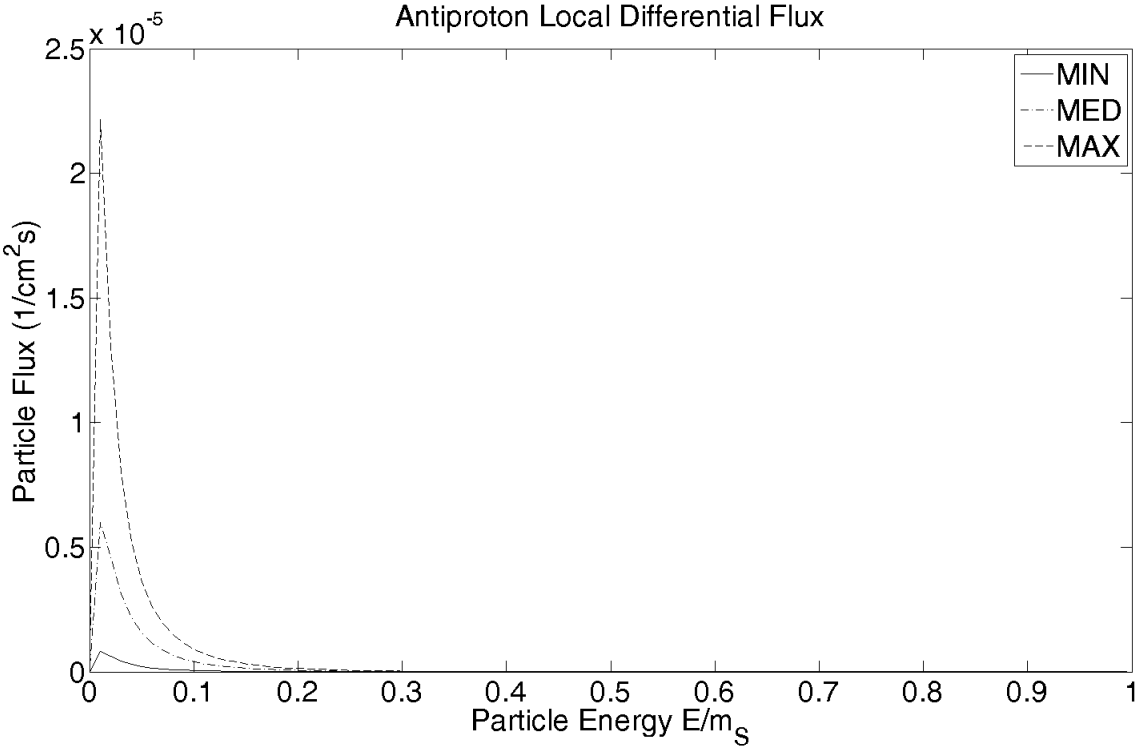

Figure 5.11: Local Antiproton Flux ($m_S = 300$ GeV)

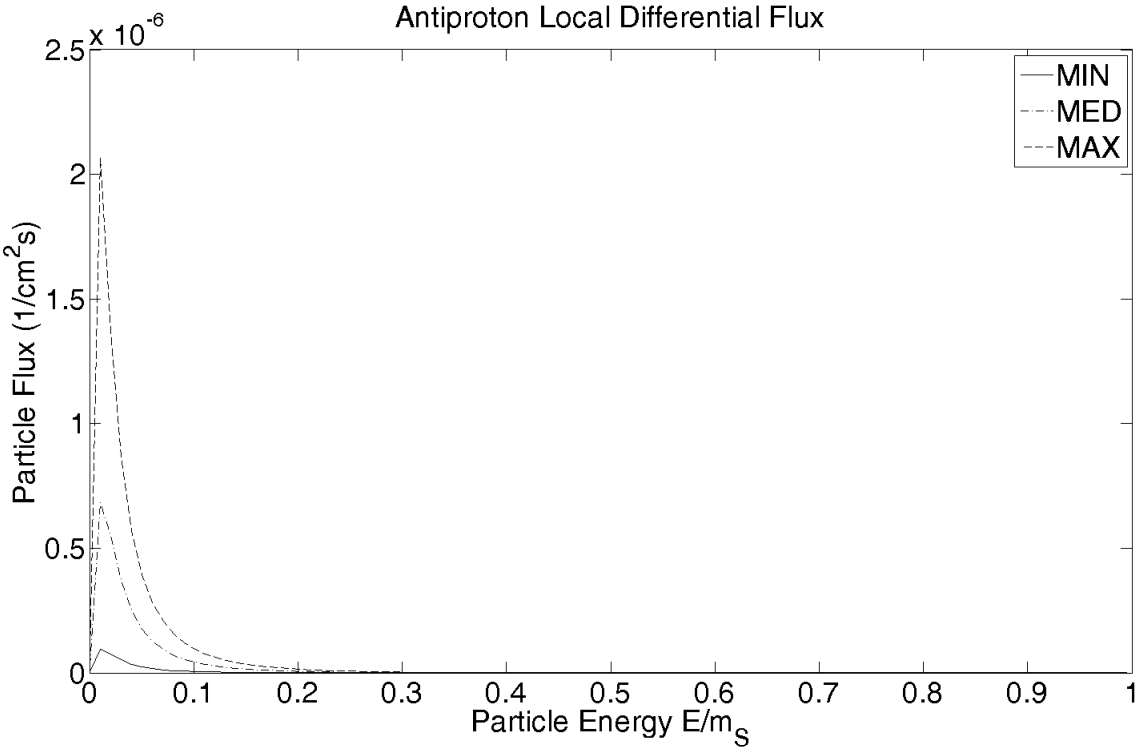

Figure 5.12: Local Antiproton Flux ($m_S = 500$ GeV)

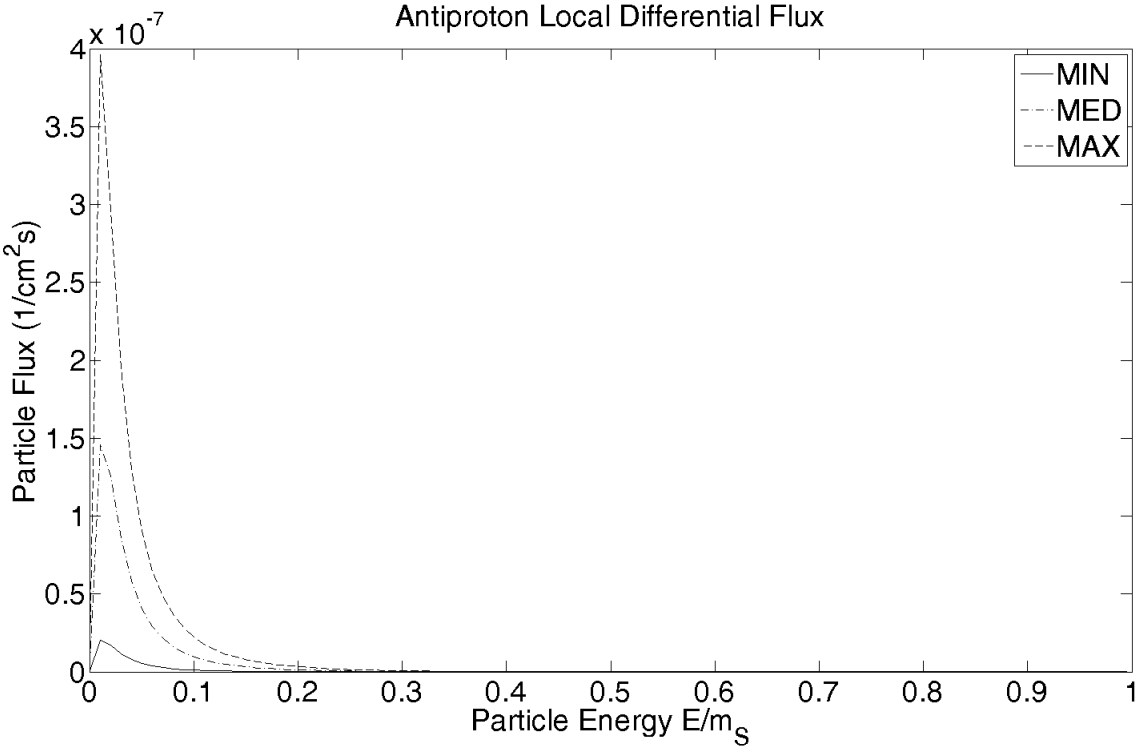

Figure 5.13: Local Antiproton Flux ($m_S = 700$ GeV)

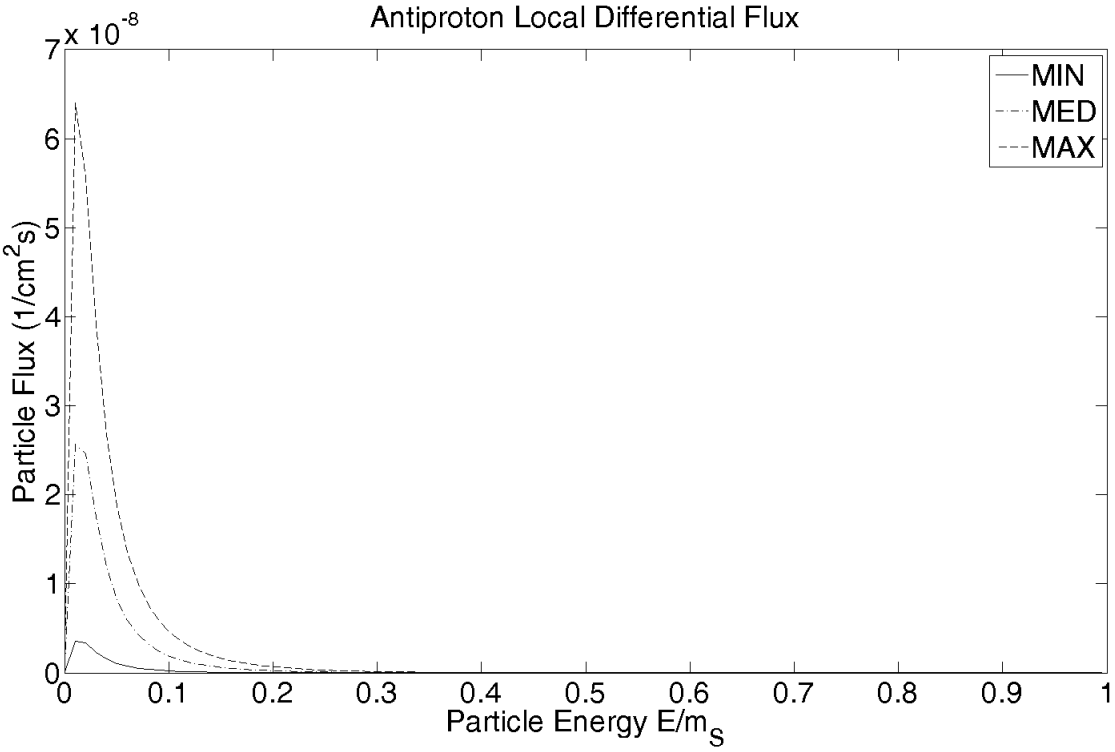

Figure 5.14: Local Antiproton Flux ($m_S = 1000$ GeV)

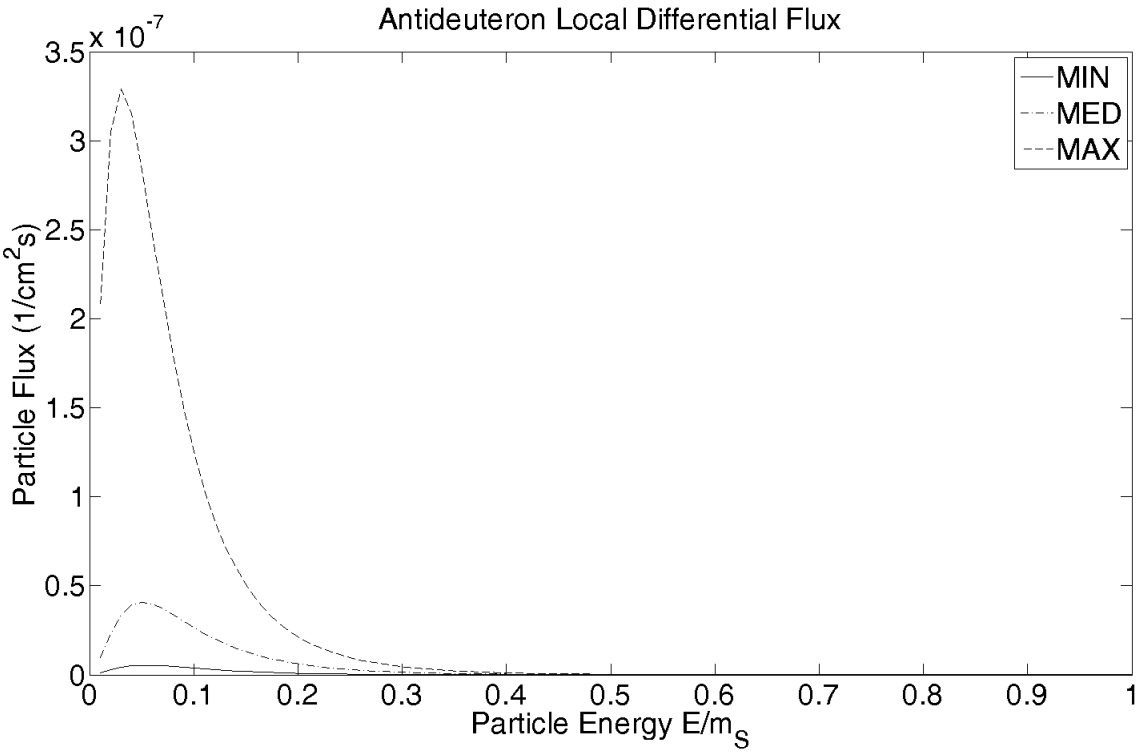

Figure 5.15: Local Antideuteron Flux ($m_S = 10$ GeV)

5.3 Discussion

We compare the presented antimatter fluxes with the observations of two space based experiments, PAMELA [34] and AMS-II [13]. Both are magnetic spectrometer devices that can detect the charge, mass, and velocity of incoming particles. The AMS-II has only recently begun to take data, and the full results of the collaboration will not be available for some time. We consider the available PAMELA antiproton flux data only, as the collaboration has not made public their positron data and has no recorded antideuteron data. The PAMELA antiproton data is available in the literature [3].

The antiproton local spectra are at the per cent level or less compared to the PAMELA data. While no conclusions can be drawn from the PAMELA data, the similar scales of the computed and observed spectra lead to an optimistic outlook for comparisons with AMS-II data. The antiproton signals may be capable of excluding some of the singlet parameter space with more data.

PAMELA is an antimatter optimized cosmic ray detector on a satellite that orbits between 350 and 610 km above the surface of the Earth. The core of the detector is the magnetic spectrometer, which is composed of a series of silicon detector plates inside the cavity of a permanent magnet. By considering deflection in the magnetic field and ionization losses on the silicon plates, momentum and charge of the particle can be found. The energy of the particle is measured by a calorimeter, which can distinguish between through-going particles, electromagnetic showers, and hadronic showers, providing further information about the particle.

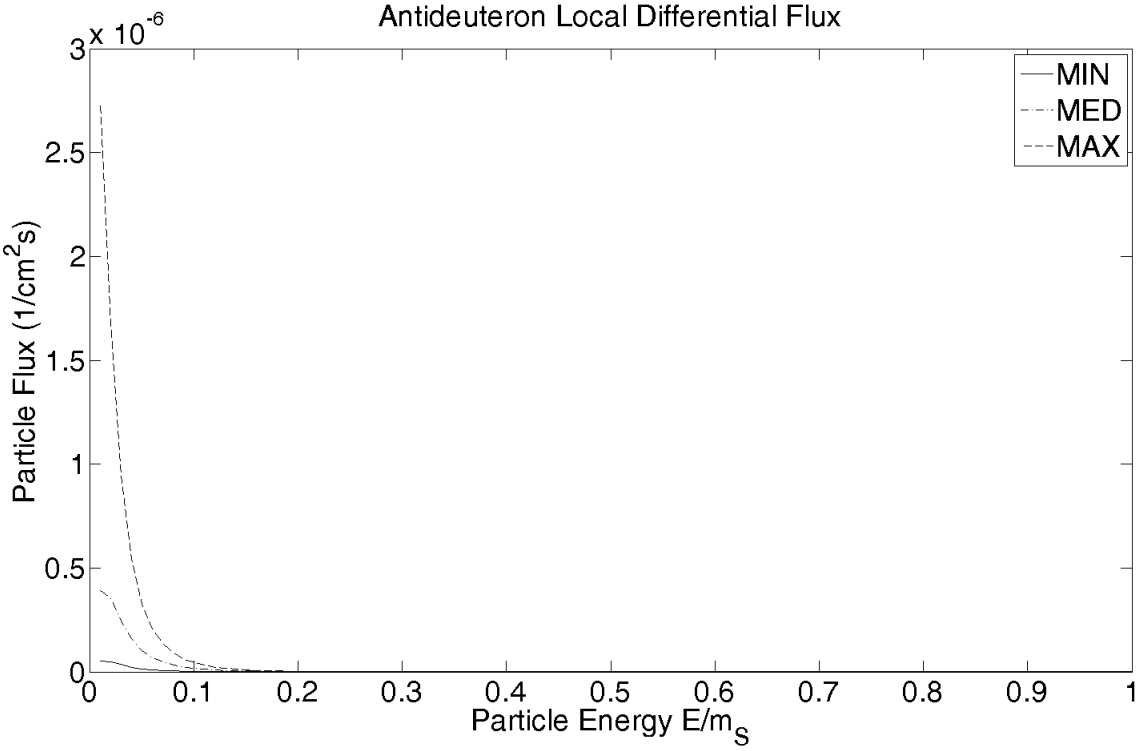

Figure 5.16: Local Antideuteron Flux ($m_S = 50$ GeV)

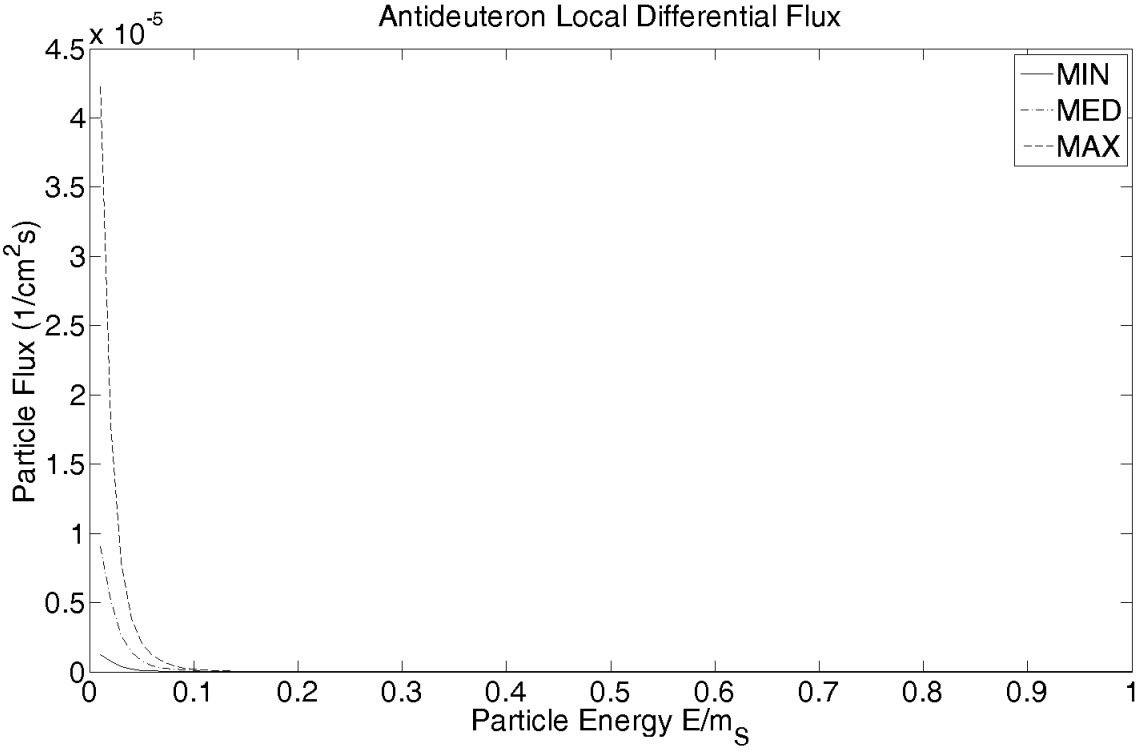

Figure 5.17: Local Antideuteron Flux ($m_S = 100$ GeV)

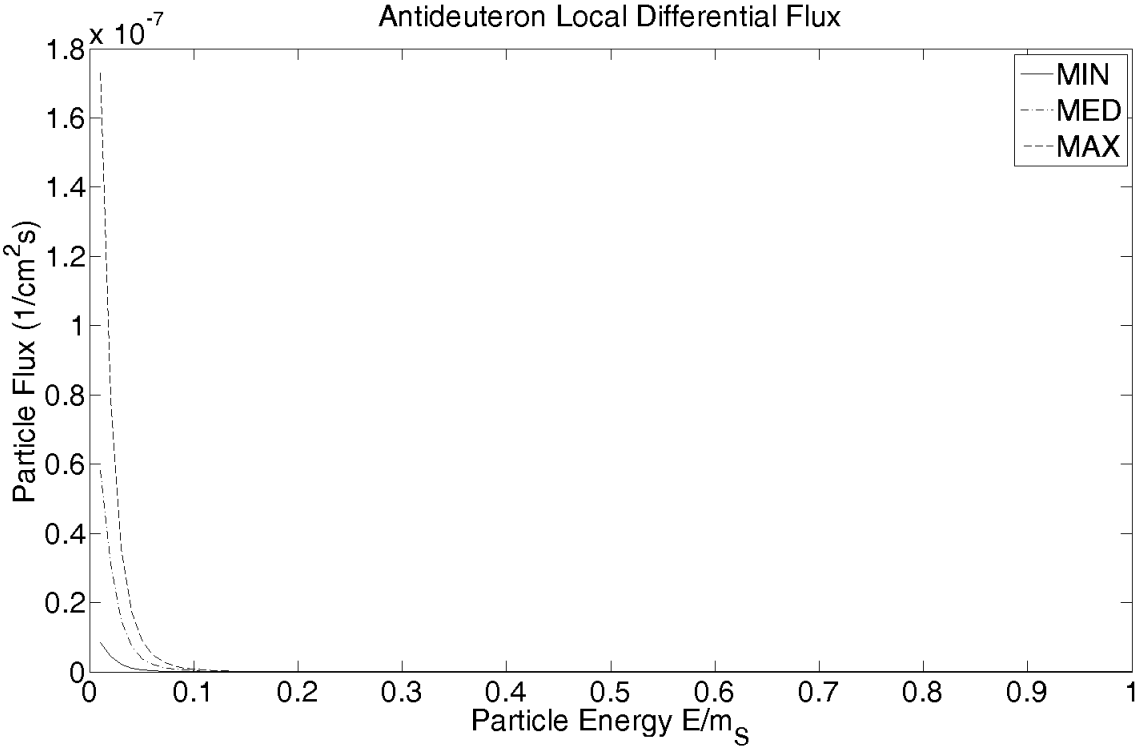

Figure 5.18: Local Antideuteron Flux ($m_S = 300$ GeV)

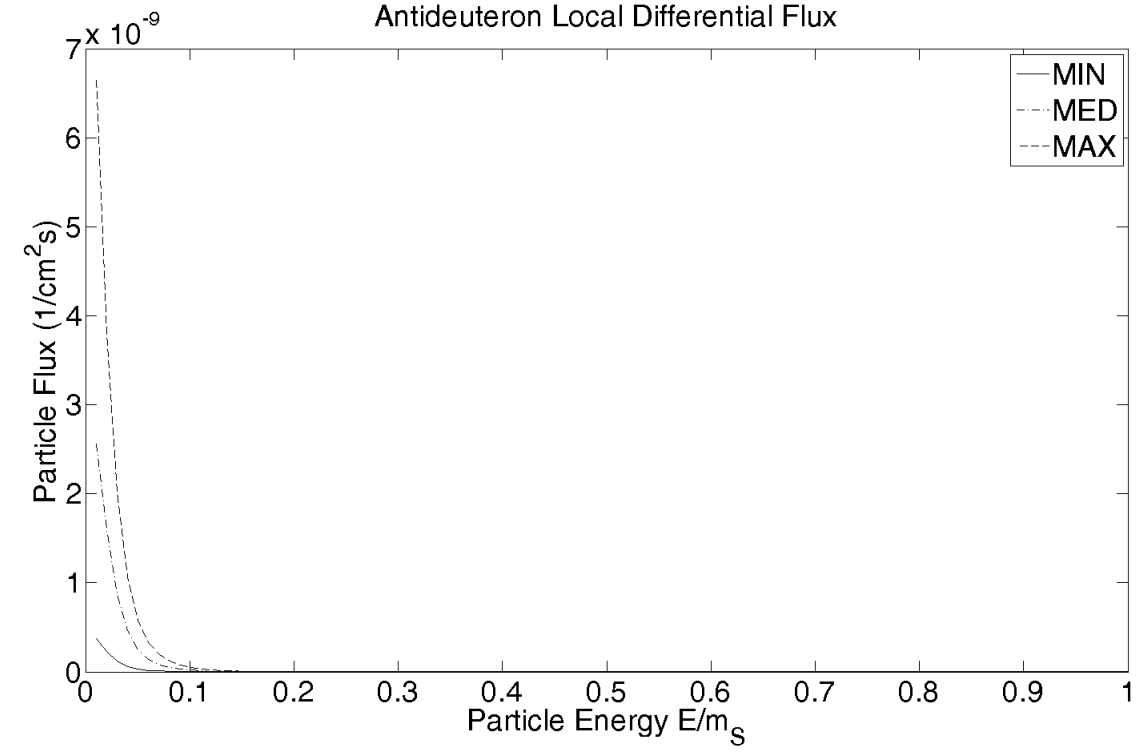

Figure 5.19: Local Antideuteron Flux ($m_S = 500$ GeV)

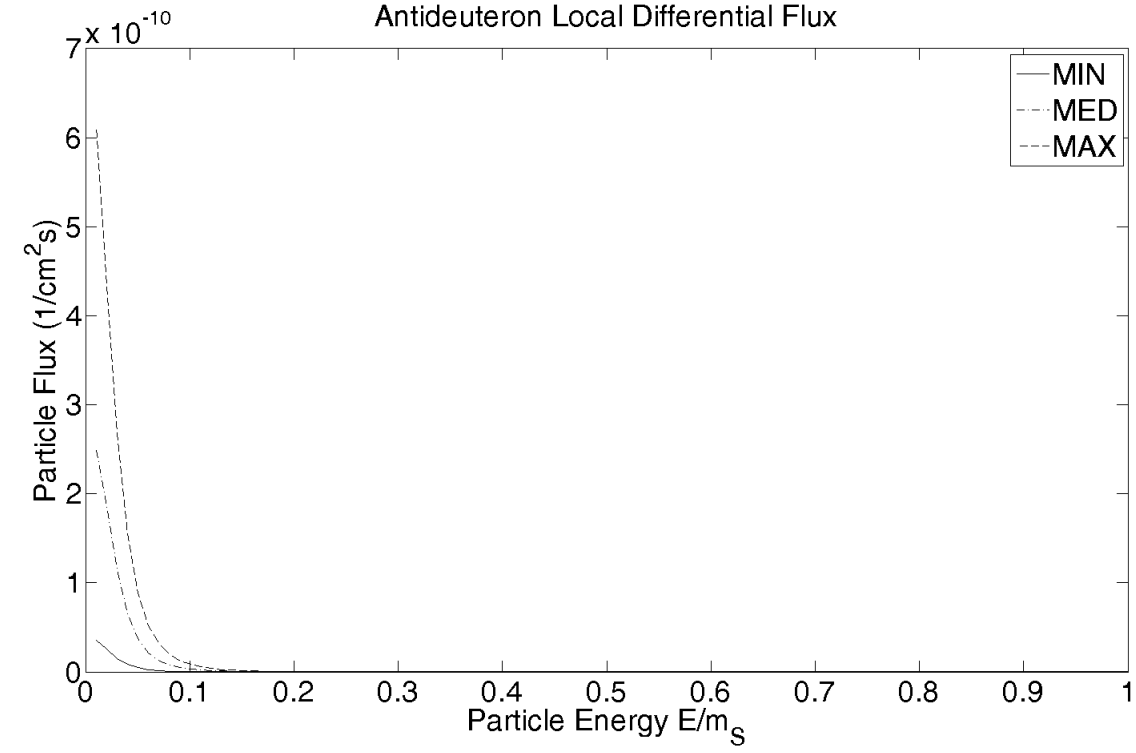

Figure 5.20: Local Antideuteron Flux ($m_S = 700$ GeV)

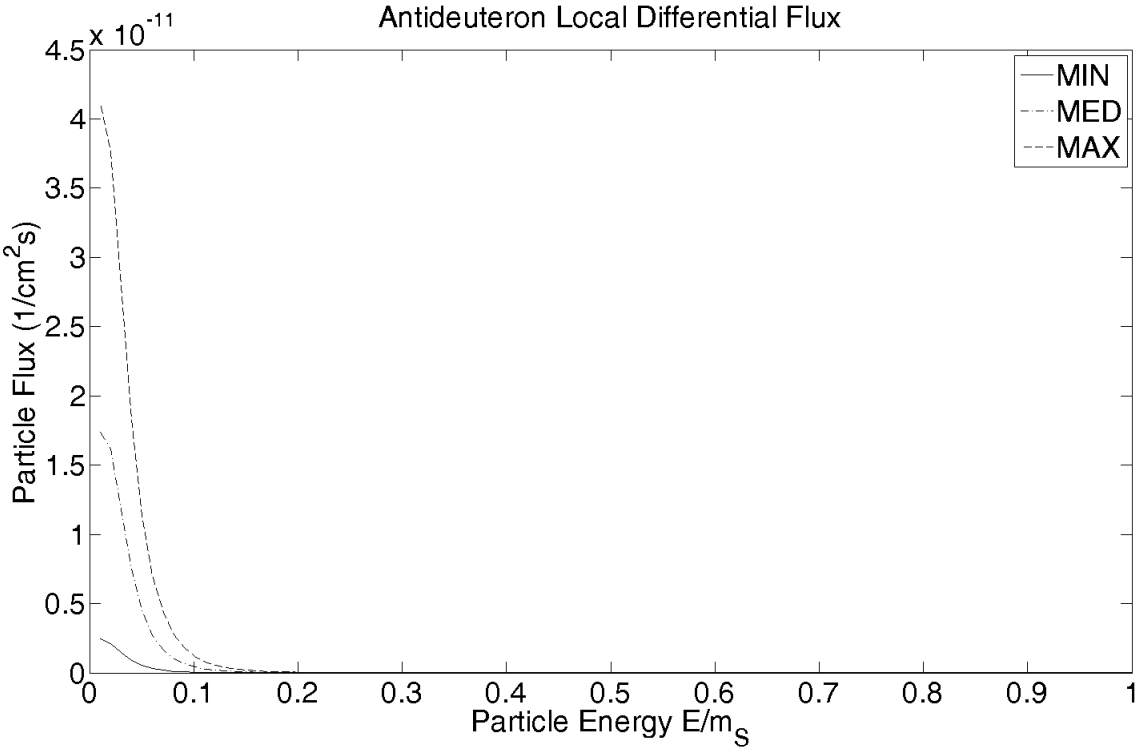

Figure 5.21: Local Antideuteron Flux ($m_S = 1000$ GeV)

The AMS-II is a general purpose high energy particle detector that is based on the International Space Station. It is expected to measure the composition and energy spectra of charged particles with an accuracy of 1%, over an energy range of 0.5 - 2000 GeV. The basic spectrometer design is similar to that of PAMELA, and it operates in a similar fashion. One of the additional systems on the AMS-II is a Cherenkov detector to estimate charge.

The AMS-II should be providing updated data within the next few years. When this data is reported, a full comparison can be made, allowing the validity of the model to be tested.

It should be noted that, while PAMELA and the antimatter component of the Fermi-LAT have recorded a steady flux of positron and antiproton events, no cosmic antideuterons have yet been observed. This is consistent with their expected background abundance as calculated, up to the uncertainties inherent in the problem, but it makes any claim about an exotic antideuteron signal unsupported. The AMS-II is expected to be probing the energy regions where cosmic antideuterons should lie as it collects data. It is expected to provide evidence of the antideuteron flux.

Chapter 6

Neutrino Signals of Singlets

The final signal of dark matter annihilation we will consider will be the neutrino signal. Neutrinos comprise a significant portion of the final state particle array of many decay processes in the $\mathcal{SM}$. They are stable and have very small mass, propagating at close to the speed of light. However, they interact with other matter only through the weak force. This, when combined with their low mass, makes them exceptionally difficult to detect. Only recently have neutrino telescopes become feasible.

While a neutrino signal of dark matter annihilations from the galactic halo may be present, actually detecting such a signal, given the relative sparsity of the particles comprising the halo, would be difficult. It would be better if we somehow had a high density region of dark matter particles to produce a stronger signal that could then be focused on. In fact such higher density sources exist, and they come about in such a way that we can only hope to observe them by a neutrino signal.

As a massive body travels through the galactic halo, it passes through clouds of dark matter particles. Some of these dark matter particles interact with the constituent particles of the massive body and some, in doing so, lose enough energy that they become gravitationally trapped. These trapped dark matter particles tend to accumulate while annihilating until they reach some kind of stable equilibrium between capture and annihilation. The majority of the products of these annihilations never reach the surface of the body of course, but the high penetrative power of neutrinos allows most of them to escape, providing a measurable signal.

In this chapter, we calculate the expected neutrino signal from the annihilation of singlets that have been gravitationally captured by the Sun. First, the singlet capture rates for the Sun are found, leading to the equilibrium abundances. Then the neutrino spectra from singlet annihilations can be computed. Finally, the outward propagation of the neutrinos from the annihilation region to the detectors on the Earth will be considered, including both scattering and oscillation effects. We then present some details of current generation neutrino telescopes and consider the possibility of observing a neutrino signal from singlet annihilations in the Sun.

6.1 Capture of Singlets

We use the results originally calculated by Gould [64] [65] in this section, as they have become the standard method for computing WIMP capture rates by massive bodies.

The number of captured singlets N in a massive body can be described by the differential equation

$$\frac{dN}{dt} = C - AN^2 - EN$$

with the C, A, and E terms each representing gravitational capture of singlets, annihilation of captured singlets, and evaporation of captured singlets, respectively. The capture rate C depends primarily on the nuclear recoil cross section for singlets and the properties of the matter making up the massive body, while the annihilation rate appears to depend directly on the singlet annihilation cross section. In general, the solution of this equation is complicated, but the assumption that evaporation is negligible ($E \simeq 0$) allows considerable simplification. Evaporation describes what happens when a captured singlet gains enough kinetic energy via elastic recoils with the medium of the capturing body that it can escape the gravitational potential. Obviously, evaporation requires that the singlet have a recoil cross section that is not too low as well as a mass that is not too high. For singlets with a mass of over a few GeV, the probability of escape by evaporation is essentially nonexistent. A detailed discussion of evaporation can be found in a recent paper by Kappl and Winkler [80].

Neglecting evaporation, the equation can be solved exactly to give

$$N(t) = \sqrt{\frac{C}{A}} \tanh\left(\sqrt{CA}t\right)$$

If we take $t = t_\odot \simeq 4.6 \times 10^9$ years (roughly the age of the Sun), then if $\sqrt{CA}t_\odot \gg 1$ we have an equilibrium solution for the present time, and the current singlet number density is constant. By writing the current annihilation rate as

$$\Gamma_{ann} = \frac{1}{2}AN^2$$

and substituting in the exact solution above, we get

$$\Gamma_{ann} = \frac{1}{2}C \tanh^2\left(\sqrt{CA}t\right) \simeq \frac{1}{2}C$$

where the approximation is due to $\sqrt{CA}t_\odot \gg 1$.

So in equilibrium, the annihilation rate of captured singlets depends only on the capture rate. Since the capture rate depends on the nuclear recoil cross section and not the annihilation cross section, so does the equilibrium annihilation rate.

We now review the computation of the capture rate for singlets in the Sun. We assume ambient singlets have a Maxwellian velocity distribution with respect to the Sun, of the form

$$\frac{f(u)}{u} = \sqrt{\frac{3}{2\pi}} \frac{\rho_0}{m_S v_d v_\odot} \left[\exp\left(-\frac{3\left(u - v_\odot\right)^2}{2v_d^2}\right) - \exp\left(-\frac{3\left(u + v_\odot\right)^2}{2v_d^2}\right)\right]$$

where $v_d = 270$ km/s is the dispersion velocity of the singlets and $v_\odot = 220$ km/s is the relative velocity of the Sun as it moves through the galactic halo. The local singlet density is $\rho_0 = 0.3$ GeV/cm^3, as always. We can write the total capture rate for the Sun in terms of a sum over capture rates for individual elements

$$C = \int_0^{R_\odot} dr 4\pi r^2 \sum_i \frac{dC_i(r)}{dV}.$$

The elemental capture rates can be found from

$$\frac{dC_i(r)}{dV} = \int_0^{u_{max}} du \frac{f(u)}{u} \Omega_{v,i}(w)$$

where $\Omega_{v,i}(w)$ is the capture probability per unit time for element i, and it depends on $w = \sqrt{u^2 + v^2}$, which is the singlet velocity $v(r)$ in terms of the singlet escape velocity at that point in the Sun . The solar escape velocity at an interior point of distance r from the center of the Sun can be approximated by [65]

$$v^2(r) = v_c^2 - \frac{M(r)}{M_\odot}\left(v_c^2 - v_s^2\right)$$

where v_c is the escape velocity at the center of the Sun and v_s is the escape velocity at the surface of the Sun. $M(r)$ is the solar mass interior to r and $M_\odot = 1.998 \times 10^{30}$ kg is the total solar mass. The upper limit of integration u_{max} is the velocity at which singlets will scatter to the escape velocity, so integrating past that will overcount the number of singlets captured. This velocity is $u_{max} = 2v\frac{\sqrt{\mu}}{\mu - 1}$ with $\mu = m_S/m_i$ for the atomic mass m_i of element i in the Sun. We appromximate the solar mass function $M(r)$ by using the basic polytrope 3 solution for the Lane-Emden equation, which corresponds to the basic Eddington standard model for main sequence stellar structure.

The capture probability $\Omega_{v,i}(w)$ is somewhat complicated. For nuclei larger than Hydrogen, singlet scattering from the nuclei is decoherent, which needs to be taken into account. We follow Wikström and Edsjö [121] and use a Helm-Gould exponential form factor [64]

$$\left|F_i\left(q^2\right)\right|^2 = \exp\left(\frac{-\Delta E}{E_i^0}\right)$$

for a scattering of momentum transfer q on element i, where the parameters are defined by

$$\Delta E = \frac{q^2}{2m_S}$$

$$E_i^0 = \frac{3\hbar^2}{2m_S R_i^2}$$

with a nuclear radial factor of

$$R_i = \left[0.91\left(m_i/GeV\right)^{1/3} + 0.3\right] 10^{-15} m.$$

These allow the analytic evaluation of the capture probability for each element

Element	Abundance (Logarithmic)
H	12
He	10.90
C	8.39
N	7.83
O	8.69
Ne	7.87
Mg	7.55
Si	7.54
S	7.19
Fe	7.47

Table 6.1: Solar Abundances (logarithmic astronomical scale)

$$\Omega_{v,i}(w) = \sigma_i n_i \frac{(\mu+1)^2}{2\mu} E_i^0 \left\{ \exp\left(-\frac{m_S u^2}{2E_i^0}\right) - \exp\left(-\frac{2\mu}{(\mu+1)^2}\frac{m_S\left(u^2+v^2\right)}{E_i^0}\right)\right\}$$

The number density of element i in the Sun is n_i and the nuclear recoil cross section σ_i can be written in terms of the nucleon-singlet scattering cross section as computed in Chapter 3

$$\sigma_i = \sigma_{SN\to SN} A_i^2 \frac{(m_S m_{A_i})^2}{(m_S + m_{A_i})^2}\frac{(m_S+m_p)^2}{(m_S m_p)^2}$$

for a nucleus with mass number A_i and nuclear mass m_{A_i}, and where m_p is the proton mass as usual. As in Chapter 5, we compute all cross sections with $\eta = 0.1$.

We use the solar abundances as reported in [88] and reproduced in Table 6.1. The elements included are H, He, C, N, O, Ne, Mg, Si, S, and Fe, which are the ten most abundant elements in the Sun according to photospheric spectral analysis. The abundance scale used is the logarithmic astronomical scale, based off the abundance of hydrogen $A(H)$. In this scale $A(H) \equiv 12$, and the abundance of an element $A(El)$ is given in terms of its number density $n(El)$ with reference to the number density of hydrogen by

$$A(El) = \log\left[n(El)/n(H)\right] + 12.$$

We plot here the capture rate (Figure 6.1) as a function of singlet mass to exhibit the basic behavior of the function. It is important that higher mass singlets have a significantly lower rate of capture than those with less mass. There are minor resonances hiding in the low mass range, coincident with the atomic masses of the elements included, but they are swamped by the basic kinematical structure of the capture model.

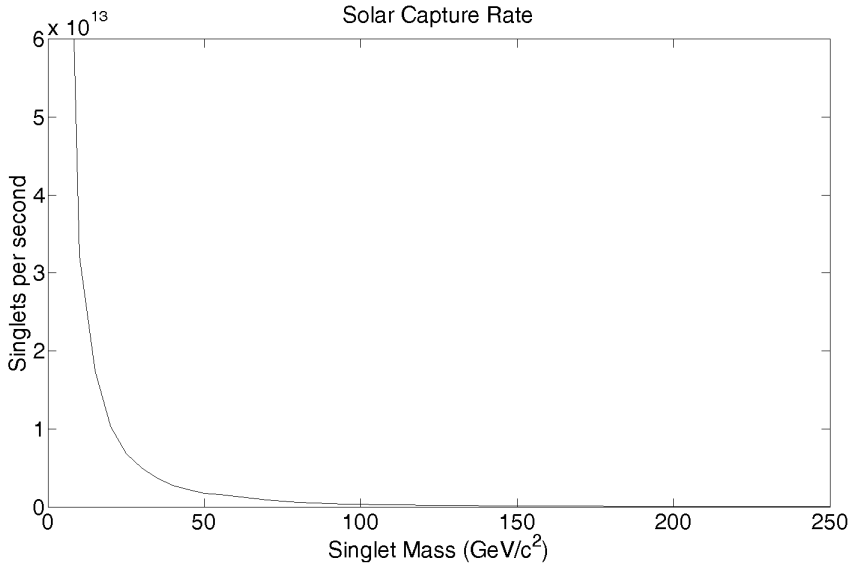

Figure 6.1: Solar Singlet Capture Rate

6.2 Neutrino Production

Captured singlets annihilate at a rate governed by the capture rate as described in the previous section. For singlet populations in massive bodies such as the Sun, many of the annihilation products are absorbed by the surrounding medium or decay before they can interact. Of all the standard model particles, the only ones that can escape with such ease as to leave their production spectrum recognizable are neutrinos. In this section, we compute the neutrino energy spectrum resulting from singlet annihilations.

In modern literature, neutrino spectra are all computed using software packages such as `PYTHIA`, which is capable of taking into account most of the relevant effects such as hadronization. The spectra so produced are more detailed and more accurate than anything that can be done analytically, but we brifely review some of the analytic terms anyway. The most complete reference for the computation of the spectra of neutrinos produced by the annihilation or decay of captured particles was written by Jungman and Kamionkowski in the mid 1990s [77], and remains the most accurate analytic treatment.

The computation uses equations (5.1) and (5.2) from Chapter 5, where they were applied to antimatter. As mentioned in Chapter 2, singlets do not annihilate directly to neutrinos in our model, so any neutrinos produced are due to decays of primary or secondary annihilation products. The basic number density of neutrinos produced from singlet annihilations can be found from the expression

$$\frac{d\mathcal{N}_\nu}{dE_\nu}\left(E_{in}, E_\nu\right) = \int_{E_{min}}^{E_{max}} dE' \frac{d\mathcal{N}_{SS\to f}}{dE'}\left(E_{in}, E'\right) \frac{d\mathcal{N}_{f\to\nu}}{dE_\nu}\left(E', E_\nu\right) \tag{6.1}$$

which expresses the number density of neutrinos produced from singlet annihilation to state f and then

decay of state f into neutrinos.

We are dealing with energy spectra, so we need to be careful with the kinematics. The final state neutrinos are produced in a rest frame that is different from the center of mass frame of the annihilating singlets. To take this into account, we need to perform a Lorentz boost on the function $\frac{d\mathcal{N}_\nu}{dE_\nu}(E', E_\nu)$ to ensure the neutrinos have the right energy. We can perform the boost by acting on the rest frame distribution by

$$\left.\frac{d\mathcal{N}_\nu}{dE_\nu}\right|_{boosted}(E, E_\nu) = \frac{1}{2}\int_{E_-(E)}^{E_+(E)} \frac{d\epsilon}{\epsilon}\frac{1}{\gamma\beta}\left.\frac{d\mathcal{N}_\nu}{dE_\nu}\right|_{rest}(\epsilon, E) \tag{6.2}$$

with $\beta = v/c$ the scaled velocity of the decaying particle and $\gamma = 1/\sqrt{1-\beta^2}$ as usual. The integration limits are $E_\pm(E) = \frac{E_\nu}{\gamma(1\mp\beta)}$.

Insertion of this boost and the actual expressions in terms of center of mass cross sections and decay rates leads to a complicated expression. The expression can be simplified by noting that we work in the nonrelativistic limit for the singlets, meaning that the injection energy is always $E_{in} = 2m_S$. This allows us to ignore the integral over E in (6.1), making the production spectrum simply a product rather than a convolution.

The above expression needs to be modified for secondary neutrino producing decay channels, such as the heavy boson decays. In such cases there needs to be two or more boosts, one for each decay, until the final neutrino states are achieved. This can get exceedingly complex. When one tries to take into account stopping effects from secondary particles interacting with the capturing medium before they decay, the analytical approach is stretched to its limit. We proceed by following the work of Cirelli and collaborators [32], who provide numerical functions for neutrino production spectra.

When we work with singlets in the intermediate mass range of 81-1000 GeV, we consider only the following annihilation channels: top quark ($t\bar{t}$), W boson (W^+W^-), Z boson (ZZ), and Higgs boson (hh). For singlet masses in the 5-81 GeV range, we consider the bottom quark ($b\bar{b}$), charm quark ($c\bar{c}$), and tau lepton ($\tau\bar{\tau}$) to be the primary annihilation channels for the singlet. The cross sections for each of these annihilation events can be found in Chapter 2. Neutrinos can be produced from the direct decay of gauge bosons and leptons, or from the decay of hadrons resulting from hadronized quarks. All quarks but the t can hadronize before they decay, leading to a complicated spectrum. There is also a significant contribution from secondary decays, like the $h \to b\bar{b} \to X \to \nu$ channels or the $t \to Wb \to X \to \nu$ channels. The lepton component is really only due to the τ decay. Muons have such a long lifetime that they interact substantially with the capturing medium before they decay, losing enough energy that any neutrinos produced are of too low energy to be interesting.

While previous authors in this area often computed only the muon neutrino flux, as that is usually what is detected in high energy neutrino detectors, we report all three neutrino flavor spectra. This is because oscillations, which will be discussed in the next section, are also being taken into account, so the neutrino spectra at production are not the same as the neutrino spectra at detection. The above mentioned collaboration [32] has produced the basic neutrino spectra for certain $\mathcal{SM}$ annihilation channels. These spectra are independant of the specific model of dark matter used, having been computed from the decays of

$\mathcal{SM}$ particles of a given energy to neutrinos only. With the branching ratios to each of the singlet annihilation channels, we can use these basic decay spectra to construct the neutrino spectrum from singlet annihilations. The differential flux is

$$\frac{d\mathcal{N}_\nu}{dE_\nu} = \frac{\Gamma_{ann}}{4\pi d^2} \sum_f BR_f \frac{dN_\nu^f}{dE_\nu}.$$

The $\frac{dN_f}{dE}$ are the provided spectra, and BR_f is the branching ratio for singlet annihilation to final state f. The annihilation rate Γ_{ann} was computed in the above section, and d is the distance from the production region to the detector, in this case the distance from the Earth to the Sun.

The numerical neutrino production spectra provided have been fit to a function of the form

$$\frac{d\mathcal{N}_f}{dx} = a_0 \left(1 + a_1 w + a_2 w^2 + a_3 w^3 + a_4 w^4 + a_5 w^5\right) (1-x)^b + c_0 x^{c_1} (1-x)^{c_2}$$

where $x = E_\nu / m_S$ and $w = \log_{10}(x)$. The parameters for the various annihilation channels, which depend on neutrino flavor and available energy, are found online and in the literature [32]. This analytic approximation is accurate to the per cent level, but we use the available numerical functions.

In Figures 6.2 - 6.7 we plot the provided neutrino spectra for each of the relevant annihilation channels. We have included only the relevant annihilation channels at each mass value. The reason for the seperation of the τ flavor from the other two as explained above was that the τ lepton annihilation products can decay and contribute to the neutrino flux while the other charged leptons cannot, leading to an imbalance in neutrino flavor. At this point, these fluxes apply to both neutrinos and antineutrinos, with the differences between the two only showing up during propagation. As expected, the neutrino energies are weighted toward the low end of the scale.

6.3 Propagation

The propagation of neutrinos between the point of production and the point of detection on the Earth is not as simple as it was once thought to be. As the neutrinos propagate outward through the capturing body, they interact with it through both neutral current and charged current weak interactions (scattering from nuclei via intermediate Z and W bosons). The primary effect of these interactions is energy loss, though the charged current interactions can involve flavor changing effects. The relevance of these effects depends on neutrino energy, and for neutrinos travelling through the solar medium these terms can be ignored for E_ν <100 GeV. Since the higher mass singlets being considered here can produce neutrinos with that order of energy, the absorption terms cannot be neglected. These effects are straightforward to deal with, but less so is the oscillation that needs to be addressed for propagating neutrinos.

Though it was first proposed decades ago, soon after Kaon oscillation was observed, it has only recently been confirmed that neutrinos undergo flavor oscillations as they propagate. In terms of theory, this means that the neutrino mass eigenstates $\{\nu_i\}$, $i = 1, 2, 3$ and the neutrino flavor eigenstates $\{\nu_\alpha\}$, $\alpha = e, \mu, \tau$ are not identical, but are related by a mixing matrix V which has been experimentally determined:

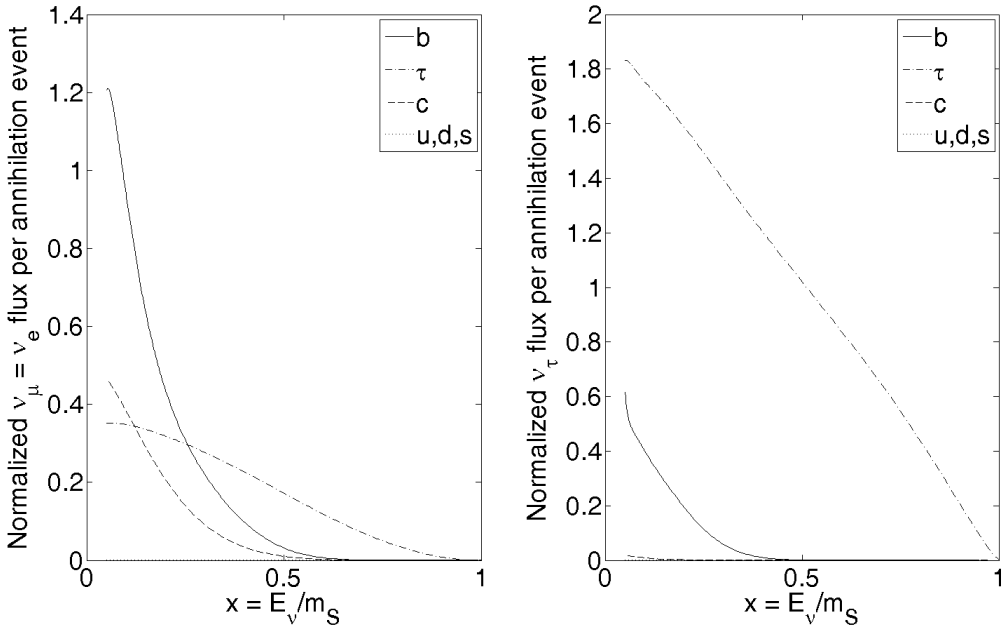

Figure 6.2: Neutrino Production Spectra ($m_S = 10$ GeV)

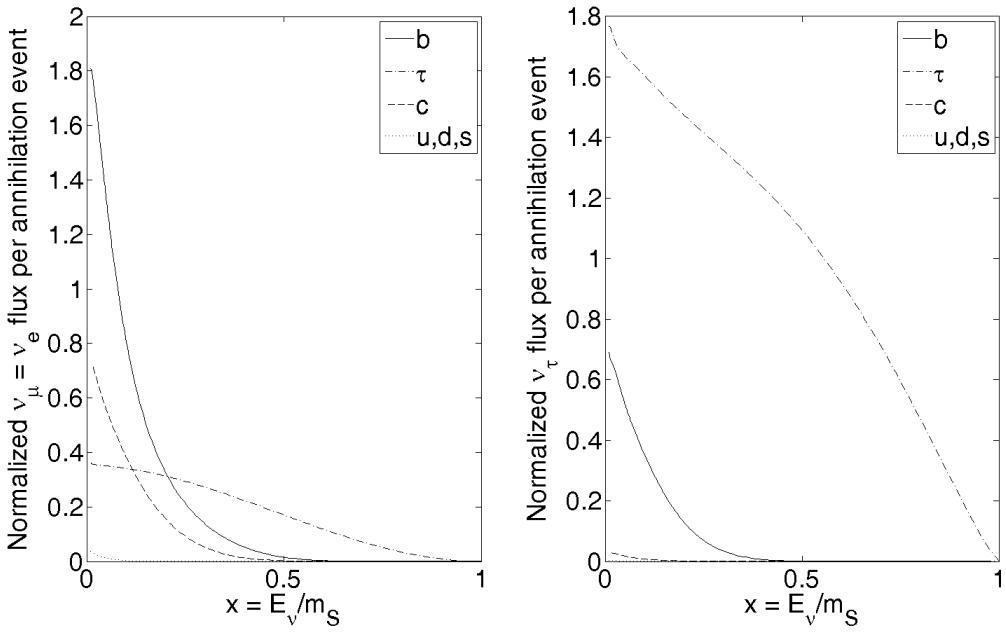

Figure 6.3: Neutrino Production Spectra ($m_S = 50$ GeV)

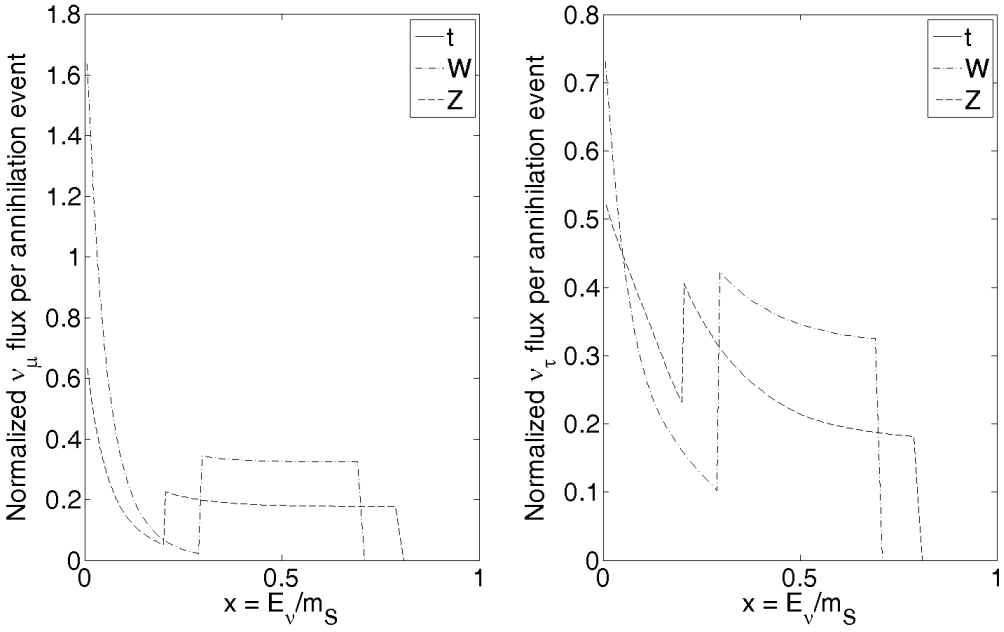

Figure 6.4: Neutrino Production Spectra ($m_S = 100$ GeV)

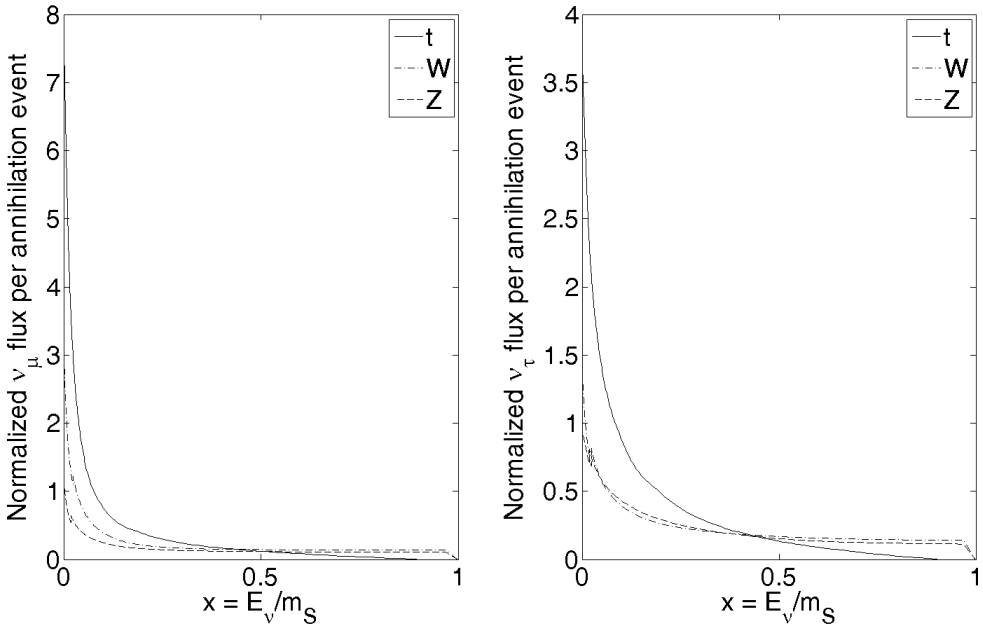

Figure 6.5: Neutrino Production Spectra ($m_S = 300$ GeV)

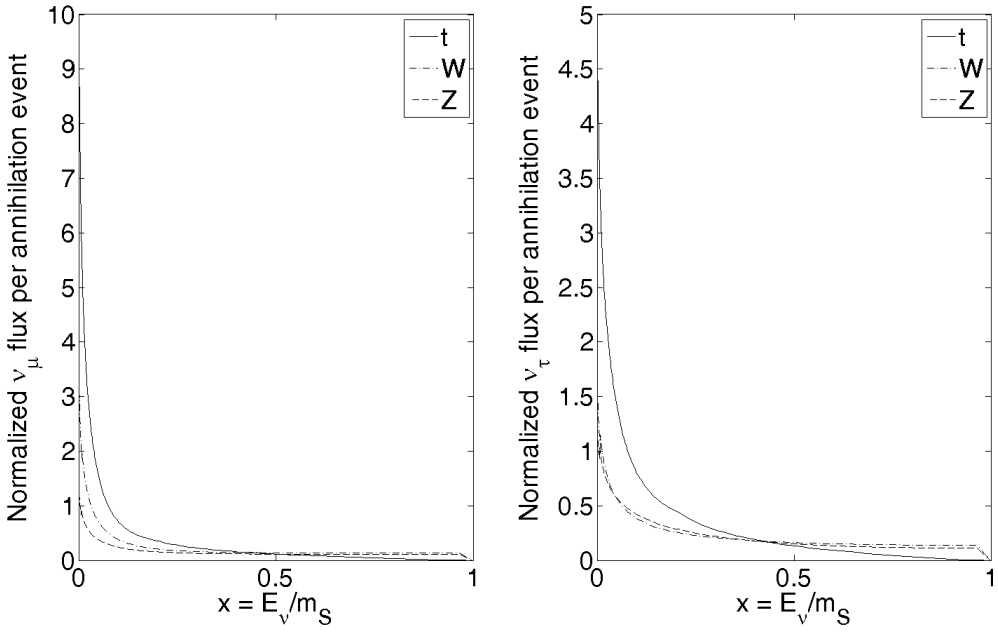

Figure 6.6: Neutrino Production Spectra ($m_S = 500$ GeV)

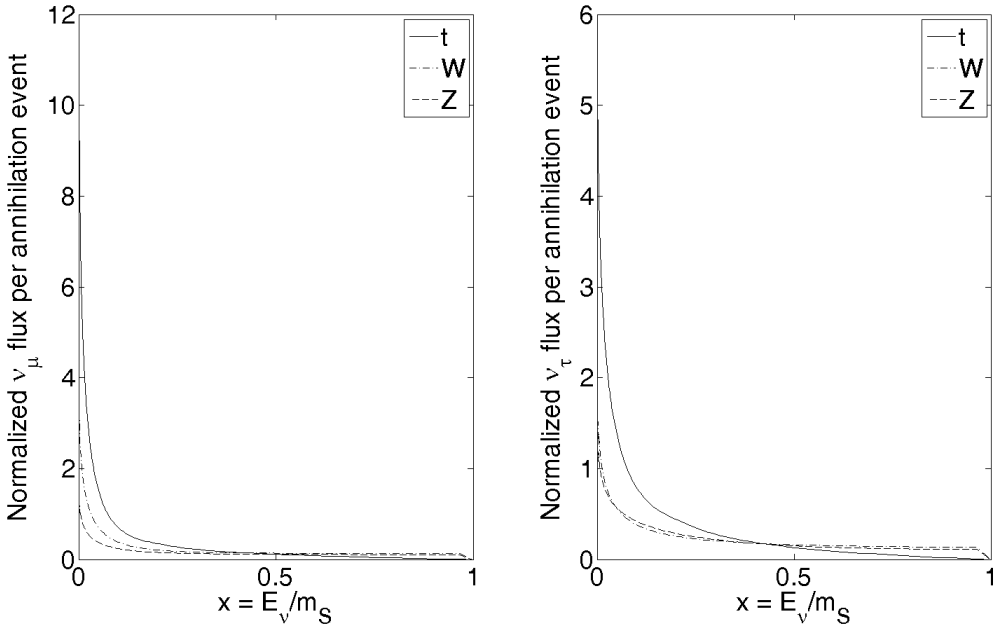

Figure 6.7: Neutrino Production Spectra ($m_S = 700$ GeV)

$$\begin{pmatrix} \nu_e \\ \nu_\mu \\ \nu_\tau \end{pmatrix} = V \begin{pmatrix} \nu_1 \\ \nu_2 \\ \nu_3 \end{pmatrix}. \tag{6.3}$$

Phenomonologically, this means that the flavor ratio $\nu_e : \nu_\mu : \nu_\tau$ of the neutrino signal at production will be different from the flavor ratio at detection. The consequences are numerous, the most relevant one to us being that even if we only want to compare a muon neutrino signal with a certain experiment, we need to compute the production spectra of all three flavors.

The usual treatment of neutrino propagation is to follow the work by Strumia and Vissani [116], and use the density matrix formalism. This allows us to combine oscillations and interactions into a single equation for the flavor density matrix. This equation is

$$\frac{d\rho}{dr} = i\left[H, \rho\right] + \left.\frac{d\rho}{dr}\right|_{NC} + \left.\frac{d\rho}{dr}\right|_{CC} - \epsilon\left[H, \left[H, \rho\right]\right].$$

The solution $\rho\left(r, E\right)$ is the 3x3 flavor density matrix, whose diagonal entries are flavor eigenstates and whose off-diagonal entries are superpositions of flavor states. The independent variable r is the propagation distance. The first term describes oscillations, the second and third terms describe neutral current and charged current interactions, respectively, and the final term describes decoherence. The initial condition for this equation is the initial production spectrum for each flavor, as described in the previous section, placed along the diagonal.

The decoherence term describes the fact that not all neutrinos are created at the same spatial point, and so some will propagate slightly different distances through the production region. Since we are assuming the neutrinos are all produced at the center of mass of the capturing body, this term vanishes. This assumption can be justified by showing that taking the average over the production region is negligibily different from taking production to be at the center of mass point [32].

Neutral current interactions essentially remove a neutrino from the flux and reinsert it at a lower energy. The term can be written

$$\left.\frac{d\rho}{dr}\right|_{NC} = -\int_0^{E_\nu} dE'_\nu \frac{d\Gamma_{NC}}{dE'_\nu}\left(E_\nu, E'_\nu\right)\rho\left(E_\nu\right)$$

$$+\int_{E_\nu}^{\infty} dE'_\nu \frac{d\Gamma_{NC}}{dE'_\nu}\left(E_\nu, E'_\nu\right)\rho\left(E'_\nu\right).$$

The differential cross section $\frac{d\Gamma_{NC}}{dE'_\nu}\left(E_\nu, E'_\nu\right)$ describes the scattering of neutrinos off of neutrons and protons in the propagation medium. The first term describes absorption and the second term describes reinsertion.

The charged current interactions, at tree level at least, are due to u-channel and t-channel interactions with an intermediate W boson (see Figure 6.8), though the full deep inelastic scattering treatment is required for

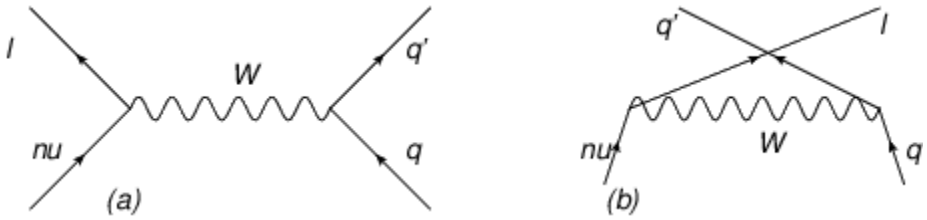

Figure 6.8: Charged Current Neutrino-Nucleon Scattering (a) t-channel (b) u-channel

accurate results at higher energies. The neutrino scatters off of a quark in a nucleon, leading to the production of a charged lepton, which may decay, and a different quark, which will hadronize. Both the charged lepton and the hadron jet can decay back into neutrinos. Since electrons do not decay, and muons are stopped before they can decay, only the τ leptons can have decays contributing to the flux.

This results in more τ neutrinos being reinjected into the flux than the other two flavors, leading to the effect called ν_τ regeneration. The charged current term can be written

$$\left.\frac{d\rho}{dr}\right|_{CC} = -\frac{\{\Gamma_{CC}, \rho\}}{2} + \int \frac{dE_\nu^{in}}{E_\nu^{in}} [\Pi_\tau \rho_{\tau\tau} \left(E_\nu^{in}\right) \Gamma_{CC}^{\tau} \left(E_\nu^{in}\right) f_{\tau\to\tau} \left(E_\nu^{in}, E_\nu\right)$$

$$+\Pi_{e,\mu} \bar{\rho}_{\tau\tau} \left(E_\nu^{in}\right) \bar{\Gamma}_{CC}^{\tau} \left(E_\nu^{in}\right) f_{\bar{\tau}\to e,\mu} \left(E_\nu^{in}, E_\nu\right)].$$

The braces { , } indicate an anticommutator, and that term describes the initial absorption process. The second term describes the reinsertion and the resulting ν_τ regeneration effects. The Γ matrices express absorption rates and the f are energy distributions of secondary neutrinos. The Π are 3x3 flavor projectors. Further details and discussion of the implementation are both available in the reference [116].

Needless to say, both of these terms are nonzero only inside the capturing body. Once the neutrinos have propagated outside into the vacuum, these terms vanish due to the low density of the interplanetary medium.

The oscillation term is simply the commutator of the density matrix with the oscillation Hamiltonian H. The operator H describes the oscillations of ultrarelativistic neutrinos in matter. It can be written in the form

$$H = \frac{m \cdot m^\dagger}{2E} + A.$$

The term A is the matter potential, taking the form of a 3x3 flavor matrix. It embodies how the above discussed neutral and charged weak current scatterings off of the surrounding matter alter the oscillation probabilities. It has a basic form of

$$A = \sqrt{2} G_F \left[N_e diag\left(1,0,0\right) - \frac{N_n}{2} diag\left(1,1,1\right) \right]$$

for 'normal' matter which is essentially electronic with negligible antimatter. The N_e and N_n are the electron and neutron number densities of the propagation medium, respectively. The factor G_F is Fermi's

constant. Obviously, A must be very close to zero in the interplanetary medium, leaving only the basic oscillation Hamiltonian.

The energy of the neutrinos is E, and the factor $m \cdot m^\dagger$ is given by

$$m \cdot m^\dagger = V^\star \cdot diag\left(m_1^2, m_2^2, m_3^2\right) \cdot V^T$$

where V is the neutrino mixing matrix as defined in (6.3). The m_i are neutrino mass eigenvalues. For antineutrinos, the Hamiltonian must be transformed as $m \cdot m^\dagger \to m^\dagger \cdot m$ and $A \to -A$.

Given an initial spectrum, the easiest way to obtain a solution to this equation is to simply propagate the initial condition step by step to the required propagation distance. While exact solutions likely exist for the vacuum case, the complexity of the interaction terms precludes their existence for propagation through matter. As with the production spectra, we use the post-propagation spectra that have been compiled [32]. The full details of the assumptions that were made and the numerical values used for various quantities are detailed in the reference.

In Figures 6.9 - 6.14 are plots of the neutrino flux from singlet annihilations in the Sun as they look after propagation to Earth. We have included the flux for singlet mass values of m_S = 10, 50, 100, 300, 500, and 700 GeV. Due to the need to include the neutrinos from Higgs decays for those singlet mass values which have an open Higgs annihilation channel, which were not present in the provided spectra, the numerically implemented Lorentz boost (6.2) has induced a certain block structure to the spectra.

6.4 Discussion

We consider the neutrino flux from singlet annihilations in the Sun in the context of the results from the Super Kamiokande detector [36] in Japan and the lack of results from the IceCube [68] detector in Antarctica.

Super Kamiokande is a solar neutrino detector at heart, and focuses much of its attention on the Sun. It was recently reported that Super Kamiokande did not observe any excess neutrinos from the Sun during its last analysis period [118]. The neutrino fluxes predicted for most of our mass range are small enough that they could be hiding in the background of this data set, but the magnitude of the fluxes from some of the lighter mass singlets makes finding an unobserved neutrino signal from them unlikely.

A full analysis needs to wait until the IceCube solar data is available, and until the DeepCore experiment is fully integrated. DeepCore will lower the energy threshold for IceCube from 10 GeV to the 100 MeV scale. At this time, given how much of the neutrino signal is expected to lie below 10 GeV, analysis of these results with respect to IceCube data makes little sense.

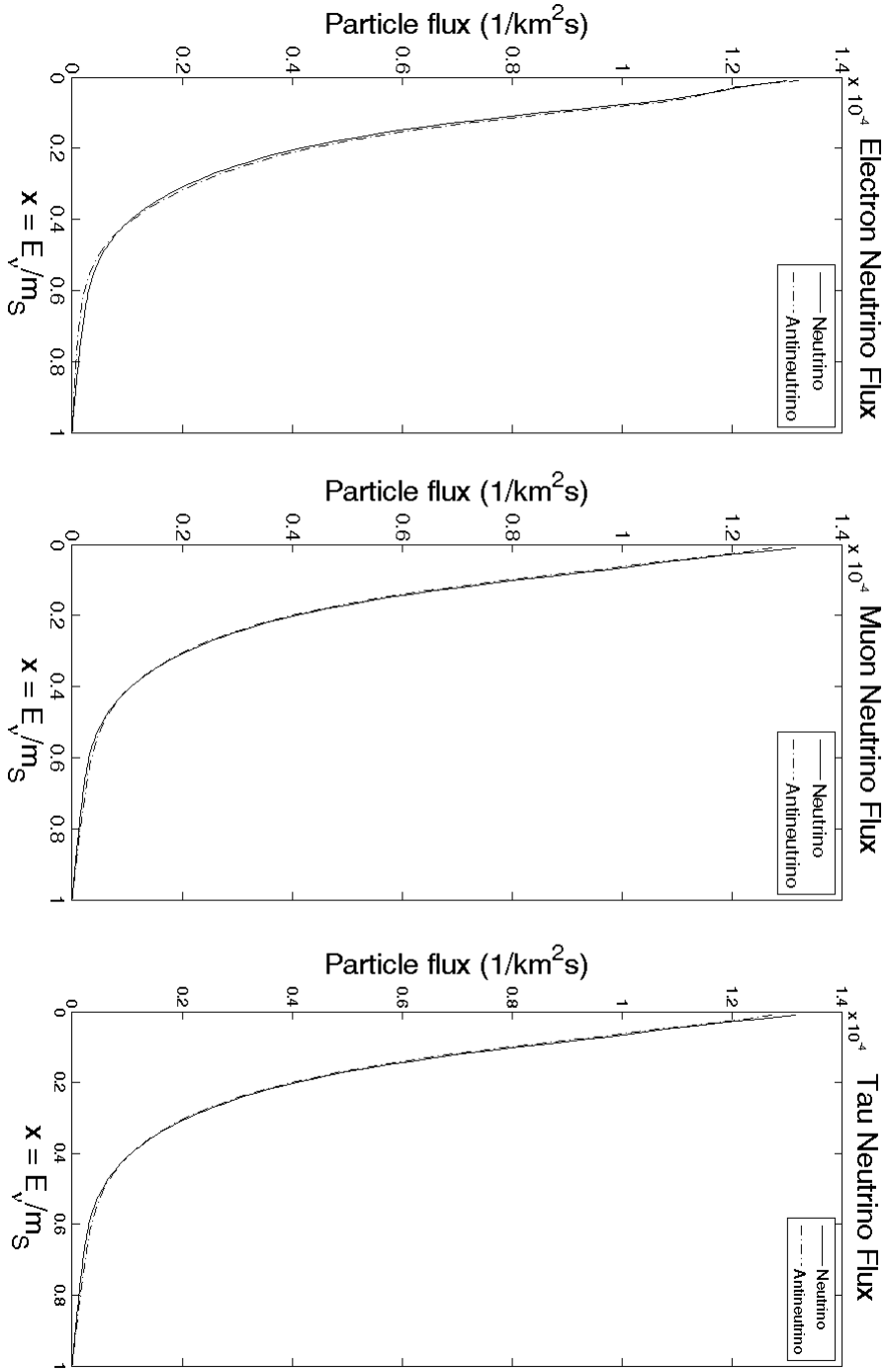

Figure 6.9: Local Neutrino Flux ($m_S = 10$ GeV)

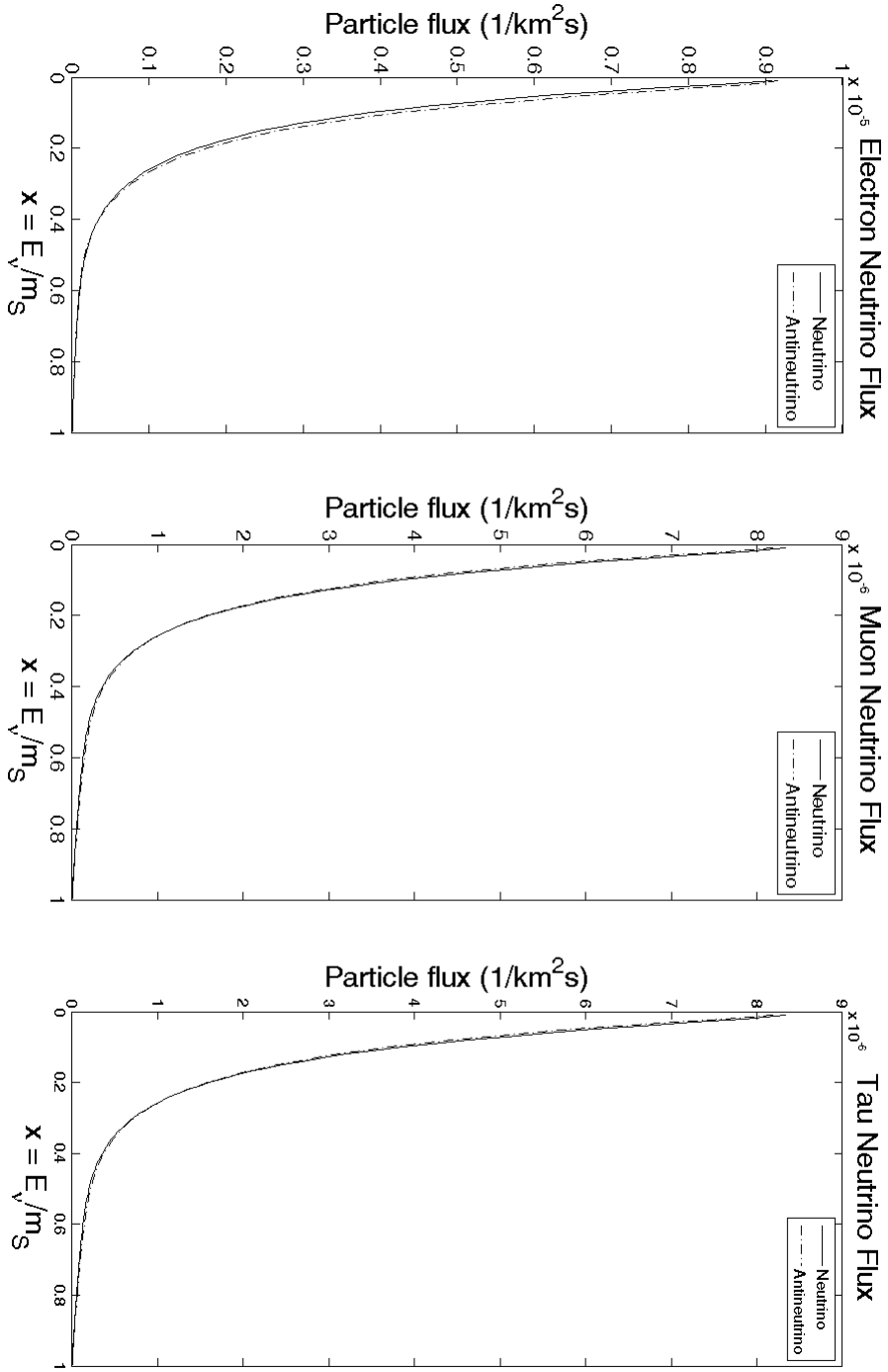

Figure 6.10: Local Neutrino Flux ($m_S = 50$ GeV)

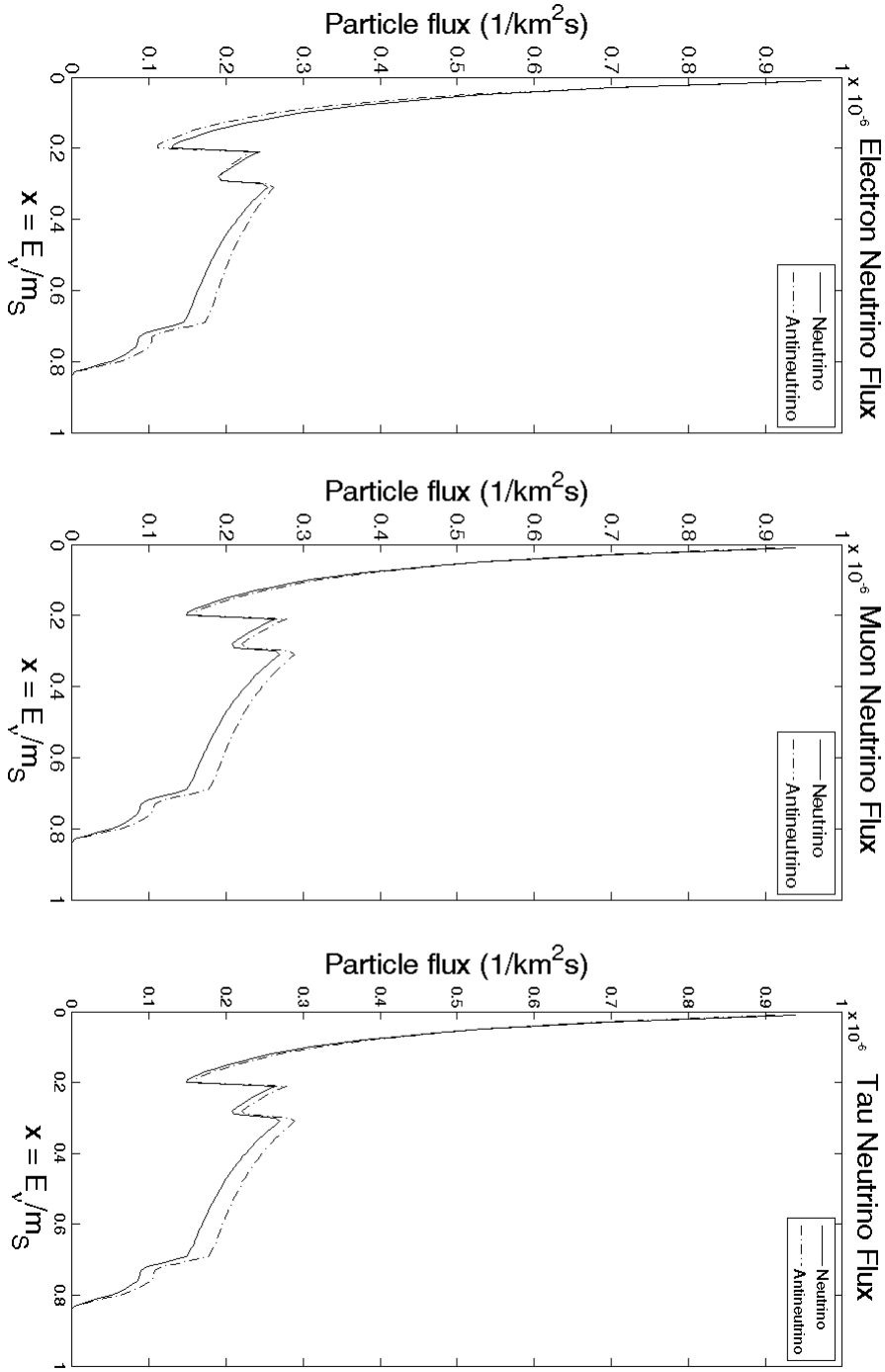

Figure 6.11: Local Neutrino Flux ($m_S = 100$ GeV)

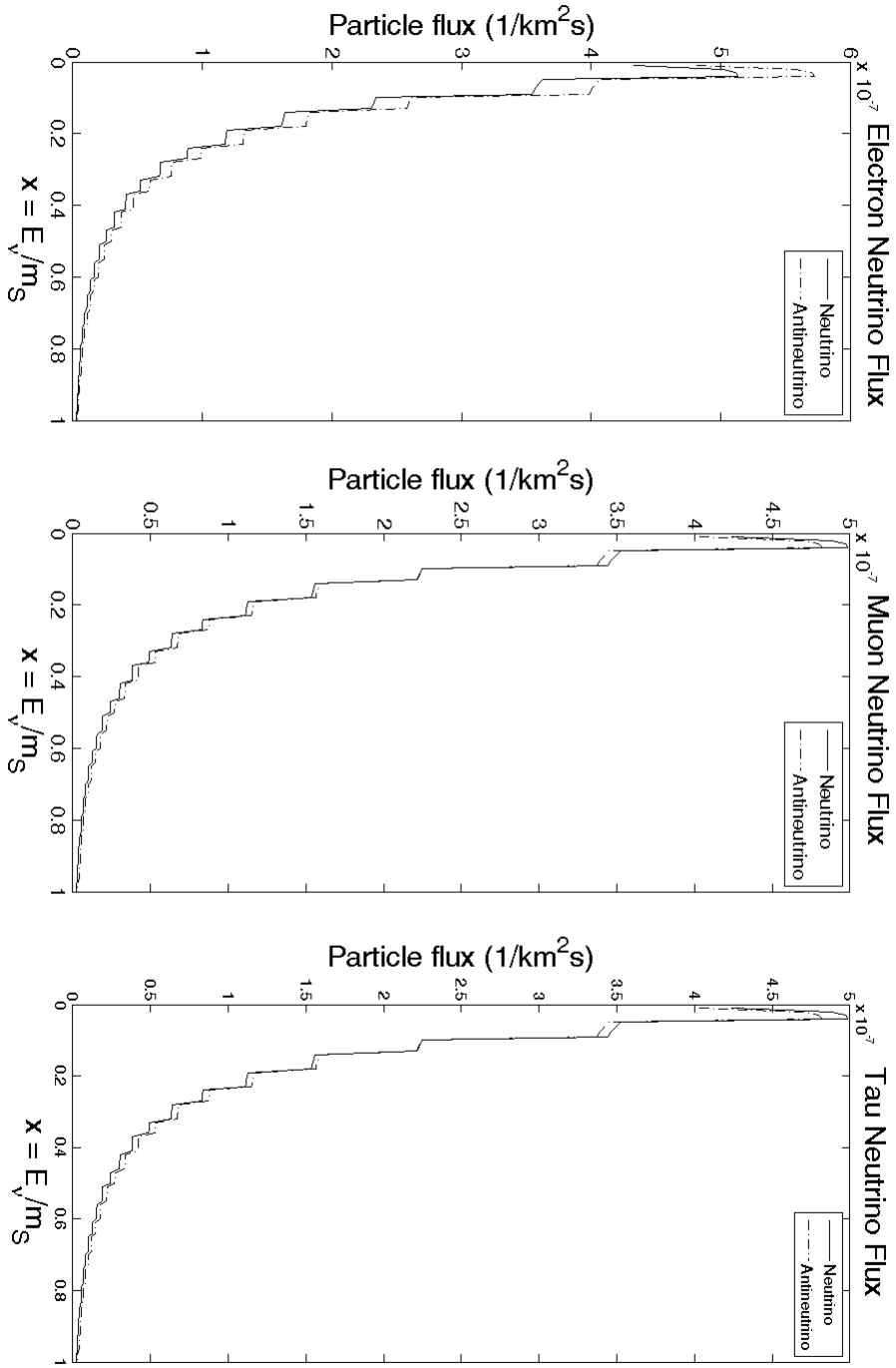

Figure 6.12: Local Neutrino Flux ($m_S = 300$ GeV)

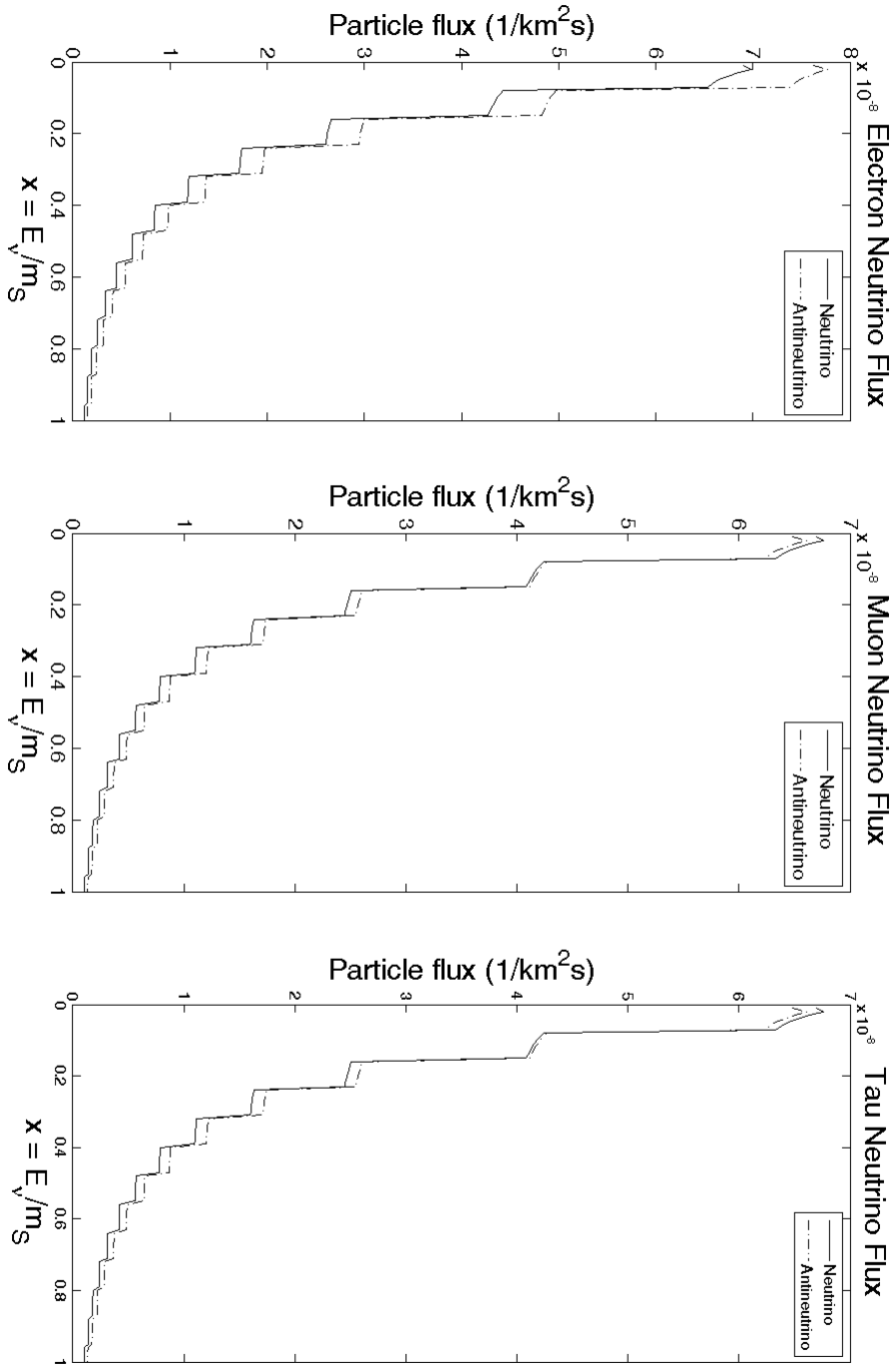

Figure 6.13: Local Neutrino Flux ($m_S = 500$ GeV)

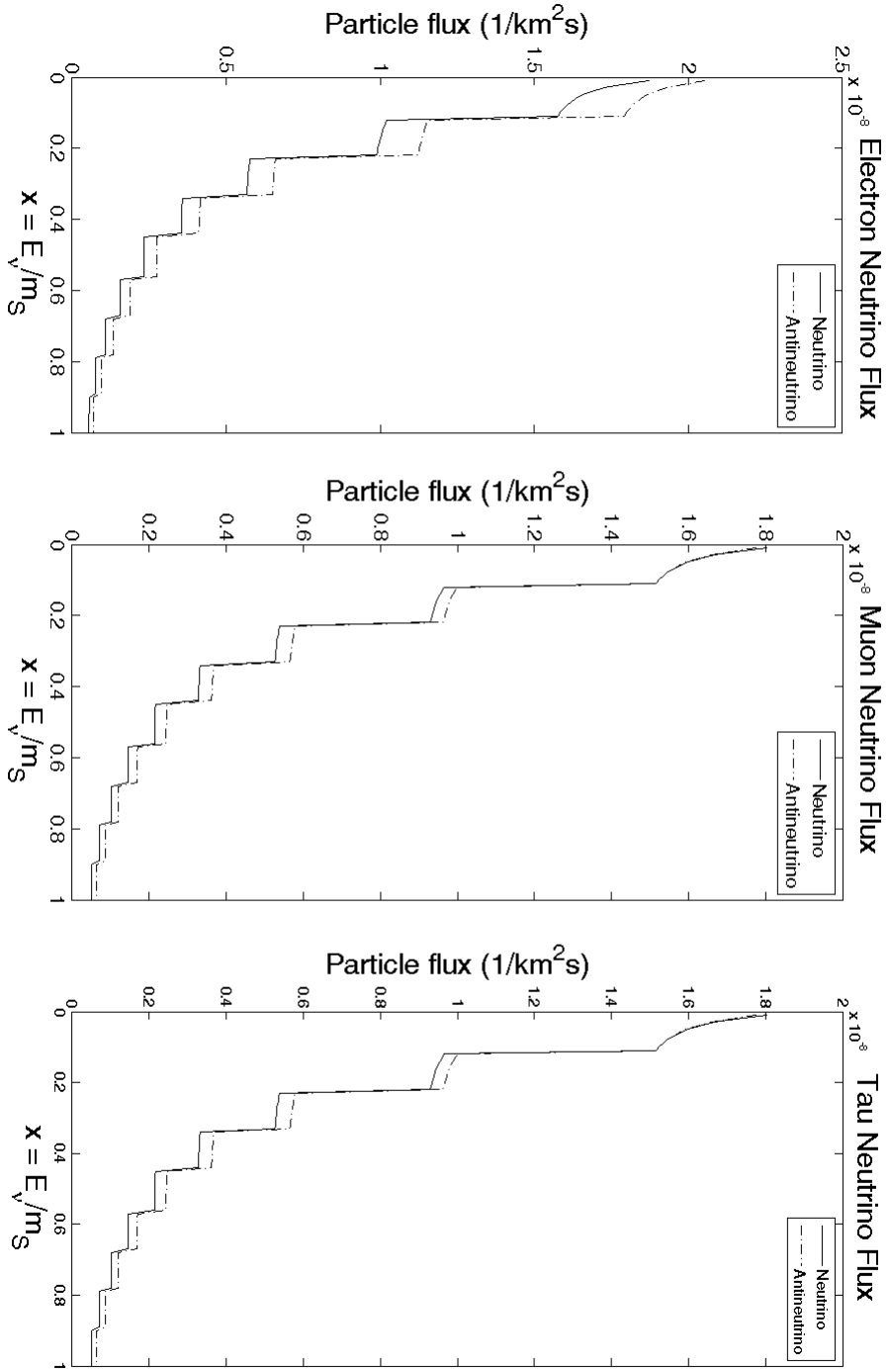

Figure 6.14: Local Neutrino Flux ($m_S = 700$ GeV)

Chapter 7

Collider Signals of Singlets

This chapter deals with the production of singlets in particle colliders, with calculations done for the case of the LHC at CERN. In general, collider production is the most difficult way to search for dark matter, simply because there are so many things happening at once. If searching for dark matter was the only reason to run the LHC, it would never have been built. Luckily, particle colliders can provide information about nearly all aspects of particle physics.

Dark matter, being essentially invisible, is difficult to see in the detection chambers at colliders. One would have to look for missing energy, decay products, or some kind of bremsstrahlung. To use these effects to produce any kind of meaningful signal requires an intimate understanding of the processes that are happening. In the energy ranges that are currently being investigated, we lack this understanding. There is no clear picture of what would happen in the absence of dark matter, so trying to extract a positive signal is nearly futile. At best, we can use collider results as bounds on what is possible for a dark matter candidate.

The scalar singlets that we consider have masses in the 100-1500 GeV range, so to produce a pair at the upper limits of the mass range a collider needs to be working at 3000 GeV or more. They also couple to $\mathcal{SM}$ matter only through the Higgs portal, indicating that for singlets to be produced, a Higgs boson must also be producable. These two requirements make it obvious that the experiment we should focus on is the LHC. While other experiments, like the Tevatron, may cover some of the required energy range, only the LHC will cover all of it. The LHC also has the best chance of producing a Higgs signal.

7.1 Higgs Boson Production at the LHC

The LHC is a particle collider that is capable of reaching energies never before artificially produced. It is a device that accelerates and collides opposing beams of protons or lead ions at full power center of mass energies of 14 TeV. In reaching these energies, it is hoped that phenomena such as the Higgs boson or signs of SUSY will be revealed.

The beams travel in a circular path guided by superconducting magnets, where each beam is composed of a few thousand bunches of around a hundred billion protons at full intensity. The protons themselves are ultrarelativistic, with a γ value of around 7500 at full power. The beams are collided in one of four detectors arranged around the accelerator ring. The relevant detectors for dark matter searches are ATLAS and CMS,

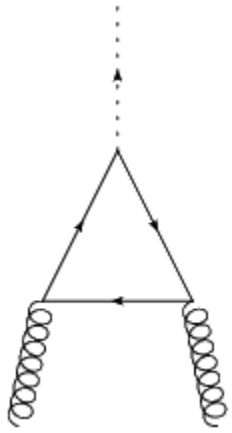

Figure 7.1: Basic Gluon Fusion

which are the beyond the $\mathcal{SM}$ detectors examining the products of the proton collision for any sign of the Higgs or SUSY.

The most important characteristic of the scalar singlet is that it couples to $\mathcal{SM}$ matter only through the Higgs portal. Any detection of singlets will be through Higgs mediation, and so paying attention to mechanisms that are capable of producing a Higgs boson is important.

According to the $\mathcal{SM}$, Higgs bosons are produced in small quantities in any interaction with sufficient energy. They decay quickly, of course. The problem with looking for the Higgs when colliding stable particles, which is what we are required to do, is that stable particles tend to be the lightest of their families, with small masses. Light particles have a correspondingly weak interaction with the Higgs, and so Higgs production rates are very low. In higher energy collisions, virtual particles with high mass may be produced. The appearance of these particles may be a loop level effect, but that supression can be more than counteracted by the much greater strength of their coupling to the Higgs. This is the usual means of Higgs boson production.

In the LHC, protons are the particles being collided. The dominant methods of Higgs production for proton collision have been known for some time [60]. We consider only the most dominant contribution, as it accounts for the vast majority of Higgs production in the Higgs mass range that is currently favored by experiment. A full analysis of the expected cross sections for various mechanisms of Higgs boson production has been released by the LHC Higgs Cross Section Working Group [48].

The primary mechanism is that of gluon fusion, the means by which 80% or more of Higgs bosons are produced in high energy pp collisions. It is a loop order effect; what happens is that two gluons, one from each proton, couple to a quark loop which is coupled to an external Higgs. Technically, all flavors of quark loop contribute, but due to the mass scale of the quarks, all terms but the top quark term are negligible. The basic diagram for the process is shown in Figure 7.1.

The process of gluon fusion has been calculated up to NNLO in perturbation theory [45]. This degree of accuracy is unnecessary for our purposes, which are exploratory in nature, but we note that NLO (and NNLO)

QCD corrections to this process are certainly significant. NLO QCD corrections lead to modification of the LO cross section by nearly 100% [113] [66], and NNLO corrections bring the ratio up to $\sigma_{NNLO}/\sigma_{LO} \simeq 2.5$ [69] [28] [70]. Additional soft gluon structure can alter the final result by over 10%. If one were to proceed with precision calculations of dark matter production through the Higgs in high energy interactions at particle colliders, one would need to perform calculations to that level, which involves 4-loop processes. Judicious use of effective Higgs-gluon couplings can reduce that number by one for many classes of diagram, but the procedure remains incredibly time consuming. Such calculations are usually done in the heavy top quark limit, in which the mass of the top quark has been taken to be infinite. This approximation is accurate to within a few per cent. The calculations have not been pushed to any higher order in the perurbation theory, so the effects that further QCD corrections will have are unknown. There are also electroweak corrections, which have been calculated up to NLO [49] [4], which contribute at the per cent level for $m_h = 125$ GeV. These corrections are often neglected, as it is unclear how to apply them in concert with the QCD corrections.

While the basic Higgs production cross section from free gluon fusion is well understood, the situation that occurs in particle colliders is rather more complicated. The gluons being fused are not free, but are parts of protons, and the protons are the particles being collided. The usual way of resolving situations like these is to treat the gluon as a component of the proton, carrying a certain proportion of its momentum, called a parton. The momentum distribution of the proton among its partons can be described by a phenomological object known as the parton distribution function. One can then compute the cross section for the free gluon fusion process and then take the partonic nature of the gluons into account by integrating the free cross section over the parton distribution functions. The full treatment of the gluon fusion mechanism requires inclusion of the gluon distribution functions.

After the Higgs boson is produced, it decays quite rapidly, and its decay products are analyzed in the detectors, along with the decay products of the many other particles that were produced in the collision. The main signal of the Higgs is a pair of photons, which unfortunately has a tendency to get lost in the large photon backgrounds. This is made more complicated since the Higgs mass is not known. The Higgs does usually appear with a pair of hadronic jets, formed by the remnants of the collided protons, and these give us some idea of what energy range the photon signal might be in. There are other signals, but they are even harder to catch than the photons, as well as being less prevalent in the experimentally favored Higgs mass range.

7.2 Singlet Production at the LHC

The previous section discussed Higgs boson production in proton colliders like the LHC. This thesis is only concerned with Higgs production insomuch as it leads to singlet production. The gluon fusion mechanism for Higgs production from the previous section can be modified for use in describing singlet production. This simply involves coupling the final state Higgs to a pair of singlets. The modified diagram is found in Figure

Figure 7.2: Singlet Production via Gluon Fusion

7.2.

Since the addition of the singlet vertex scales both processes by the same amount, the proportions which they contribute to the overall singlet production cross section remain the same as those for Higgs production. In the end, the singlet production cross section is just some fraction of the Higgs production cross section. The full calculation of the singlet production via gluon fusion cross section is deferred to the Appendix.

We use in these calculations the basic gluon distribution function, with $\alpha = \beta = \gamma = \delta = 1$,

$$f_g(x) = \frac{5}{2}\frac{\alpha(1-x)^{4+\gamma}}{\beta x^{\delta}}$$

This function is a basic parameterization that can be modified to better fit with experimental data by changing the values of the parameters. The version with all parameters equal to one is a simple approximation that serves our purposes. To get the best accuracy possible, one would leave parameterizations behind and use the fully numerical gluon distribution functions put out by CTEQ [85], or some other collaboration.

The final cross section for singlet production via gluon fusion is

$$\sigma_{gg\to SS} = \frac{\alpha_s^2\eta^2 m_t^4}{3^2 2^{11}\pi^7 k_p^4}\int\limits_{m_S^2/k_p^2}^{1} dx_1 \int\limits_{m_S^2/(k_p^2 x_1)}^{1} dx_2 \frac{25}{4}\frac{(1-x_1)^4(1-x_2)^4}{x_1^4 x_2^4}\frac{1}{\left(4x_1x_2k_p^2 - m_h^2\right) + m_h^2\Gamma_h^2}$$

$$\times I_2^2(x_1,x_2)\int\limits_{L_1}^{L_2} dp_{1\|}\frac{(x_1+x_2)\sqrt{4x_1x_2\left(x_1k_p - p_{1\|}\right)\left(x_2k_p + p_{1\|}\right) - m_S^2\left(x_1+x_2\right)^2}}{\left[2x_1x_2k_p + (x_1-x_2)\,p_{1\|}\right]\left|(x_1^2+x_2^2)\,k_p - (x_1-x_2)\,p_{1\|}\right|}$$

where the limits on the $p_{1\|}$integral are

$$L_1 = \frac{x_1-x_2}{2}k_p - \frac{x_1+x_2}{2}\sqrt{k_p^2 - \frac{m_S^2}{x_1x_2}}$$

$$L_2 = \frac{x_1 - x_2}{2} k_p + \frac{x_1 + x_2}{2} \sqrt{k_p^2 - \frac{m_S^2}{x_1 x_2}}$$

and the internal integral $I_2(x_1, x_2)$, which is fully evaluated in the Appendix, is given by

$$I_2 = -8i\pi^2 m_t \epsilon_\mu(\mathbf{k}_1, s_1)\epsilon_\nu(\mathbf{k}_2, s_2) \left[\frac{2m_t^2 + k_1 \cdot k_2}{a m_t^2} - 2\left[\arcsin\left(\sqrt{\frac{a}{4}} \right) \right]^2 - \frac{1}{2} \right] \quad for \quad 0 < a < 4$$

or

$$I_2 = -8i\pi^2 m_t \epsilon_\mu(\mathbf{k}_1, s_1)\epsilon_\nu(\mathbf{k}_2, s_2)$$

$$\times \left[\frac{2m_t^2 + k_1 \cdot k_2}{a m_t^2} \left\{ \frac{1}{2} \left[\ln\left(\frac{\sqrt{a} + \sqrt{a-4}}{\sqrt{a} - \sqrt{a-4}} \right) \right]^2 - \frac{\pi^2}{2} - i\pi \ln\left(\frac{\sqrt{a} + \sqrt{a-4}}{\sqrt{a} - \sqrt{a-4}} \right) \right\} - \frac{1}{2} \right] \quad for \quad a > 4$$

where $a = 4x_1 x_2 \mathbf{k}^2 / m_t^2$.

This expression cannot be integrated analytically, but can be done so numerically. To avoid the expense of computing the $p_{1\parallel}$ integral, we have instead presented the differential cross section $\frac{d\sigma}{dp_{1\parallel}}$. The integration has been performed using a standard adaptive quadrature method with an adaptive tolerance set to 10^{-5}. The specific software package used was MATLAB® (2008b, The MathWorks, Natick, MA, USA). The double integral over the gluon distribution parameters x_1 and x_2 was performed for values of $p_{1\parallel}$ in the range of momenta allowed by the kinematics of the problem. The accuracy of the computation is somewhat limited by the singularity induced by the presence of the coefficient function

$$C(x_1, x_2) = \frac{25}{4} \frac{(1 - x_1)^4 (1 - x_2)^4}{x_1^4 x_2^4}$$

Though the point $x_1 = x_2 = 0$ is disallowed kinematically, ensuring that the integral does exist, the singularity exerts enough of an influence on the rest of the integration region that the integration package with default tolerance levels could not evaluate the integral. Reducing the sensitivity of the quadrature package allowed the evaluation to be completed.

7.3 Results and Discussion

We present the differential cross sections $\frac{d\sigma}{dp_{1\parallel}}$ for singlet mass values of $m_S = 300$ GeV, 500 GeV, 800 GeV, 1000 GeV, and 1500 GeV in Figures 7.3 - 7.7 The cross sections are plotted in both cm^3/s and under a base 10 logarithm to show their full structure. We note that the differential cross sections reported here do not include the above integration limits L_1 and L_2. The differential cross sections are functions of $p_\parallel$, and they are cumulative functions, in a sense. The value of the differential cross section at $p_\parallel = z$ is the cross section for producing singlets with parallel momentum less than $p_\parallel = z$.

To illustrate the effects of η on these results we plot in Figure 7.8 the base 10 logarithm of the differential cross section at $m_S = 300$ GeV for $\eta = 0.1$ and $\eta = 0.3$. There is nothing surprising, simply the expected scaling of the cross section by η^2, which will be independent of singlet mass.

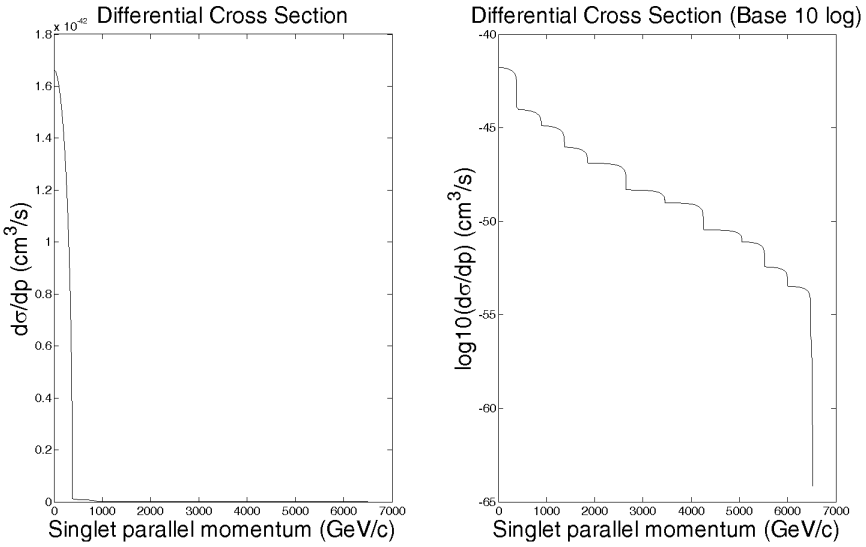

Figure 7.3: Differential Singlet Production Cross Section ($m_S = 300$ GeV)

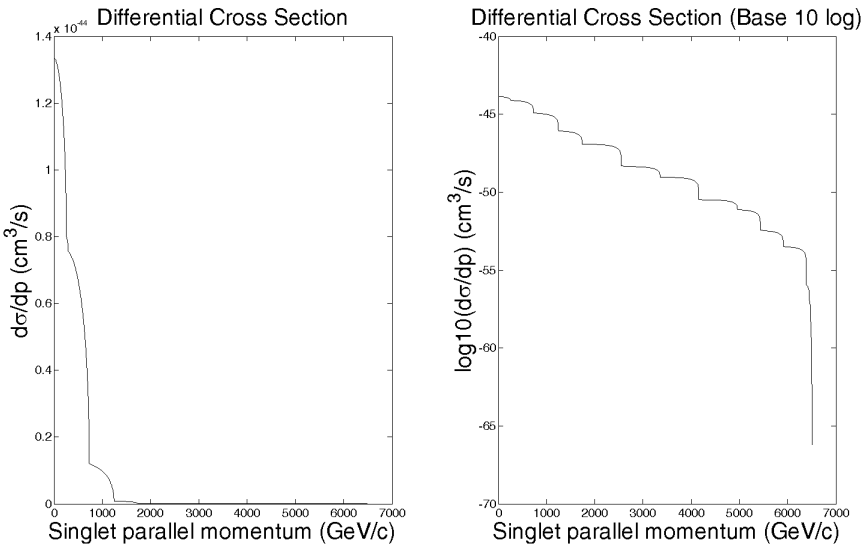

Figure 7.4: Differential Singlet Production Cross Section ($m_S = 500$ GeV)

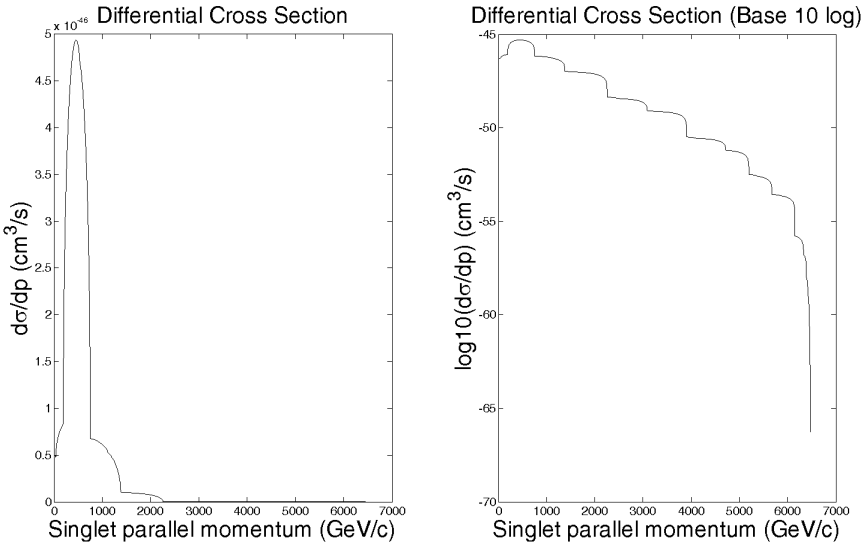

Figure 7.5: Differential Singlet Production Cross Section ($m_S = 800$ GeV)

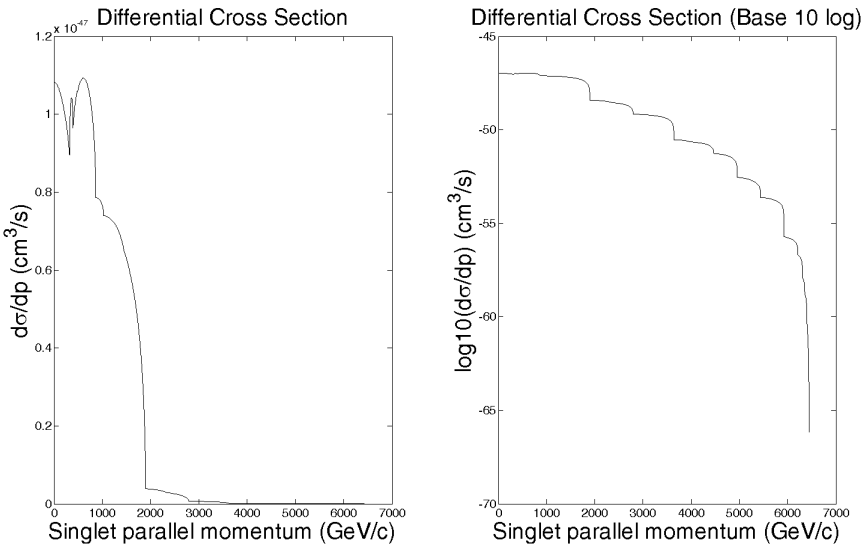

Figure 7.6: Differential Singlet Production Cross Section ($m_S = 1000$ GeV)

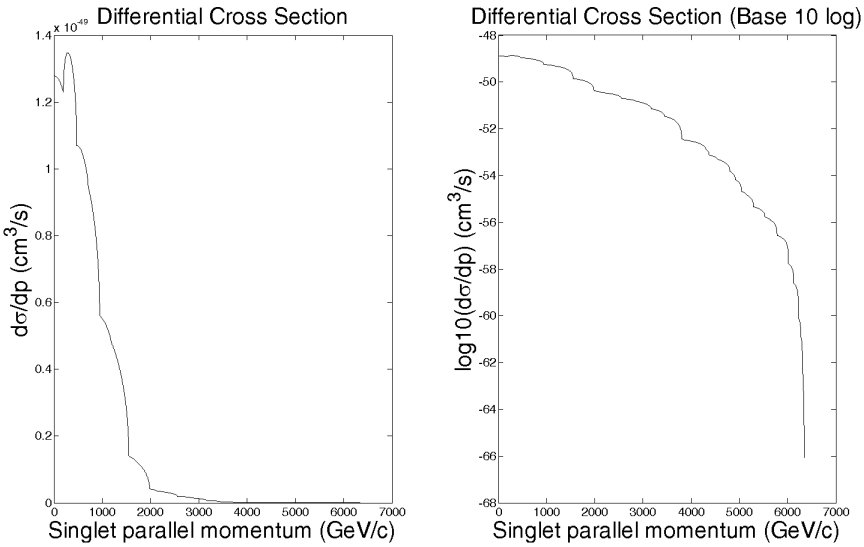

Figure 7.7: Differential Singlet Production Cross Section ($m_S = 1500$ GeV)

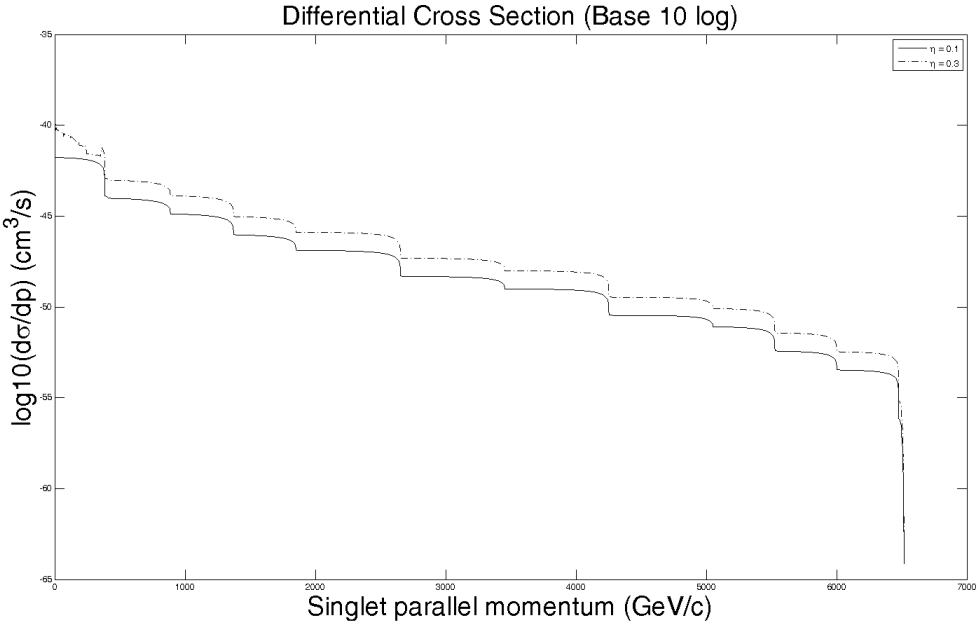

Figure 7.8: Dependence of Differential Cross Section on η ($m_S = 300$ GeV)

m_S	$\widetilde{\sigma}_{gg\to SS}$ (cm^2)	$\widetilde{\sigma}_{gg\to SS}/\sigma^{dFG}_{gg\to hh}$	$\widetilde{\sigma}_{gg\to SS}/\sigma^{ABPS}_{gg\to hh}$
300 GeV	5.0489×10^{-37}	0.0101	0.0098
500 GeV	6.0646×10^{-39}	0.1214×10^{-3}	0.1178×10^{-3}
800 GeV	2.2976×10^{-40}	0.4598×10^{-5}	0.4464×10^{-5}
1000 GeV	1.5693×10^{-41}	0.3140×10^{-6}	0.3049×10^{-6}
1500 GeV	1.3917×10^{-43}	0.2785×10^{-8}	0.2704×10^{-8}

Table 7.1: Comparison to Gluon Fusion Higgs Production Cross Sections

The momentum step size in these plots is 1 GeV, so the value of 7000 indicates a singlet has absorbed the whole 7 TeV of energy carried by the proton. Since both of the produced singlets must have the same parellel momentum component, because of conservation of momentum, the 7 TeV singlets can only come into existence if a pair of gluons, each containing all of the energy of their respective protons, manage to fuse. Looking at the approximate gluon distribution function we use for calculations we can see that even with the high x weighting that the function has, this does not occur very often. This explains why the differential cross sections indicate that essentially no singlets are produced with a $p_{\|}$ value of more than 4 TeV, and why very few are produced with more than 2.5 TeV. This is somewhat dependant on the singlet mass, of course.

The higher mass singlets reach higher momenta somewhat more easily than the lighter mass singlets, since absorbing the same amount of energy from a proton as a lighter singlet will furnish them with more momentum, simply by virtue of their higher mass. Of course, there is a lower limit on the maximum final momentum of the heavier singlets than there is on the lighter ones, as more of the initial energy of the proton is used to create them, again by virtue of their higher mass. This also explains why, as the singlet mass increases, the size of the differential cross section decreases by whole orders of magnitude, from 10^{-42} cm^3/s at $m_S = 300$ GeV to 10^{-49} cm^3/s at $m_S = 1500$ GeV.

We now consider how the production of singlets at the LHC might affect the Higgs boson signal observed there. To make a simple comparison to the full results for the Higgs boson production cross section by gluon fusion as reported by the LHC Higgs Cross Section Working Group [48], we employ a simple trapezoidal numerical integration routine to obtain an estimate ($\widetilde{\sigma}_{gg\to SS}$) of the total cross sections by singlet mass from the differential cross sections. We then compare these estimates to the Higgs production cross sections reported in the above reference. The comparisons are presented in Table 7.1. The last two columns are ratios of our estimated cross section to the calculated Higgs production cross section, where $\sigma^{dFG}_{gg\to hh} = 49.97$ pb ($\times10^{-36}cm^2/pb$) for $m_h = 125$ GeV and $\sigma^{ABPS}_{gg\to hh} = 51.47$ pb ($\times10^{-36}cm^2/pb$) for $m_h = 125$ GeV. The superscripts indicate the distribution function model used for the calculation, as described in the reference.

These comparisons indicate that any missing energy signal should be easier to extract for lower mass singlets. At the higher masses, the singlet production cross sections are so low that they would be absorbed

by the experimental background. Only the per cent level results from a singlet mass of 300 GeV or less are likely to be observable. It should be noted that we have not included in our singlet production calculations any QCD or electroweak corrections, which the unmodified gluon fusion process lead us to believe will be significant. Assuming a similar enhancment factor of $\sim$2.5, this would extend the mass range for a detectable singlet up to near 500 GeV. Of course, all of these results must wait for testing until the LHC is running at its full power of 14 TeV, which is not scheduled to happen until 2014.

Chapter 8

Conclusions

In this chapter we will briefly summarize the results obtained throughout the thesis.

The direct detection signal has proven the most promising. As was detailed in Chapter 3, the singlet nuclear recoil cross section in the low mass range from 15 to 55 GeV is consistent with the experimental results reported by the CRESST collaboration in that region. The comparison, with $\eta = 0.3$, is displayed in Figure 3.X, and this basic comparison is still at the edge of the 1σ region of significance. A slight adjustment of η would allow for an exact fit to the observed events, and such values of η are allowed by thermal relic density requirements. We do not comment at this time on the obvious contradiction between the XENON and CRESST results. It is beyond the scope of this thesis to go into a detailed analysis of the event recognition processes used by these experiments.

The indirect detection signals in general were lost in the observed astrophysical background. For the gamma ray case, the calculated signal is on the order of a few per cent of the background. This makes observational confirmation of any signal of singlet annihilations in the diffuse flux very difficult. The antimatter case is similiar, with the calculated particle fluxes at Earth being much smaller than the observed fluxes. The improved sensitivity of the AMS-02 antimatter telescope may change this. In the case of neutrinos, no excess neutrinos from the Sun have been observed, so there is no observational evidence for an exotic neutrino signal. The calculated neutrino fluxes are quite small as well.

The collider production cross section for singlets gives results that are at the per cent level when compared to Higgs boson production cross sections. Not enough data exists to test the validity of the these predictions, and will not for several years. Once the LHC resumes operations at full power these cross sections can be compared to experiment.

Further work can be done on the project in several areas. In particular, the gamma ray signal can be improved upon by taking into account substructure and conisdering the annihilation signals of higher density extragalactic objects. The neutrino signal can be improved as well, by considering neutrinos from singlet capture in the Earth or Jupiter as well as the Sun. Also, the neutrino flux can be used to place bounds on the nuclear recoil cross section, although that is more relevant for spin dependent interactions. Of course, all calculated signals can be improved by using next generation data sets and future astrophysical results.

According to the CRESST results, the scalar singlet model is favored. Most of the other direct detection experimental results exclude the scalar singlet model as a possible dark matter candidate. The indirect

signals are inconclusive, as is the collider signal for different reasons.

References

[1] C. E. Aalseth, P. S. Barbeau, N. S. Bowden, B. Cabrera-Palmer, J. Colaresi, J. I. Collar, S. Dazeley, P. de Lurgio, J. E. Fast, N. Fields, C. H. Greenberg, T. W. Hossbach, M. E. Keillor, J. D. Kephart, M. G. Marino, H. S. Miley, M. L. Miller, J. L. Orrell, D. C. Radford, D. Reyna, O. Tench, T. D. Van Wechel, J. F. Wilkerson, and K. M. Yocum. Results from a search for light-mass dark matter with a p-type point contact germanium detector. *Physical Review Letters*, 106:131301, Mar 2011.

[2] C. E. Aalseth, P. S. Barbeau, J. Colaresi, J. I. Collar, J. Diaz Leon, J. E. Fast, N. Fields, T. W. Hossbach, M. E. Keillor, J. D. Kephart, A. Knecht, M. G. Marino, H. S. Miley, M. L. Miller, J. L. Orrell, D. C. Radford, J. F. Wilkerson, and K. M. Yocum. Search for an annual modulation in a p-type point contact germanium dark matter detector. *Physical Review Letters*, 107:141301, Sep 2011.

[3] O. Adriani et al. PAMELA results on the cosmic-ray antiproton flux from 60 MeV to 180 GeV in kinetic energy. *Physical Review Letters*, 105:121101, 2010.

[4] U. Aglietti, R. Bonciani, G. Degrassi, and A. Vicini. Two loop light fermion contribution to Higgs production and decays. *Physics Letters*, B595:432–441, 2004.

[5] Z. Ahmed et al. Dark Matter Search Results from the CDMS II Experiment. *Science*, 327:1619–1621, 2010.

[6] Sarah Andreas, Chiara Arina, Thomas Hambye, Fu-Sin Ling, and Michel H.G. Tytgat. A light scalar WIMP through the Higgs portal and CoGeNT. *Physical Review*, D82:043522, 2010.

[7] G. Angloher, M. Bauer, I. Bavykina, A. Bento, A. Brown, C. Bucci, C. Ciemniak, C. Coppi, G. Deuter, F. von Feilitzsch, D. Hauff, S. Henry, P. Huff, J. Imber, S. Ingleby, C. Isaila, J. Jochum, M. Kiefer, M. Kimmerle, H. Kraus, J.-C. Lanfranchi, R.F. Lang, B. Majorovits, M. Malek, R. McGowan, V.B. Mikhailik, E. Pantic, F. Petricca, S. Pfister, W. Potzel, F. Prbst, W. Rau, S. Roth, K. Rottler, C. Sailer, K. Schffner, J. Schmaler, S. Scholl, W. Seidel, L. Stodolsky, A.J.B. Tolhurst, I. Usherov, and W. Westphal. Commissioning run of the CRESST-II dark matter search. *Astroparticle Physics*, 31(4):270 – 276, 2009.

[8] G. Angloher, M. Bauer, I. Bavykina, A. Bento, C. Bucci, et al. Results from 730 kg days of the CRESST-II Dark Matter Search arXiv:1109.0702. 2011.

[9] E. Aprile, K. Arisaka, F. Arneodo, A. Askin, L. Baudis, A. Behrens, E. Brown, J.M.R. Cardoso, B. Choi, D. Cline, S. Fattori, A.D. Ferella, K.L. Giboni, A. Kish, C.W. Lam, R.F. Lang, K.E. Lim, J.A.M. Lopes, T. Marrodn Undagoitia, Y. Mei, A.J. Melgarejo Fernandez, K. Ni, U. Oberlack, S.E.A. Orrigo, E. Pantic, G. Plante, A.C.C. Ribeiro, R. Santorelli, J.M.F. dos Santos, M. Schumann, P. Shagin, A. Teymourian, E. Tziaferi, H. Wang, and M. Yamashita. The XENON100 dark matter experiment. *Astroparticle Physics*, 35(9):573 – 590, 2012.

[10] E. Aprile and T. Doke. Liquid xenon detectors for particle physics and astrophysics. *Reviews of Modern Physics*, 82:2053–2097, Jul 2010.

[11] John Bahcall. *Dark Matter In The Universe*. World Scientific, 2004.

[12] Vernon Barger, Paul Langacker, Mathew McCaskey, Michael J. Ramsey-Musolf, and Gabe Shaughnessy. Cern lhc phenomenology of an extended standard model with a real scalar singlet. *Physical Review*, D77:035005, Feb 2008.

[13] Roberto Battiston. The antimatter spectrometer (AMS-02): A particle physics detector in space. *Nuclear Instruments and Methods in Physics Research Section A: Accelerators, Spectrometers, Detectors and Associated Equipment*, 588:227 – 234, 2008. Proceedings of the First International Conference on Astroparticle Physics.

[14] Laura Baudis. DARWIN: dark matter WIMP search with noble liquids. 2012.

[15] K. G. Begeman, A. H. Broeils, and R. H. Sanders. Extended rotation curves of spiral galaxies - Dark haloes and modified dynamics. *Monthly Notices of the Royal Astronomical Society*, 249:523–537, April 1991.

[16] Jacob D. Bekenstein. Relativistic MOND as an alternative to the dark matter paradigm. *Nuclear Physics*, A827:555C–560C, 2009.

[17] M. C. Bento, O. Bertolami, R. Rosenfeld, and L. Teodoro. Self-interacting dark matter and the higgs boson. *Physical Review*, D62:041302, Jul 2000.

[18] Lars Bergström, Joakim Edsjö, and Piero Ullio. Cosmic anti-protons as a probe for supersymmetric dark matter? *The Astrophysical Journal*, 526:215–235, 1999.

[19] Lars Bergström, Joakim Edsjö, and Piero Ullio. Spectral gamma-ray signatures of cosmological dark matter annihilations. *Physical Review Letters*, 87:251301, Nov 2001.

[20] R. Bernabei, Pierluigi Belli, F. Cappella, R. Cerulli, F. Montecchia, et al. Dark matter search. *La Rivista del Nuovo Cimento*, 26N1:1–73, 2003.

[21] O. Bertolami and R. Rosenfeld. THE HIGGS PORTAL AND AN UNIFIED MODEL FOR DARK ENERGY AND DARK MATTER. *International Journal of Modern Physics*, A23(30):4817–4827, 2008.

[22] Gianfranceo Bertone. *Particle Dark Matter*. Cambridge, 2010.

[23] Gianfranco Bertone, Dan Hooper, and Joseph Silk. Particle dark matter: Evidence, candidates and constraints. *Physics Reptorts*, 405:279–390, 2005.

[24] Andreas Birkedal, Andrew Noble, Maxim Perelstein, and Andrew Spray. Little Higgs dark matter. *Physical Review*, D74:035002, 2006. 22 pages, 9 figures. v3: a typo in Eq. (7) corrected. The rest of the paper is completely unaffected.

[25] N. W. Boggess, J. C. Mather, R. Weiss, C. L. Bennett, E. S. Cheng, E. Dwek, S. Gulkis, M. G. Hauser, M. A. Janssen, T. Kelsall, S. S. Meyer, S. H. Moseley, T. L. Murdock, R. A. Shafer, R. F. Silverberg, G. F. Smoot, D. T. Wilkinson, and E. L. Wright. The COBE mission - Its design and performance two years after launch. *The Astrophysical Journal*, 397:420–429, October 1992.

[26] Cliff Burgess, Maxim Pospelov, and Tonnis ter Veldhuis. The Minimal Model of nonbaryonic dark matter: a singlet scalar. *Nuclear Physics*, B619:709–728, 2001.

[27] S. T. Butler and C. A. Pearson. Deuterons from high-energy proton bombardment of matter. *Physical Review*, 129:836–842, Jan 1963.

[28] Stefano Catani, Daniel de Florian, and Massimiliano Grazzini. Higgs production in hadron collisions: Soft and virtual QCD corrections at NNLO. *Journal of High Energy Physics*, 0105:025, 2001.

[29] Serguei Chatrchyan et al. Combined results of searches for the standard model Higgs boson in pp collisions at sqrt(s) = 7 TeV arXiv:1202.1488. 2012.

[30] T. P. Cheng. Chiral symmetry and the higgs-boson nucleon coupling. *Physical Review*, D38:2869–2874, Nov 1988.

[31] Marco Cirelli, Gennaro Corcella, Andi Hektor, Gert Hutsi, Mario Kadastik, et al. PPPC 4 DM ID: A Poor Particle Physicist Cookbook for Dark Matter Indirect Detection. *Journal of Cosmology and Astroparticle Physics*, 1103:051, 2011. 57 pages with many figures and tables. v2: several discussions and references added, some figures improved, matches version published on JCAP. v3: a few typos corrected and some references updated. All results are available at http://www.marcocirelli.net/PPPC4DMID.html.

[32] Marco Cirelli, Nicolao Fornengo, Teresa Montaruli, Igor Sokalski, Alessandro Strumia, and Francesco Vissani. Spectra of neutrinos from dark matter annihilations. *Nuclear Physics*, B727:99 – 138, 2005.

[33] Douglas Clowe, Marusa Bradac, Anthony H. Gonzalez, Maxim Markevitch, Scott W. Randall, et al. A direct empirical proof of the existence of dark matter. *The Astrophysical Journal*, 648:L109–L113, 2006.

[34] PAMELA collaboration. Pamela: A payload for antimatter matter exploration and light-nuclei astrophysics - status and first results. In *Nuclear Science Symposium Conference Record, 2007. NSS '07. IEEE*, volume 1, pages 42 –47, 2007.

[35] PDG collaboration. Review of Particle Physics. *Journal of Physics G*, 33:1+, 2006.

[36] Super-Kamiokande collaboration. The Super-Kamiokande detector. *Nuclear Instruments and Methods in Physics Research Section A: Accelerators, Spectrometers, Detectors and Associated Equipment*, 501:418 – 462, 2003.

[37] The XENON100 Collaboration. Reply to the Comments on the XENON100 First Dark Matter Results arXiv:1005.2615. 2010.

[38] J.I. Collar and D.N. McKinsey. Comments on 'First Dark Matter Results from the XENON100 Experiment' arXiv:1005.0838. 2010.

[39] J.I. Collar and D.N. McKinsey. Response to arXiv:1005.2615, arXiv:1005.3723. 2010.

[40] Fred I. Cooperstock and S. Tieu. General relativity resolves galactic rotation without exotic dark matter. *The Astrophysical Journal*, 2005.

[41] Yanou Cui, John D. Mason, and Lisa Randall. General Analysis of Antideuteron Searches for Dark Matter. *Journal of High Energy Physics*, 1011:017, 2010.

[42] G. Cynolter, E. Lendvai, and G. Pocsik. Note on unitarity constraints in a model for a singlet scalar dark matter candidate. *Acta Physica Polonica*, B36:827–832, 2005. 6 pages, 4 eps figures Report-no: ITP-Budapest 614.

[43] Hooman Davoudiasl, Ryuichiro Kitano, Tianjun Li, and Hitoshi Murayama. The new Minimal Standard Model. *Physics Letters*, B609:117 – 123, 2005.

[44] A. Davour and Picasso Collaboration. The PICASSO Dark Matter Search Project. In *Identification of Dark Matter 2008*, 2008.

[45] Daniel de Florian and Massimiliano Grazzini. Higgs production through gluon fusion: Updated cross sections at the Tevatron and the LHC. *Physics Letters*, B674:291–294, 2009.

[46] Rainer Dick, Robert Mann, and Kai Wunderle. Cosmic rays through the Higgs portal. *Nuclear Physics*, B805:207–230, 2008.

[47] Rainer Dick and Frederick Sage. A minimal dark matter interpretation for the CRESST-II signal. *European Journal of Physics C*, To appear 2012.

[48] S. Dittmaier et al. Handbook of LHC Higgs Cross Sections: 1. Inclusive Observables. 2011. Long author list - awaiting processing.

[49] A. Djouadi and P. Gambino. Leading electroweak correction to Higgs boson production at proton colliders. *Physical Review Letters*, 73:2528–2531, 1994.

[50] F. Donato, Nicolao Fornengo, D. Maurin, and P. Salati. Antiprotons in cosmic rays from neutralino annihilation. *Physical Review*, D69:063501, 2004.

[51] J. Einasto. Influence of the atmospheric and instrumental dispersion on the brightness distribution in a galaxy. *Trudy Inst. Astrofiz. Alma-Ata*, 1965.

[52] M.M. Ettefaghi and M. Dehghani. The Decay of singlet scalar dark matter to unparticle and photon arXiv:0805.0682. 2008.

[53] Marco Farina, Mario Kadastik, Duccio Pappadopulo, Joosep Pata, Martti Raidal, and Alessandro Strumia. Implications of Xenon100 and LHC results for Dark Matter models. *Nuclear Physics*, B853(3):607 – 624, 2011.

[54] Marco Farina, Duccio Pappadopulo, and Alessandro Strumia. CDMS stands for Constrained Dark Matter Singlet. *Physics Letters*, B688:329–331, 2010.

[55] Jonathan L. Feng, Jason Kumar, Danny Marfatia, and David Sanford. Isospin-violating dark matter. *Physics Letters*, B703(2):124 – 127, 2011.

[56] Fermi-LAT Collaboration. Spectrum of the Isotropic Diffuse Gamma-Ray Emission Derived from First-Year Fermi Large Area Telescope Data. *Physical Review Letters*, 104(10):101101, March 2010.

[57] R. Foot. Mirror dark matter. *International Journal of Modern Physics*, A22:4951–4957, 2007.

[58] Paul H. Frampton. Black Holes as Dark Matter. *AIP Conference Proceedings*, 1232:53–57, 2010.

[59] RJ Gaitskell. Direct detection of dark matter. *ANNUAL REVIEW OF NUCLEAR AND PARTICLE SCIENCE*, 54:315–359, 2004.

[60] H. M. Georgi, S. L. Glashow, M. E. Machacek, and D. V. Nanopoulos. Higgs bosons from two-gluon annihilation in proton-proton collisions. *Physical Review Letters*, 40:692–694, Mar 1978.

[61] Matthew Gonderinger, Yingchuan Li, Hiren Patel, and Michael Ramsey-Musolf. Vacuum stability, perturbativity, and scalar singlet dark matter. *Journal of High Energy Physics*, 2010, 2010.

[62] P Gondolo, J Edsjö, P Ullio, L Bergström, M Schelke, and E A Baltz. Darksusy: computing supersymmetric dark matter properties numerically. *Journal of Cosmology and Astroparticle Physics*, 2004(07):008, 2004.

[63] A. Goudelis, Y. Mambrini, and C. Yaguna. Antimatter signals of singlet scalar dark matter. *Journal of Cosmology and Astroparticle Physics*, 2009(12):008, 2009.

[64] A. Gould. Resonant enhancements in weakly interacting massive particle capture by the earth. *The Astrophysical Journal*, 321:571–585, October 1987.

[65] A. Gould. Cosmological density of WIMPs from solar and terrestrial annihilations. *The Astrophysical Journal*, 388:338–344, April 1992.

[66] D. Graudenz, M. Spira, and P. M. Zerwas. Qcd corrections to higgs-boson production at proton-proton colliders. *Physical Review Letters*, 70:1372–1375, Mar 1993.

[67] Wan-Lei Guo and Yue-Liang Wu. The real singlet scalar dark matter model. *Journal of High Energy Physics*, 2010, 2010.

[68] Francis Halzen and Spencer R. Klein. IceCube: An Instrument for Neutrino Astronomy. *Review of Scientific Instruments*, 81:081101, 2010.

[69] Robert V. Harlander. Virtual corrections to g g to gt; H to two loops in the heavy top limit. *Physics Letters*, B492:74–80, 2000.

[70] Robert V. Harlander and William B. Kilgore. Next-to-next-to-leading order Higgs production at hadron colliders. *Physical Review Letters*, 88:201801, 2002.

[71] Xiao-Gang He, Shu-Yu Ho, Jusak Tandean, and Ho-Chin Tsai. Scalar Dark Matter and Standard Model with Four Generations. *Physical Review*, D82:035016, 2010.

[72] Xiao-Gang He, Tong Li, Xue-Qian Li, Jusak Tandean, and Ho-Chin Tsai. Constraints on scalar dark matter from direct experimental searches. *Physical Review*, D79:023521, Jan 2009.

[73] Xiao-Gang He, Tong Li, Xue-Qian Li, Jusak Tandean, and Ho-Chin Tsai. The simplest dark-matter model, CDMS II results, and Higgs detection at LHC. *Physics Letters*, B688:332 – 336, 2010.

[74] Xiao-Gang He and Jusak Tandean. Hidden higgs boson at the lhc and light dark matter searches. *Physical Review*, D84:075018, Oct 2011.

[75] J.A Hinton. The status of the hess project. *New Astronomy Reviews*, 48:331 – 337, 2004. 2nd VERITAS Symposium on the Astrophysics of Extragalactic Sources.

[76] D.E Holz and A Zee. Collisional dark matter and scalar phantoms. *Physics Letters*, B517:239 – 242, 2001.

[77] Gerard Jungman and Marc Kamionkowski. Neutrinos from particle decay in the sun and earth. *Physical Review*, D51:328–340, Jan 1995.

[78] Gerard Jungman, Marc Kamionkowski, and Kim Griest. Supersymmetric dark matter. *Physics Reports*, 267:195 – 373, 1996.

[79] Marc Kamionkowski and Michael S. Turner. Distinctive positron feature from particle dark-matter annihilations in the galatic halo. *Physical Review*, D43:1774–1780, Mar 1991.

[80] Rolf Kappl and Martin Wolfgang Winkler. New Limits on Dark Matter from Super-Kamiokande. *Nuclear Physics*, B850:505–521, 2011.

[81] Edward W. Kolb, Daniel J.H. Chung, and Antonio Riotto. WIMPzillas! hep-ph/9810361. pages 91–105, 1998.

[82] E. Komatsu et al. Seven-Year Wilkinson Microwave Anisotropy Probe (WMAP) Observations: Cosmological Interpretation. *The Astrophysical Journal Supplements*, 192:18, 2011.

[83] M. Kowalski et al. Improved Cosmological Constraints from New, Old and Combined Supernova Datasets. *The Astrophysical Journal*, 686:749–778, 2008.

[84] Alexander Kusenko. Sterile neutrinos, dark matter, and pulsar velocities in models with a higgs singlet. *Physical Review Letters*, 97:241301, Dec 2006.

[85] Hung-Liang Lai et al. New parton distributions for collider physics. *Physical Review*, D82:074024, 2010.

[86] Benjamin Lee and Steven Weinberg. Cosmological Lower Bound on Heavy-Neutrino Masses. *Physical Review Letters*, 39(4):165–168, 1977.

[87] Rose Natalie Lerner and John McDonald. Gauge singlet scalar as inflaton and thermal relic dark matter. *Physical Review*, D80:123507, 2009.

[88] Katharina Lodders. Solar system abundances and condensation temperatures of the elements. *The Astrophysical Journal*, 591(2):1220, 2003.

[89] Ewa L. Lokas and Gary A. Mamon. Dark matter distribution in the coma cluster from galaxy kinematics: breaking the massanisotropy degeneracy. *Monthly Notices of the Royal Astronomical Society*, 343(2):401–412, 2003.

[90] Laura Lopez Honorez, Emmanuel Nezri, Josep F. Oliver, and Michel H.G. Tytgat. The Inert Doublet Model: An Archetype for Dark Matter. *Journal of Cosmology and Astroparticle Physics*, 0702:028, 2007.

[91] Richard Massey, Thomas Kitching, and Johan Richard. The dark matter of gravitational lensing. *Reports of Progress in Physics*, 73:086901, 2010.

[92] D. Maurin, F. Donato, R. Taillet, and P. Salati. Cosmic rays below z=30 in a diffusion model: new constraints on propagation parameters. *The Astrophysical Journal*, 555:585–596, 2001.

[93] Christopher McCabe. Astrophysical uncertainties of dark matter direct detection experiments. *Physical Review*, D82:023530, Jul 2010.

[94] John McDonald. Gauge singlet scalars as cold dark matter. *Physical Review*, D50(6):3637–3649, 1994.

[95] John McDonald. Thermally generated gauge singlet scalars as self-interacting dark matter. *Physical Review Letters*, 88:091304, Feb 2002.

[96] David Merritt, Alister W. Graham, Ben Moore, Jrg Diemand, and Balsa Terzic. Empirical models for dark matter halos. i. nonparametric construction of density profiles and comparison with parametric models. *The Astronomical Journal*, 132(6):2685, 2006.

[97] Mordehai Milgrom. MOND: A pedagogical review. *Acta Physica Polonica*, B32:3613, 2001.

[98] Ben Moore, Carlos Calcáneo-Roldán, Joachim Stadel, Tom Quinn, George Lake, Sebastiano Ghigna, and Fabio Governato. Dark matter in draco and the local group: Implications for direct detection experiments. *Physical Review*, D64:063508, Aug 2001.

[99] J.F. Navarro, C.S. Frenk, and S.D.M. White. The Structure of Cold Dark Matter Halos. *The Astrophysical Journal*, 462:563, 1996.

[100] Donal O'Connell, Michael J. Ramsey-Musolf, and Mark B. Wise. Minimal extension of the standard model scalar sector. *Physical Review*, D75:037701, Feb 2007.

[101] Brian Patt and Frank Wilczek. Higgs-field portal into hidden sectors arXiv:hep-ph/0605188. 2006.

[102] Maxim Perelstein and Bibhushan Shakya. Antiprotons from Dark Matter: Effects of a Position-Dependent Diffusion Coefficient. *Physical Review*, D83:123508, 2011.

[103] Troy A. Porter, Igor V. Moskalenko, and Andrew W. Strong. Inverse compton emission from galactic supernova remnants: Effect of the interstellar radiation field. *The Astrophysical Journal Letters*, 648(1):L29, 2006.

[104] V. C. Rubin and W. K. Ford, Jr. Rotation of the Andromeda Nebula from a Spectroscopic Survey of Emission Regions. *The Astrophysical Journal*, 159:379, February 1970.

[105] S. Rudaz and F. W. Stecker. Cosmic-ray antiprotons, positrons, and gamma rays from halo dark matter annihilation. *The Astrophysical Journal*, 325:16–25, February 1988.

[106] Robert Schabinger and James D. Wells. A Minimal spontaneously broken hidden sector and its impact on Higgs boson physics at the large hadron collider. *Physical Review*, D72:093007, 2005.

[107] Geraldine Servant and Timothy M.P. Tait. Elastic scattering and direct detection of Kaluza-Klein dark matter. *New Journal of Physics*, 4:99, 2002.

[108] Geraldine Servant and Timothy M.P. Tait. Is the lightest Kaluza-Klein particle a viable dark matter candidate? *Nuclear Physics*, B650:391–419, 2003.

[109] M.A. Shifman, A.I. Vainshtein, and V.I. Zakharov. Remarks on Higgs-boson interactions with nucleons. *Physics Letters*, B78(4):443 – 446, 1978.

[110] Vanda Silveira and A. Zee. Scalar Phantoms. *Physics Letters*, B161:136, 1985.

[111] Torbjorn Sjostrand, Stephen Mrenna, and Peter Z. Skands. PYTHIA 6.4 Physics and Manual. *Journal of High Energy Physics*, 0605:026, 2006.

[112] Yoshiaki Sofue and Vera Rubin. Rotation curves of spiral galaxies. *Annual Review of Astronomy and Astrophysics*, 39(1):137–174, 2001.

[113] M. Spira, A. Djouadi, D. Graudenz, and P.M. Zerwas. Higgs boson production at the LHC. *Nuclear Physics*, B453:17–82, 1995.

[114] V. Springel, J. Wang, M. Vogelsberger, A. Ludlow, A. Jenkins, A. Helmi, J. F. Navarro, C. S. Frenk, and S. D. M. White. The aquarius project: the subhaloes of galactic haloes. *Monthly Notices of the Royal Astronomical Society*, 391(4):1685–1711, 2008.

[115] P. Sreekumar, D. L. Bertsch, B. L. Dingus, J. A. Esposito, C. E. Fichtel, R. C. Hartman, S. D. Hunter, G. Kanbach, D. A. Kniffen, Y. C. Lin, H. A. Mayer-Hasselwander, P. F. Michelson, C. von Montigny, A. Mcke, R. Mukherjee, P. L. Nolan, M. Pohl, O. Reimer, E. Schneid, J. G. Stacy, F. W. Stecker, D. J. Thompson, and T. D. Willis. Egret observations of the extragalactic gamma-ray emission. *The Astrophysical Journal*, 494(2):523, 1998.

[116] Alessandro Strumia and Francesco Vissani. Neutrino masses and mixings and... arXiv:hep-ph/0606054. 2006.

[117] K. Takeda et al. Nucleon strange quark content from two-flavor lattice QCD with exact chiral symmetry. *Physical Review*, D83:114506, 2011.

[118] T. Tanaka et al. An Indirect Search for WIMPs in the Sun using 3109.6 days of upward-going muons in Super-Kamiokande. *The Astrophysical Journal*, 742:78, 2011. Long author list - awaiting processing.

[119] A.I. Vainshtein, M.B. Voloshin, V.I. Zakharov, and M.A. Shifman. Low-energy theorems for Higgs meson interaction with photons. *Soviet Journal of Nuclear Physics*, 30:711–716, 1979.

[120] A. E. Vladimirov, S. W. Digel, G. Jóhannesson, P. F. Michelson, I. V. Moskalenko, P. L. Nolan, E. Orlando, T. A. Porter, and A. W. Strong. GALPROP WebRun: An internet-based service for calculating galactic cosmic ray propagation and associated photon emissions. *Computer Physics Communications*, 182:1156–1161, May 2011.

[121] G. Wikström and J. Edsjö. Limits on the WIMP-nucleon scattering cross-section from neutrino telescopes. *Journal of Cosmology and Astroparticle Physics*, 2009(04):009, 2009.

[122] Carlos E. Yaguna. Gamma rays from the annihilation of singlet scalar dark matter. *Journal of Cosmology and Astroparticle Physics*, 2009(03):003, 2009.

[123] F. Zwicky. Die Rotverschiebung von extragalaktischen Nebeln. *Helvetica Physica Acta*, 6:110–127, 1933.

Appendix A

Calculations

A.1 Tree Level Singlet Annihilation Cross Sections

In this section we use the following Feynman rules to compute matrix elements:

Singlet-Higgs Vertex

$$V_{SSh} = \frac{i\eta v_h}{2}$$

Higgs-Fermion Vertex

$$V_{ffh} = \frac{-im_f}{v_h}$$

Higgs-W Boson Vertex

$$V_{WWh} = \frac{2im_W^2 g^{\mu\nu}}{v_h}$$

Higgs-Z Boson Vertex

$$V_{ZZh} = \frac{2im_Z^2 g^{\mu\nu}}{v_h}$$

3-point Higgs Vertex

$$V_{hhh} = -3i\frac{m_h^2}{v_h}$$

Higgs Propagator
(We use here the standard prescription for the propagator of an unstable particle.)

$$P_h = \frac{i}{q^2 + m_h^2 - im_h\Gamma_h}$$

External Singlet

$$\langle S(p)| = |S(p)\rangle = 1$$

External Fermion

$$\langle F(p)| = \bar{u}(p)$$

$$|F(p)\rangle = u(p)$$

External Antifermion

$$\left\langle \bar{F}(p)\right| = v(p)$$

$$\left|\bar{F}(p)\right\rangle = \bar{v}(p)$$

(u and v are Dirac spinors; we do not require an explicit basis)

External Gauge Boson

$$\langle G(p)| = \bar{\epsilon}_{\mu}^{\alpha}(p)$$

$$|G(p)\rangle = \epsilon_{\mu}^{\alpha}(p)$$

(the ϵ are polarization vectors)
External Higgs

$$\langle h(p)| = |h(p)\rangle = 1$$

Note that we use the metric signature (-,+,+,+).

Fermion Production:
The above rules allow us to write the matrix element for fermion production as

$$i\mathcal{M} = \frac{im_f}{v_h}\frac{i\eta v_h}{2}\frac{i\bar{u}(k)v(k')}{q^2 + m_h^2 - im_h\Gamma_h}.$$

To obtain the cross section, we square the norm

$$|\mathcal{M}|^2 = \frac{\eta^2 m_f^2}{4}\frac{[\bar{u}(k)v(k')\bar{v}(k')u(k)]}{\left(q^2 + m_h^2\right)^2 + m_h^2\Gamma_h^2}$$

and then sum over the final spin states. We can use the standard trace technique of evaluating the spin sums of the Dirac spinors

$$\sum_{spins}|\mathcal{M}|^2 = \frac{\eta^2 m_f^2}{4}\frac{Tr\left[\left(k\cdot\gamma + m_f\right)\left(k'\cdot\gamma + m_f\right)\right]}{\left(q^2 + m_h^2\right)^2 + m_h^2\Gamma_h^2}.$$

The trace evaluates to

$$\sum_{spins}|\mathcal{M}|^2 = \frac{\eta^2 m_f^2}{4}\frac{4\left[k\cdot k' - m_f^2\right]}{\left(q^2 + m_h^2\right)^2 + m_h^2\Gamma_h^2}.$$

We work in the center of mass frame, in which (see Figure A.1)
$p = (E, 0, 0, |\mathbf{p}|)$
$p' = (E, 0, 0, -|\mathbf{p}|)$
$q = k + k' = p + p' = -2E$
$k = (E_f, 0, |\mathbf{k}|\cos(\theta), |\mathbf{k}|\sin(\theta))$
$k' = (E_f, 0, -|\mathbf{k}'|\cos(\theta), -|\mathbf{k}'|\sin(\theta))$.
Conservation of momentum implies that$|\mathbf{k}| = |\mathbf{k}'|$.
Then

$$k\cdot k' = -\left(E_f^2 + |k|^2\right)$$

The 3-momentum squared is $|\mathbf{k}|^2 = -\left(E_f^2 - m_f^2\right)$, from the definition of relativistic energy. We also have $q^2 = (p+p')^2 = (-2E + |\mathbf{p}| - |\mathbf{p}|)^2$, giving

$$\sum_{spins}|\mathcal{M}|^2 = \frac{\eta^2 m_f^2}{4}\frac{4\left[E_f^2 + |\mathbf{k}|^2 - m_f^2\right]}{\left(4E^2 + m_h^2\right)^2 + m_h^2\Gamma_h^2}.$$

In the nonrelatvistic limit, $p \to 0 \Rightarrow E \to m_S$. Then $q^2 = 4m_S^2$ and $E_f = E = m_S$ by conservation of energy. So then $|\mathbf{k}|^2 = m_S^2 - m_f^2 \Rightarrow k\cdot k' = E_f^2 + |\mathbf{k}|^2 = 2m_S^2 - m_f^2$.

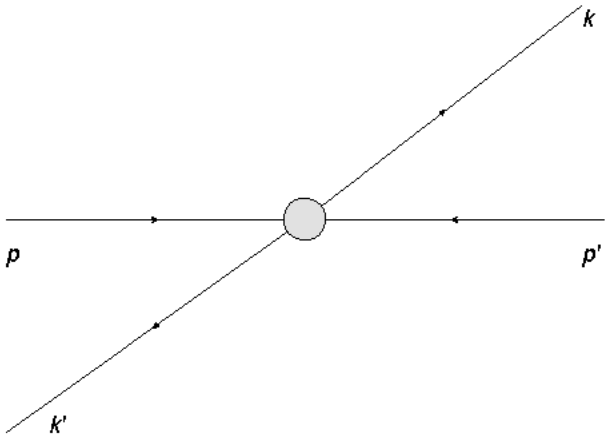

Figure A.1: Singlet Annihilation Kinematics

We then have

$$\sum_{spins} |\mathcal{M}|^2 = \eta^2 m_f^2 \frac{\left[2m_S^2 - 2m_f^2\right]}{\left(4m_S^2 + m_h^2\right)^2 + m_h^2\Gamma_h^2}.$$

Now we must combine this with the phase space normalization

$$v_{rel}\frac{d\sigma}{d\Omega} = \frac{\sqrt{m_S^2 - m_f^2}}{8\pi m_S^3} N_c \sum_{spins} |\mathcal{M}|^2$$

and perform the angular integration to obtain the cross section

$$v\sigma_{SS\to ff} = \eta^2 \frac{N_c m_f^2}{4\pi m_S^3} \frac{\sqrt{m_S^2 - m_f^2}^3}{\left(4m_S^2 + m_h^2\right)^2 + m_h^2\Gamma_h^2}.$$

The factor N_c counts the colors of the fermions. It is 3 for quarks and 1 for leptons.

Vector Boson Production:
We generate a matrix element of the form:

$$i\mathcal{M} = \epsilon_\mu^\alpha(k)\epsilon_\nu^\beta(k')g^{\mu\nu}\frac{2im_V^2}{v_h}\frac{i\eta v_h}{2}\frac{i}{q^2 + m_h^2 - im_h\Gamma_h}$$

As usual, we must square the norm

$$|\mathcal{M}|^2 = \eta^2 m_V^4 \frac{\left[\epsilon_\mu^\alpha(k)\epsilon_\nu^\beta(k')g^{\mu\nu}\right]^2}{\left(q^2 + m_h^2\right)^2 + m_h^2\Gamma_h^2}$$

and sum over final state polarizations. We can use the following identity for the polarization sums of massive spin-1 particles:

$$\sum_{spins}\left[\epsilon_\mu^\alpha(k)\epsilon_\nu^\beta(k')g^{\mu\nu}\right]^2 = \left(g^{\mu\nu} + \frac{k^\mu k^\nu}{m_V^2}\right)\left(g_{\nu\mu} + \frac{k_\nu' k_\mu'}{m_V^2}\right) = 2 + \frac{\left(k\cdot k'\right)^2}{m_V^4}.$$

Then we have

$$\sum_{spins} |\mathcal{M}|^2 = \frac{\eta^2 m_V^4}{\left(q^2 + m_h^2\right)^2 + m_h^2 \Gamma_h^2} \left(2 + \frac{\left(k \cdot k^{'}\right)^2}{m_V^4} \right).$$

Working in the center of mass frame for the two singlets again gives 4-momenta
$p = (E, 0, 0, |\mathbf{p}|)$
$p' = (E, 0, 0, -|\mathbf{p}|)$
$q = k + k' = p + p' = 2E$
$k = (E_V, 0, |\mathbf{k}|\cos(\theta), |\mathbf{k}|\sin(\theta))$
$k' = (E_V, 0, -|\mathbf{k}'|\cos(\theta), -|\mathbf{k}'|\sin(\theta))$.
These momenta give, as above $k \cdot k' = E_V^2 + |\mathbf{k}|^2$, $q^2 = (p + p')^2 = (-2E - |\mathbf{p}| + |\mathbf{p}|)^2 = 4E^2$

$$\sum_{spins} |\mathcal{M}|^2 = \frac{\eta^2 m_V^4}{\left(4E^2 + m_h^2\right)^2 + m_h^2 \Gamma_h^2} \left(2 + \frac{\left(E_V^2 + |\mathbf{k}|^2\right)^2}{m_V^4} \right)$$

In the nonrelativistic limit, we again get $E_V = m_S$, $k \cdot k' = 2m_S^2 - m_V^2$, and $q^2 = 4m_S^2$. These expressions can be inserted into the above formula for the squared matrix element to give

$$\sum_{spins} |\mathcal{M}|^2 = \frac{\eta^2 m_V^4}{\left(4m_S^2 + m_h^2\right)^2 + m_h^2 \Gamma_h^2} \left(2 + \frac{\left(2m_S^2 - m_V^2\right)^2}{m_V^4} \right)$$

$$= \frac{\eta^2 \left[2m_V^4 + \left(2m_S^2 - m_V^2\right)^2 \right]}{\left(4m_S^2 + m_h^2\right)^2 + m_h^2 \Gamma_h^2} = \frac{\eta^2 \left[3m_V^4 + 4m_S^4 - 4m_S^2 m_V^2 \right]}{\left(4m_S^2 + m_h^2\right)^2 + m_h^2 \Gamma_h^2}$$

Then the phase space integral is

$$v_{rel} \frac{d\sigma}{d\Omega} == \frac{\sqrt{m_S^2 - m_V^2}}{8\pi m_S^3} \frac{1}{1 + \delta_z} \sum_{spins} |\mathcal{M}|^2$$

where the factor δ_z is used to count the symmetry factors for the Z boson, since it is its own antiparticle. It is 1 for the Z boson and 0 for the W boson. Insertion of the matrix element and evaluating the angular integral gives:

$$v\sigma_{SS \to WW} = \eta^2 \frac{\sqrt{m_S^2 - m_W^2}}{4\pi m_S^3} \frac{3m_W^4 - 4m_W^2 m_S^2 + 4m_S^4}{\left(4m_S^2 + m_h^2\right)^2 + m_h^2 \Gamma_h^2}$$

and

$$v\sigma_{SS \to ZZ} = \eta^2 \frac{\sqrt{m_S^2 - m_Z^2}}{8\pi m_S^3} \frac{3m_Z^4 - 4m_Z^2 m_S^2 + 4m_S^4}{\left(4m_S^2 + m_h^2\right)^2 + m_h^2 \Gamma_h^2}.$$

Higgs Boson Production:
This process involves four diagrams, as seen in Figure A.2. The Feynman rules allow us to write the matrix element as

$$i\mathcal{M} = -\frac{i\eta v_h}{2} + i^3 \frac{6m_h^2 \eta v_h}{q_1^2 + m_h^2 - m_h \Gamma_h} - \frac{\eta^2 v_h^2}{4} \frac{i}{q_2^2 + m_S^2 - i\epsilon} - \frac{\eta^2 v_h^2}{4} \frac{i}{q_3^2 + m_S^2 - i\epsilon}$$

where the terms appear in the order they do in the Figure.
This can be simplified to the form

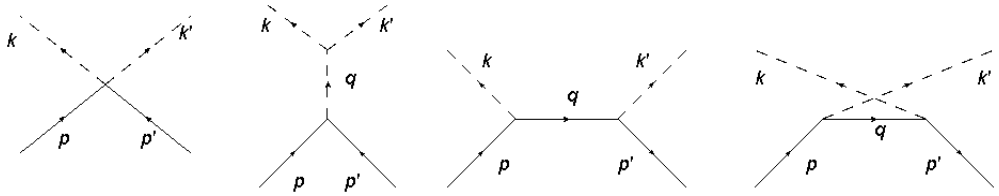

Figure A.2: Higgs Boson Production from Singlet Annihilation

$$i\mathcal{M} = -\frac{i\eta v_h}{2} - i\frac{6m_h^2\eta v_h}{q_1^2 + m_h^2 - im_h\Gamma_h} - \frac{\eta^2 v_h^2}{4} i\left(\frac{1}{q_2^2 + m_S^2 - i\epsilon} - \frac{1}{q_3^2 + m_S^2 - i\epsilon}\right).$$

We have, in the center of mass frame for the two singlets, the 4-momenta
$p = (E, 0, 0, |\mathbf{p}|)$
$p' = (E, 0, 0, -|\mathbf{p}|)$
$q_1 = k + k' = p + p' = 2E$
$q_2 = p - k$
$q_3 = p - k'$
$k = (E_h, 0, |\mathbf{k}|\cos(\theta), |\mathbf{k}|\sin(\theta))$
$k' = (E_h, 0, -|\mathbf{k}'|\cos(\theta), -|\mathbf{k}'|\sin(\theta))$.

These momenta give in the nonrelativstic limit $k \cdot k' = -E_h^2 - |\mathbf{k}|^2 = 2m_S^2 + m_h^2$, $q_1^2 = (p+p')^2 = (-2E - |\mathbf{p}| + |\mathbf{p}|)^2 = 4E^2 = 4m_S^2$, $q_2^2 = q_3^2 = 2m_S^2 - m_h^2$.

There are no spins to sum over, so we can simply square the matrix element to obtain, with some simplification

$$|\mathcal{M}|^2 = \eta^2 \left|\frac{2m_S^2 + m_h^2}{4m_S^2 - m_h^2 + im_h\Gamma_h} - \frac{2\eta v_h^2}{2m_S^2 - m_h^2}\right|^2.$$

We have used that $m_h \gg \Gamma_h$, and so Γ_h does not contribute to the numerator when the fractions are combined. Inclusion of the phase space integral as usual and integration leads to

$$v\sigma_{SS\to hh} = \eta^2 \frac{\sqrt{m_S^2 - m_h^2}}{16\pi m_S^3} \left|\frac{2m_S^2 + m_h^2}{4m_S^2 - m_h^2 + im_h\Gamma_h} - \frac{2\eta v_h^2}{2m_S^2 - m_h^2}\right|^2.$$

Massless Gauge Boson Production:

We proceed with a tree level calculation using the effective Lagrangian referenced in Chapter 2. The gluon and photon production mechanisms are identical up to different coupling constants in this effective field theory. The basic diagram appears in Figure A.3, where the obscured vertex represents the $\gamma\gamma h$ or ggh coupling, which has a Feynman rule giving it a value of $V_{ggh} = -iA_g H^{\mu\nu}\delta^{AB}$ or $V_{\gamma\gamma h} = -iA_\gamma H^{\mu\nu}(k_1, k_2)$ where the Dirac tensor is a function of the gauge boson momenta $H^{\mu\nu}(k_1, k_2) = \delta^{\mu\nu}(k_1 \cdot k_2) - k_1^\nu k_2^\mu$, the A_i are coupling constants, and the Dirac delta represents conservation of color at the vertex, present only for the gluon case. The other Feynman rules are as usual.

The matrix element can be written

$$i\mathcal{M} = \epsilon_\mu^\alpha(k)\epsilon_\nu^\beta(k')H^{\mu\nu}(k, k')iA\frac{i\eta v_h}{2}\frac{i}{q^2 + m_h^2 - im_h\Gamma_h}$$

Inserting the vertex tensor and contracting it with the boson polarization vectors gives

$$i\mathcal{M} = i^2 A\frac{i\eta v_h}{2}\frac{\left[\left(\epsilon^\alpha(k)\cdot\epsilon^\beta(k')\right)(k\cdot k') - \left(\epsilon^\alpha(k)\cdot k'\right)\left(\epsilon^\beta(k')\cdot k\right)\right]}{q^2 + m_h^2 - im_h\Gamma_h}$$

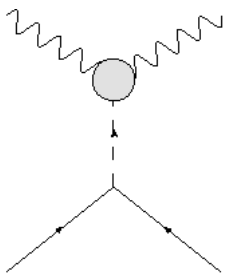

Figure A.3: Massless Gauge Boson Production from Singlet Annihilation (Effective Tree Level Theory)

and then squaring (and summing over spins, which sets the second numerator term to zero) gives

$$\sum_{spins} |\mathcal{M}|^2 = \frac{1}{4} \frac{A^2 \eta^2 v_h^2}{\left(q^2 + m_h^2\right)^2 + m_h^2 \Gamma_h^2} \left(\sum_{spins} \left(\epsilon^\alpha(k) \cdot \epsilon^\beta(k') \right) (k \cdot k') \right).$$

As usual, the center of mass frame simplifies the kinematics considerably, giving four-momenta
$p = (E, 0, 0, |\mathbf{p}|)$
$p' = (E, 0, 0, -|\mathbf{p}|)$
$q = k + k' = p + p' = 2E$
$k = (E_k, 0, |\mathbf{k}| \cos(\theta), |\mathbf{k}| \sin(\theta))$
$k' = (E_k, 0, -|\mathbf{k}'| \cos(\theta), -|\mathbf{k}'| \sin(\theta))$.
These momenta give $k \cdot k' = -E_b^2 - |\mathbf{k}|^2 = -4E_k^2$, $q^2 = (p + p')^2 = (-2E - |\mathbf{p}| + |\mathbf{p}|)^2 = 4E^2$, where we used that the final state bosons were on-shell ($k^2 = 0$).

$$\Rightarrow \sum_{spins} |\mathcal{M}|^2 = \frac{1}{4} \frac{A^2 \eta^2 v_h^2}{\left(q^2 + m_h^2\right)^2 + m_h^2 \Gamma_h^2} \left(4E_k^2\right).$$

In the nonrelativistic limit, $E = E_k = m_S$

$$\Rightarrow \sum_{spins} |\mathcal{M}|^2 = \frac{A^2 \eta^2 v_h^2 m_S^2}{\left(4m_S^2 + m_h^2\right)^2 + m_h^2 \Gamma_h^2}$$

which gives us a cross section of, using the usual phase space integral

$$v\sigma_{SS \to bb} = \frac{1}{s} \frac{A^2 \eta^2 v_h^2 m_S^2}{\left(4m_S^2 + m_h^2\right)^2 + m_h^2 \Gamma_h^2}$$

where s is the symmetry factor of the bosons. Since the cross section is scaled by A^2, and A contains the electromagnetic structure constant for the case of photons ($\alpha_{em} = 1/137$) or the strong coupling constant for the case of gluons ($\alpha_s \simeq 0.1$ for the relevant energy scale), the cross section is scaled by the square of these numbers. Since they are quite small, we can see that the direct production of massless gauge bosons is supressed quite strongly compared to massive particles. This is of course a consequence of the fact that these particles can only be directly produced in loop order processes.

A.2 Tree Level Nuclear Recoil Cross Section

The diagram appears in Figure 3.1. The Feynman rule for the effective Higgs-Nucleon interaction vertex is

$$V_{NNh} = ig$$

The matrix element for the process is

$$i\mathcal{M} = ig\frac{i\eta v_h}{2}\frac{i\bar{u}(k^{'})u(k)}{q^2 + m_h^2 - im_h\Gamma_h}$$

which we then square the norm of to obtain

$$|\mathcal{M}|^2 = \frac{\eta^2 g^2 v_h^2}{4}\frac{\left[\bar{u}(k^{'})u(k)\bar{u}(k)u(k^{'})\right]}{\left(q^2 + m_h^2\right)^2 + m_h^2\Gamma_h^2}.$$

We sum over the final and average over the initial spins and take the trace to obtain

$$\frac{1}{2}\sum_{spins}|\mathcal{M}|^2 = \frac{\eta^2 g^2 v_h^2}{4}\frac{Tr\left[\left(k'\cdot\gamma\right)\left(k\cdot\gamma\right) + m_N^2\right]}{\left(q^2 + m_h^2\right)^2 + m_h^2\Gamma_h^2}$$

$$= \frac{\eta^2 g^2 v_h^2}{4}\frac{4\left[\left(k'\cdot k\right) + m_N^2\right]}{\left(q^2 + m_h^2\right)^2 + m_h^2\Gamma_h^2}.$$

In the rest frame of the nucleon, we have $k'\cdot k = m_N E_{k'}$, and $q^2 = \left(k' - k\right)^2$

$$\Rightarrow \frac{1}{2}\sum_{spins}|\mathcal{M}|^2 = \eta^2 g^2 v_h^2\frac{\left[\left(m_N E_{k'}\right) + m_N^2\right]}{\left(\left(k' - k\right)^2 + m_h^2\right)^2 + m_h^2\Gamma_h^2}.$$

Inclusion of the Lorentz invariant phase space factor in the nonrelativistic limit $E_S' = E_S = m_S$, $E_{k'} = m_N$, and $k' - k = 0$ and integration over the solid angle gives

$$\sigma = \frac{\eta^2 g^2 v_h^2}{8\pi}\frac{1}{m_h^4 + m_h^2\Gamma_h^2}\frac{m_N^2}{\left(m_S + m_N\right)^2}$$

Taking into account that $\Gamma_h^2 \ll m_h^2$, we obtain the final result that was presented in Chapter 3

$$\sigma_{SN} = \frac{g^2\eta^2 v_h^2}{4\pi}\frac{m_N^2}{m_h^4\left(m_S + m_N\right)^2}.$$

A.3 Gluon Fusion Singlet Production Cross Section

The singlet production via gluon fusion through an intermediate Higgs process can be described by the pair of Feynman diagrams in Figure A.4. We label the momenta as follows:

l =loop momentum

k_1, k_2 =gluon momenta

q =Higgs momentum

p_1, p_2 =singlet momenta.

We write the matrix element in terms of l, k_1, k_2 whenever possible, as these are the variables that must be integrated over.

The QCD Feynman rules we use are:

Quark-gluon interaction vertex

$$V_{gqq} = -ig_s\gamma^\mu\frac{\lambda^a}{2}$$

Quark propagator

$$P_q = \frac{i\left(p\cdot\gamma + m_q\right)}{p^2 + m_q^2 - i\epsilon}.$$

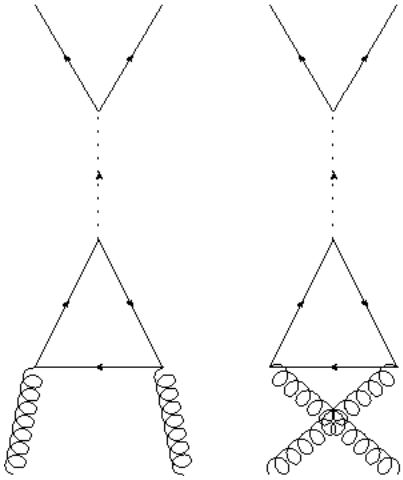

Figure A.4: Diagrams Contributing to Singlet Production via Gluon Fusion

With a total factor of $-\int \frac{d^4l}{(2\pi)^4}$ for the quark loop. Throughout the computation, we ignore for simplicity color conservation factors at the vertices.

These rules give us a matrix element of the form:

$$i\mathcal{M} = (-ig_s)^2 \frac{\left[t^a t^b\right]}{4} \frac{i\eta v}{2} \int \frac{d^4l}{(2\pi)^4} \frac{i}{q^2 + m_h^2 - i\Gamma_h m_h}$$

$$\times \Bigg\{ \gamma^\nu \frac{i\left(l\cdot\gamma - k_1\cdot\gamma + m_t\right)}{\left(l-k_1\right)^2 + m_t^2 - i\epsilon} \frac{i\left(l\cdot\gamma + k_2\cdot\gamma + m_t\right)}{\left(l+k_2\right)^2 + m_t^2 - i\epsilon} \gamma^\mu \frac{i\left(l\cdot\gamma + m_t\right)}{l^2 + m_t^2 - i\epsilon}$$

$$+\gamma^\nu \frac{i\left(-l\cdot\gamma + m_t\right)}{\left(-l\right)^2 + m_t^2 - i\epsilon} \gamma^\mu \frac{i\left(-l\cdot\gamma + k_2\cdot\gamma + m_t\right)}{\left(-l+k_2\right)^2 + m_t^2 - i\epsilon} \frac{i\left(-l\cdot\gamma - k_1\cdot\gamma + m_t\right)}{\left(-l-k_1\right)^2 + m_t^2 - i\epsilon} \Bigg\}$$

We transform $l \Rightarrow -l$ in the second term to allow the denominators to be identical. The matrix element then becomes:

$$i\mathcal{M} = (-ig_s)^2 \frac{Tr\left[t^a t^b\right]}{4} \frac{i\eta v}{2} \frac{i^4}{q^2 + m_h^2 - i\Gamma_h m_h} \times$$

$$\int \frac{d^4l}{(2\pi)^4} \Bigg\{ \frac{Tr\left[\gamma^\nu \left(l\cdot\gamma - k_1\cdot\gamma + m_t\right)\left(l\cdot\gamma + k_2\cdot\gamma + m_t\right)\gamma^\mu \left(l\cdot\gamma + m_t\right)\right]}{\left(\left(l-k_1\right)^2 + m_t^2 - i\epsilon\right)\left(\left(l+k_2\right)^2 + m_t^2 - i\epsilon\right)\left(l^2 + m_t^2 - i\epsilon\right)}$$

$$+ \frac{Tr\left[\gamma^\nu \left(-l\cdot\gamma + m_t\right)\gamma^\mu \left(-l\cdot\gamma + k_2\cdot\gamma + m_t\right)\left(-l\cdot\gamma - k_1\cdot\gamma + m_t\right)\right]}{\left(\left(l-k_1\right)^2 + m_t^2 - i\epsilon\right)\left(\left(l+k_2\right)^2 + m_t^2 - i\epsilon\right)\left(l^2 + m_t^2 - i\epsilon\right)} \Bigg\}$$

$$= A(N/D_1 D_2 D_3)$$

with the prefactor

$$A = (-ig_s)^2 \frac{Tr\left[t^a t^b\right]}{4} \frac{i\eta v}{2} \frac{i^4}{q^2 + m_h^2 - i\Gamma_h m_h}$$

The trace of the numerator is evaluated using the standard rules of traces of products of γ matrices, giving

$$N = 8m_t \left(k_1^\mu k_2^\nu - k_1^\nu k_2^\mu + 2k_2^\mu l^\nu - 2k_1^\nu l^\mu + 4l^\mu l^\nu - g^{\mu\nu} l \cdot l - g^{\mu\nu} k_1 \cdot k_2 - m_t^2 g^{\mu\nu}\right).$$

Now we attempt to evaluate the loop integration using a Feynman parameterization. We use

$$\frac{1}{D_1 D_2 D_3} = 2\int\int dz_1 dz_2 \frac{1}{\left[D_1 + (D_2 - D_1)z_1 + (D_3 - D_1)z_2\right]^3} = 2\int\int dz_1 dz_2 \frac{1}{[D]^3}.$$

This transforms the denominator to

$$D_1 D_2 D_3 \to D = \left(l^2 + m_t^2\right) + \left[\left(l - k_1\right)^2 + m_t^2 - \left(l^2 + m_t^2\right)\right] z_1$$

$$+ \left[\left(l + k_2\right)^2 + m_t^2 - \left(l^2 + m_t^2\right)\right] z_2 + i\epsilon.$$

We complete the square by undergoing a change of variables

$$P = l - z_2 k_2 + z_1 k_1$$

which requires us to change the denominator and numerator

$$D = P^2 + m_t^2 + z_2 k_2^2 + z_1 k_1^2 + 2z_1 z_2 k_1 \cdot k_2 - z_2^2 k_2^2 - z_1^2 k_1^2$$

$$\frac{N}{8m_t} = k_1^\mu k_2^\nu - k_1^\nu k_2^\mu + 2k_2^\mu \left(P + z_2 k_2 - z_1 k_1\right)^\nu - 2k_1^\nu \left(P + z_2 k_2 - z_1 k_1\right)^\mu$$

$$+4\left(P^\mu P^\nu + z_2 P^\mu k_2^\nu - z_1 P^\mu k_1^\nu + z_2 P^\nu k_2^\mu - z_1 k_1^\mu P^\nu + z_2^2 k_2^\mu k_2^\nu - z_1 z_2 k_1^\nu k_2^\mu - z_1 z_2 k_2^\nu k_1^\mu + z_1^2 k_1^\mu k_1^\nu\right)$$

$$-g^{\mu\nu}\left(P^2 - z_2^2 k_2^2 - z_1^2 k_1^2 + 2z_2 k_2 P + 2z_2^2 k_2^2 - 2z_2 z_1 k_1 \cdot k_2\right)$$

$$-g^{\mu\nu}\left(-2z_1 k_1 \cdot P - 2z_1 z_2 k_1 \cdot k_2 + 2z_1^2 k_1^2 + 2z_1 z_2 k_1 \cdot k_2 + k_1 \cdot k_2 + m_t^2\right)$$

At this point, the matrix element is of the form

$$i\mathcal{M} = 2A\int\int dz_1 dz_2 \int \frac{d^4 P}{(2\pi)^4} 8m_t \frac{N}{D^3}.$$

Note that the P integral can be reduced to scalar, vector and tensor components in P. By symmetry of the integration domain, the terms with a single P^μ do not contribute to the integral. To evaluate the troublesome $P^\mu P^\nu$ term, we note that it contributes as the $P^2 g^{\mu\nu}$ term to the integral and since the terms have opposite signs, they cancel. This leaves only the scalar terms remaining, giving

$$i\mathcal{M} = 2A\int\int dz_1 dz_2 \int \frac{d^4 P}{(2\pi)^4} 8m_t \frac{\tilde{N}}{\left(P^2 - \Delta\right)^3}$$

with

$$\tilde{N} = k_1^\mu k_2^\nu - k_1^\nu k_2^\mu + 2z_2 k_2^\mu k_2^\nu - 2z_1 k_2^\mu k_1^\nu - 2z_2 k_2^\mu k_1^\nu + 2z_1 k_1^\mu k_1^\nu$$

$$+4z_2^2 k_2^\mu k_2^\nu - 4z_1 z_2 k_2^\mu k_1^\nu - 4z_1 z_2 k_1^\mu k_2^\nu + 4z_1^2 k_1^\mu k_1^\nu$$

$$+g^{\mu\nu}\left(z_2^2 k_2^2 + z_1^2 k_1^2 - 2z_2^2 k_2^2 - 2z_1^2 k_1^2 + 2z_1 z_2 k_1 \cdot k_2 - k_1 \cdot k_2 - m_t^2\right)$$

and

$$\Delta = P^2 - D$$

$$= -\left(m_t^2 + z_2 k_2^2 + z_1 k_1^2 + 2z_1 z_2 k_1 \cdot k_2 - z_2^2 k_2^2 - z_1^2 k_1^2\right).$$

The scalar P integral has taken a standard form whose solution is known

$$I = \int \frac{d^4 P}{(2\pi)^4} \frac{1}{\left(P^2 - \Delta\right)^3} = -i\pi \frac{\Gamma(1)}{\Gamma(3)} \frac{1}{\Delta}$$

$$\Rightarrow i\mathcal{M} = 2A \int\int dz_1 dz_2 8 m_t \left(-i\pi\right) \frac{\Gamma(1)}{\Gamma(3)} \frac{\tilde{N}}{\Delta}.$$

The Γ are the usual gamma functions. We extract the remaining integrals and take on-shell gluons ($k_i^2 = 0$), eliminating many troublesome terms, especially in the denominator. We can reduce

$$\tilde{N} = k_1^\mu k_2^\nu - k_1^\nu k_2^\mu - 2z_1 k_2^\mu k_1^\nu - 2z_2 k_2^\mu k_1^\nu - 4z_1 z_2 k_2^\mu k_1^\nu - 4z_1 z_2 k_1^\mu k_2^\nu$$

$$+g^{\mu\nu}\left(2z_1 z_2 k_1 \cdot k_2 - k_1 \cdot k_2 - m_t^2\right)$$

$$\Delta = -\left(m_t^2 + 2z_1 z_2 k_1 \cdot k_2\right)$$

$$\Rightarrow i\mathcal{M} = 2A \int\int dz_1 dz_2 8 m_t i\pi \frac{\Gamma(1)}{\Gamma(3)} \frac{\tilde{N}}{\left(m_t^2 + 2z_1 z_2 k_1 \cdot k_2\right)}.$$

We define the integral I_2

$$I_2 = 8i\pi^2 m_t \epsilon_\mu(\mathbf{k}_1, s_1)\epsilon_\nu(\mathbf{k}_2, s_2)$$

$$\times \int_0^1 dz_1 \int_0^{1-z_1} dz_2 \frac{-m_t^2 g^{\mu\nu} - g^{\mu\nu} k_1 \cdot k_2 \left(1 - 2z_1 z_2\right) - 4z_1 z_2 k_2^\mu k_1^\nu + \left(z_1 + z_2\right) k_2^\mu k_1^\nu}{2k_1 \cdot k_2 z_1 z_2 + m_t^2}.$$

Fixing the gauge allows us to set the $k_2^\mu k_1^\nu$ tensor terms to zero, giving

$$I_2 = -8i\pi^2 m_t \epsilon_\mu(\mathbf{k}_1, s_1)\epsilon_\nu(\mathbf{k}_2, s_2) \int_0^1 dz_1 \int_0^{1-z_1} dz_2 \frac{m_t^2 + k_1 \cdot k_2 \left(1 - 2z_1 z_2\right)}{2k_1 \cdot k_2 z_1 z_2 + m_t^2}$$

$$= -8i\pi^2 m_t \epsilon_\mu(\mathbf{k}_1, s_1)\epsilon_\nu(\mathbf{k}_2, s_2) \int_0^1 dz_1 \int_0^{1-z_1} dz_2 \left(\frac{2m_t^2 + k_1 \cdot k_2}{2k_1 \cdot k_2 z_1 z_2 + m_t^2} - 1\right)$$

$$= -8i\pi^2 m_t \epsilon_\mu(\mathbf{k}_1, s_1)\epsilon_\nu(\mathbf{k}_2, s_2)\left[\left(\int_0^1 dz_1 \int_0^{1-z_1} dz_2 \frac{2m_t^2 + k_1\cdot k_2}{2k_1\cdot k_2 z_1 z_2 + m_t^2}\right) - \frac{1}{2}\right]$$

$$= -8i\pi^2 m_t \epsilon_\mu(\mathbf{k}_1, s_1)\epsilon_\nu(\mathbf{k}_2, s_2)\left[\frac{2m_t^2 + k_1\cdot k_2}{m_t^2}\left(\int_0^1 dz_1 \int_0^{1-z_1} dz_2 \frac{1}{1 - a z_1 z_2}\right) - \frac{1}{2}\right]$$

$$= -8i\pi^2 m_t \epsilon_\mu(\mathbf{k}_1, s_1)\epsilon_\nu(\mathbf{k}_2, s_2)\left[\frac{2m_t^2 + k_1\cdot k_2}{a m_t^2} J - \frac{1}{2}\right]$$

with

$$J = -a\int_0^1 dz_1 \int_0^{1-z_1} dz_2 \frac{1}{1 - a z_1 z_2}$$

$$= \int_0^1 dz_1 \frac{\ln|1 - a z_1 (1 - z_1)|}{z_1}.$$

We next move to center of mass frame for the gluons, allowing the simplification $k_1 \cdot k_2 = 2\mathbf{k}^2$, where $\mathbf{k}$ is the 3-momentum of either of the gluons in the center of mass frame. We have defined $a = 4\mathbf{k}^2/m_t^2$.

The value of the integral J is known, and can be written, depending on the value of a

$$J = \begin{cases} -2\left[\arcsin\left(\sqrt{\frac{a}{4}}\right)\right]^2 & if \quad 0 < a < 4 \\ \frac{1}{2}\left[\ln\left(\frac{\sqrt{a}+\sqrt{a-4}}{\sqrt{a}-\sqrt{a-4}}\right)\right]^2 - \frac{\pi^2}{2} - i\pi \ln\left(\frac{\sqrt{a}+\sqrt{a-4}}{\sqrt{a}-\sqrt{a-4}}\right) & if \quad a > 4 \end{cases}$$

So then

$$I_2 = T\begin{cases} \left[\frac{2m_t^2+k_1\cdot k_2}{a m_t^2} - 2\left[\arcsin\left(\sqrt{\frac{a}{4}}\right)\right]^2 - \frac{1}{2}\right] & if \quad 0 < a < 4 \\ \left[\frac{2m_t^2+k_1\cdot k_2}{a m_t^2}\left\{\frac{1}{2}\left[\ln\left(\frac{\sqrt{a}+\sqrt{a-4}}{\sqrt{a}-\sqrt{a-4}}\right)\right]^2 - \frac{\pi^2}{2} - i\pi\ln\left(\frac{\sqrt{a}+\sqrt{a-4}}{\sqrt{a}-\sqrt{a-4}}\right)\right\} - \frac{1}{2}\right] & if \quad a > 4 \end{cases}$$

with $T = -8i\pi^2 m_t \epsilon_\mu(\mathbf{k}_1, s_1)\epsilon_\nu(\mathbf{k}_2, s_2)$.

For the free gluon fusion process at high energies, $a > 4$, but when we take the gluon distribution functions into account, the other case becomes possible.

A basic parameterization of the gluon distribution functions is

$$f_g(x) = \frac{5}{2}\frac{(1-x)^4}{x}.$$

The gluons carry fractions of the proton momenta $\mathbf{k}_{g1} = x_1\mathbf{k}_p$ and $\mathbf{k}_{g2} = -x_2\mathbf{k}_p$. We work in the proton center of mass frame, which is different from the gluon center of mass frame, and this makes construction of the Lorentz invariant phase space somewhat difficult. Since we are dealing with very high energy processes, we are able to take the gluon momenta to be totally parallel, that is, totally in the direction of motion of the protons. The kinematics of the situation simplify considerably. Let the final state singlet four-momenta be $p_1 = \left(E_{S1}, 0, \cos(\theta)\, p_{1\perp}, \sin(\theta)\, p_{1\parallel}\right)$ and $p_2 = \left(E_{S2}, 0, \cos(\theta)\, p_{2\perp}, \sin(\theta)\, p_{2\parallel}\right)$. From conservation of linear momentum $p_{1\perp} = -p_{2\perp} = p_\perp$.

From conservation of energy, we have

$$(x_1 + x_2)\, k_p - \sqrt{m_S^2 + p_\perp^2 + p_{1\parallel}^2}$$

$$= \sqrt{m_S^2 + p_\perp^2 + p_{1\parallel}^2 + (x_1 - x_2)^2 k_p^2 - 2(x_1 - x_2) k_p p_{1\parallel}}$$

We can use this condition to express E_{S1} and E_{S2} in terms of the transverse and perpendicular momenta. This condition gives us that

$$(x_1+x_2)^2\left(m_S^2+p_\perp^2+p_{1\parallel}^2+(x_1-x_2)^2k_p^2-2(x_1-x_2)k_pp_{1\parallel}\right)$$

$$=\left(\left(x_1^2+x_2^2\right)k_p-(x_1-x_2)p_{1\parallel}\right)^2$$

and

$$(x_1+x_2)^2\left(m_S^2+p_\perp^2\right)^2=4x_1x_2\left(x_1x_2k_p^2-p_{1\parallel}^2\right)+4x_1x_2(x_1-x_2)k_pp_{1\parallel}$$

$$=4x_1x_2\left(x_1k_p-p_{1\parallel}\right)\left(x_2k_p+p_{1\parallel}\right). \tag{A.1}$$

which together give that the energies E_{S1} and E_{S2} can be written as

$$E_{S1}E_{S2}=\frac{\left(2x_1x_2k_p+(x_1-x_2)p_{1\parallel}\right)\left|\left(x_1^2+x_2^2\right)k_p-(x_1-x_2)p_{1\parallel}\right|}{(x_1+x_2)^2}$$

a term which contributes to the wavefunction normalization.

Writing the cross section with gluon momentum distribution functions included in terms of the free gluon cross section gives

$$\sigma_{gg\to SS}=\int_0^1dx_1\int_0^1dx_2f_g(x_1)f_g(x_2)\sigma^{free}_{gg\to SS}.$$

The free cross section is obtained by squaring the matrix element and including the phase space normalization and the symmetry factors. We can also use (A.1) to get the stronger boundary conditions on the phase space integration

$$L_1=\frac{x_1-x_2}{2}k_p-\frac{x_1+x_2}{2}\sqrt{k_p^2-\frac{m_S^2}{x_1x_2}}$$

$$L_2=\frac{x_1-x_2}{2}k_p+\frac{x_1+x_2}{2}\sqrt{k_p^2-\frac{m_S^2}{x_1x_2}}$$

We then have the total cross section, as it appears in Chapter 7:

$$\sigma_{gg\to SS}=\frac{\alpha_s^2\eta^2m_t^4}{3^22^{11}\pi^7k_p^4}\int\limits_{m_S^2/k_p^2}^1dx_1\int\limits_{m_S^2/(k_p^2x_1)}^1dx_2\frac{25}{4}\frac{(1-x_1)^4(1-x_2)^4}{x_1^4x_2^4}\frac{1}{\left(4x_1x_2k_p^2-m_h^2\right)+m_h^2\Gamma_h^2}$$

$$\times I_2^2(x_1,x_2)\int\limits_{L_1}^{L_2}dp_{1\parallel}\frac{(x_1+x_2)\sqrt{4x_1x_2\left(x_1k_p-p_{1\parallel}\right)\left(x_2k_p+p_{1\parallel}\right)-m_S^2(x_1+x_2)^2}}{\left[2x_1x_2k_p+(x_1-x_2)p_{1\parallel}\right]\left|\left(x_1^2+x_2^2\right)k_p-(x_1-x_2)p_{1\parallel}\right|}.$$